PROCESSING, PHASE EQUILIBRIA AND ENVIRONMENTAL DEGRADATION OF
Mo(Si,Al)$_2$ INTERMETALLIC COMPOUND

BY

PAUL D. EASON

A DISSERTATION PRESENTED TO THE GRADUATE SCHOOL
OF THE UNIVERSITY OF FLORIDA
IN PARTIAL FULFILLMENT OF THE REQUIREMENTS FOR THE
DEGREE OF DOCTOR OF PHILOSOPHY

UNIVERSITY OF FLORIDA

1998

Dedicated to Jack.

ACKNOWLEDGEMENTS

The completion of this degree closes a chapter in my life which encompasses the greater portion of my adult years. As an undergradudate freshman I decided that I was not leaving college without the title of "Doctor of Philosophy." What I had not bargained for was remaining at the University of Florida for the duration of that goal. In the years that I have spent here, I have been pleased and surprised to experience many aspects of life outside the realm of my curriculum. My time in Gainesville has afforded me the chance to meet and interact with a group of exceptional people in the forms of friends, colleagues, and mentors. Many of these individuals have combined these roles, and provided me not only a source of guidance, but one of inspiration. Because of the friends I have met during my stay here, I have been exposed to other lands, cultures and ideologies from which I hope to have taken every possible benefit. The support from this circle of friends has allowed me to grow both intellectually and personally, and the education I have received extends far beyond any formal classroom experience.

I would like to thank Prof. Mike Kaufman for being not only an outstanding academic advisor, but for always being an accessible and understanding friend. Mike has allowed me to enjoy graduate school, a gift too often denied to graduate students. I would also like to thank my dissertation committee, with whom I have been fortunate to work. I hope that this document reflects a portion of the combined knowledge of my committee members, whose years of expertise in the field of materials science have been available to me without fail. Most importantly, I must credit the love and support of my family which have brought me to this point in my life, without them none of this would have been possible.

TABLE OF CONTENTS

Abstract of Dissertation Presented to the Graduate School
of the University of Florida in Partial Fulfillment of the
Requirements for the Degree of Doctor of Philosophy

PROCESSING, PHASE EQUILIBRIA AND ENVIRONMENTAL DEGRADATION OF
Mo(Si,Al)$_2$ INTERMETALLIC COMPOUND

By

Paul D. Eason

December, 1998

Chairman: Prof. Michael J. Kaufman
Major Department: Materials Science and Engineering

The Mo(Si,Al)$_2$ C40 compound was chosen for investigation as a possible high

temperature structural material. To produce the C40 phase, several processing routes were

explored with emphasis on obtaining microstructure/property relationships (i.e. control of

grain size and minimization of secondary phases). To facilitate processing of single phase

material, the phase equilibria of the Mo-Si-Al ternary system were reevaluated with respect

to the phases adjacent to the C40 compound. An anomalous environmental degradation

appeared to be the primary obstacle to further study of the compound and was investigated

accordingly.

Several processing routes were assessed for the production of dense, nearly single-

phase Mo(Si,Al)$_2$. Hot powder compaction was chosen as the method of sample

production as is the case with many refractory silicide based materials. Therefore,

variations in the processing techniques came from the choice of precursor materials and

methods of powder production. Mechanical alloying, arc-melting and comminution, and blending of both elemental and compound powders were all employed to produce charges for hot uniaxial pressing. The final compacts were compared on the basis of density, grain size and presence of secondary phases.

Establishment of a Mo-Si-Al ternary isothermal phase diagram at 1400°C was performed. Multiphase alloy compositions were selected to identify the phase boundaries of the C40, C54, T1 and Mo_3Al_8 phase fields, as well as to verify the existence of the C54 phase at 1400°C. The alloys were equilibrated by heat treatment and analyzed for phase identification and quantitative compositional information.

The environmental degradation phenomenon was approached as a classical "pest" with an emphasis of study on grain boundary chemistry and atmospheric dependence of attack. Both Auger spectroscopy and electron microscopy revealed carbon-impurity-induced grain boundary segregation responsible for the embrittlement and material loss. Means of preventing the attack by alloying techniques used in traditional alloys were explored.

CHAPTER 1
INTRODUCTION

The drive to decrease weight, increase operating temperature, and improve the overall performance of turbine engines has been one of the primary forces in material development over the past five decades. The limited service temperature of currently available nickel-base superalloys has led to investigations into new classes of materials which may prove more capable in high-temperature structural applications. Among the materials which have shown promise for elevated temperature application, a class of metallic based compounds called "intermetallics" has garnered much consideration. Intermetallic systems containing aluminum and silicon have been the subject of interest for a number of years due to the unique combination of properties they possess. Among the list of promising attributes, these intermetallics often display high temperature oxidation resistances, relatively high melting points and low density. Conversely, these materials are almost universally plagued by mechanical deficiencies including low ambient fracture toughness and loss of strength at elevated temperature which have been attributed to intrinsic deficiencies including low symmetry crystal structures, covalent-type bonding and complex unit cells. In addition, many intermetallics exhibit temperature regimes of environmental sensitivity, or "pest," leading to grain boundary embrittlement and, in some cases, complete disintegration of polycrystalline parts. Mechanisms of pest vary among the intermetallics yet the term remains pervasive.

Molybdenum disilicide is one of the intermetallic materials being considered for application in high temperature environments. In addition to its high melting point (2020° C) [1] and moderate density (6.24g/cc) [2], this material also displays excellent high temperature oxidation resistance due to the formation of an adherent, glassy silica scale

1

which acts to passivate the surface. However, at lower temperatures (400° - 600° C) the material undergoes pest oxidation which results in the catastrophic degradation of monolithic parts at accelerated rates. Fortunately, a preoxidation step can be performed which will reduce the sensitivity of $MoSi_2$ in this intermediate temperature regime.

Processing of intermetallic compounds is complicated by their high melting points and narrow solubility ranges making powder processing an attractive route for material production. Hot powder compaction is a widely employed technique in the production of $MoSi_2$ and has been successfully used in the processing of this and other silicide-based ternary compounds. Issues commonly associated with powder processing include degree of densificaton and incorporation of oxides resident on powder surfaces. In the case of $MoSi_2$, these factors can directly impact mechanical and environmental properties, making processing schemes critical to the final viability of the material. Inadequate densification of $MoSi_2$ can reduce the resistance to pesting by supplying high diffusivity paths for oxygen penetration. The presence of silica in $MoSi_2$ compacts has been blamed for the loss of strength at elevated temperature as well as its poor creep resistance. To this end, processing investigations have centered on the elimination of silica in powder processed $MoSi_2$ by formation of carbide compounds and reduction of silica to form more stable oxides.

In attempts to improve the utility of $MoSi_2$, both compositing and alloying approaches have been employed in hopes of imparting better mechanical properties. The goal of the latter approach seeks to eliminate the intrinsic deficiencies, such as the low symmetry crystal structure, without compromising the desirable attributes. The aim of alloying $MoSi_2$ is to produce a higher symmetry crystal structure by atomic replacement of either the molybdenum or silicon atoms while maintaining the overall MX_2 stoichiometry. Replacing silicon with additions of aluminum in excess of eight atomic percent yields a ternary compound, $Mo(Si,Al)_2$, with the hexagonal C40 crystal structure directly related to the tetragonal $C11_b$ structure of the binary silicide. It has been suggested that the C40

phase might exhibit improved mechanical properties due to its higher symmetry, as well as enhanced high temperature oxidation resistance due to the formation of an adherent multilayered oxide of silica, mullite, and alumina.

In previous investigations, processing of $Mo(Si,Al)_2$ has been performed by arc-melting, resulting in coarse microstructures often containing minor amounts of secondary phases. In the current investigation, several routes of powder processing were employed to produce dense, nearly single-phase C40. While evaluation of each production method was underway, it was noted that samples produced many months prior and stored in a dessiccator, appeared to display a form of surface degradation. Attempts to accelerate this phenomenon in one week at 200° C resulted in structures similar to those observed in samples maintained at room temperature for 17 months. While attack observed in this anomalously low temperature regime suggested the occurrence of a pest-type phenomenon, there have been no reports of silicides pesting in the vicinity of room temperature.

As is the case with many scientific endeavors, the current investigation evolved to encompass phenomena that were discovered through the course of the experimentation. This study was approached from the onset as a preliminary investigation into the properties of the $Mo(Si,Al)_2$ compound. To this end, the establishment of a reproducible and efficient processing route for dense, nearly single-phase C40 was paramount. As a consequence of processing difficulties, it became necessary to examine the phase equilibria of the Mo-Si-Al ternary system as they pertain to the C40 compound. When the discovery of the anomalous environmental sensitivity of the compound presented a direct obstacle to the future development of this material, it became the focus of the investigation. In turn, this study has been guided by the subsequent observations as they have presented themselves.

CHAPTER 2
LITERATURE REVIEW

2.1 The Mo - Si System

There are three intermediate compounds that form in the Mo-Si binary system. These compounds exhibit limited solubility ranges and covalent type bonding which makes them fall into a class of materials known as intermetallics. These intermetallic phases have been studied for several decades because of their unique properties. Among these properties, the high melting points and relatively low densities have made these molybdenum silicides popular as potential high temperature structural materials.
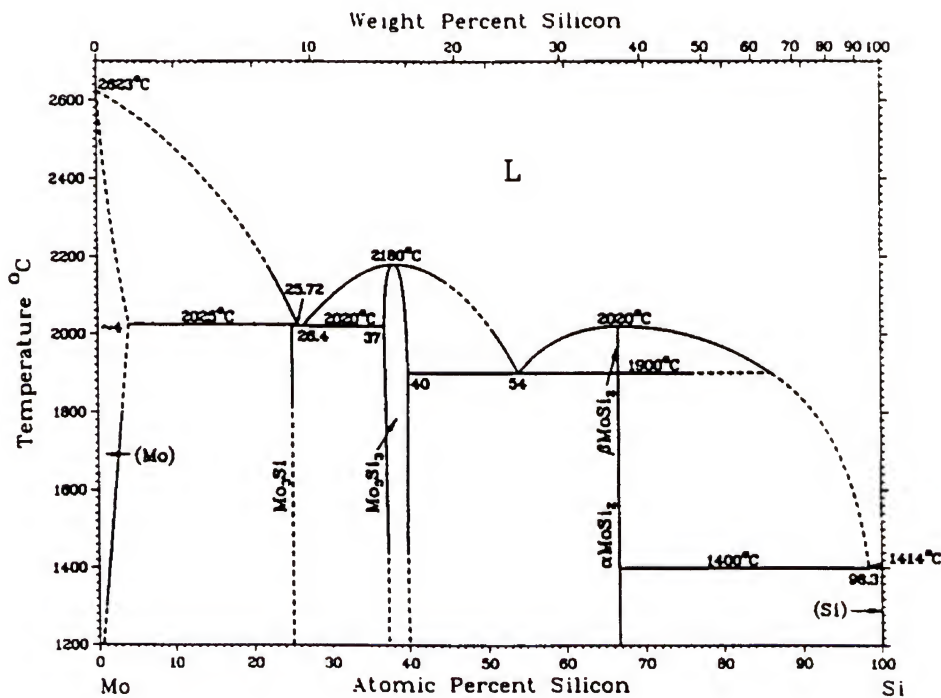

Figure 2.1 The Mo-Si binary phase diagram [1]. NOTE: It has been shown that there is no C40 polymorphic transformation at 1860°C [3].

4

2.1.1 MoSi$_2$ - History and Applications

In the early 1950s, W.A. Maxwell was among the first to consider molybdenum disilicide for use as a high temperature structural material [4]. Simultaneously, in Sweden, the Kanthal Corporation patented a resistance heating element comprised almost entirely of MoSi$_2$ that could be used in air at temperature exceeding 1600°C [5]. These considerations were based on the attractive high melting point (2020° C) and superior oxidation properties characteristic of MoSi$_2$. While Kanthal continued in the development of MoSi$_2$ heating elements, interest in the use of molybdenum disilicide as a structural material was short lived, due to intrinsic deficiencies in properties, namely, low ambient fracture toughness, and loss of strength at elevated temperature [6, 7].

From the late 1950s and early 1960s, considerable attention was given to processing and phase relations in the Mo-Si binary system as well as related ternary systems. Maxwell continued with efforts to surmount the mechanical property deficiencies with some early compositing efforts, attempting to reinforce MoSi$_2$ with alumina. Work by Nowotny and Brukl, among others, led to the development of a series of phase diagrams, and evaluations of many silicide-based systems, including Mo-Si-Al and Mo-Si-C [8-12]. In 1955, Fitzer noted an unusual form of environmental degradation in molybdenum disilicide which he deemed "pest" for its similarity to the "Tin pest" phenomenon [13]. In the early 1970's, Fitzer made notable progress with the reinforcement of molybdenum disilicide by both silicon carbide and alumina.

When advances in technical ceramics brought about the rationale that brittle materials might be engineered for structural applications, there evolved a renewed interest in MoSi$_2$ as a possible structural material. Many of the compositing efforts of the late 1980s and early 1990s focused again on the reinforcement of MoSi$_2$ with phases such as silicon carbide and alumina. These attempts yielded moderate property improvements, but did not provide any distinct advantage over other materials being considered for the same

applications. Efforts still continue in the production of reinforced $MoSi_2$ with an emphasis on *in-situ* processing for the formation of novel composite architectures [14-21]. Despite failure to yet realize structural application, $MoSi_2$ has achieved more commercial success than most intermetallic materials, based on the continued superiority of Kanthal Super heating elements as well as use of $MoSi_2$ for glow plugs in large diesel engines, electronic contacts and interconnects, and as a constituent in TUFI space shuttle tiles [6, 22, 23].

2.1.2 Mechanical Properties of $MoSi_2$

The mechanical properties of molybdenum disilicide were cited from the outset as obstacles to its structural use [4].   For most intermetallics, their covalent nature of bonding combined with their low symmetry crystal structures, and complex unit cells allows a limited number of active slip systems thus excluding the possibility of plastic deformation [6, 7]. $MoSi_2$ exhibits a tetragonal $C11_b$ crystal structure (Figure 2.2) which leads, in part, to its poor mechanical properties. $MoSi_2$ displays low ambient fracture toughness as well as a severe lack of ductility from room temperature to $1000°$ C . At temperatures between $1000°$ C and $1250°$ C, thermal activation of dislocation motion allows a regime of moderate ductility while providing maintained strength. A loss in strength above $1200°$ - $1300°$ C has been attributed to the presence of silica incorporated during powder processing. The softening of silica at these temperatures has been blamed for the grain boundary sliding and mass transport that coincide with a loss in creep resistance and strength [6, 24, 25].

2.1.3 Environmental Properties of $MoSi_2$

One of the most redeeming qualities of $MoSi_2$ comes from the formation of the adherent silica scale which affords superior oxidation resistance at temperatures exceeding $1700°$ C. It is this oxidation resistance that allows the use of molybdenum disilicide as eating elements and glow plugs. Passivation of $MoSi_2$ occurs above $600°$ C when the existing mixed oxide scale is depleted of MoO_3 by means of volatilization (Figure 2.3).
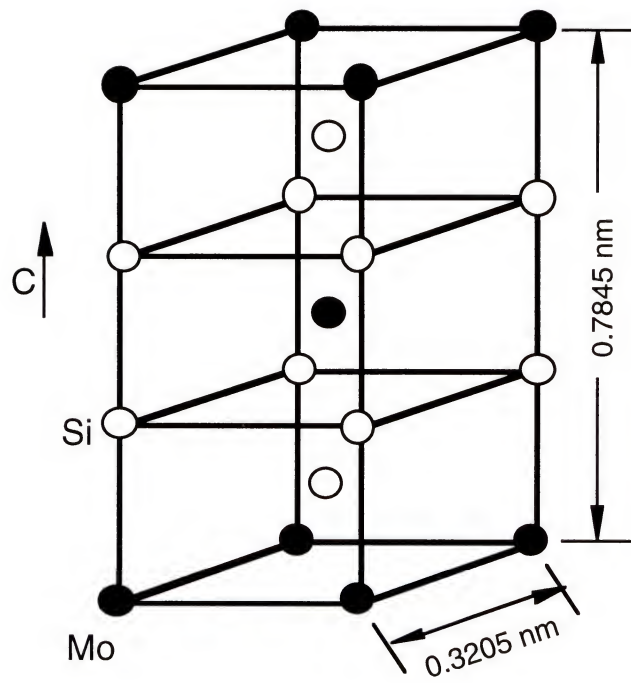
Figure 2.2 Atomic arrangement of the molybdenum disilicide tetragonal C11$_b$ unit cell.
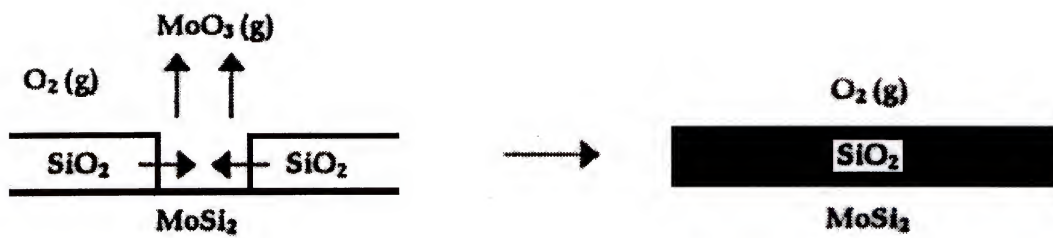
Figure 2.3 Schematic representation of the passivation of MoSi$_2$ by glassy silica formation on the surface above 600°C [26].
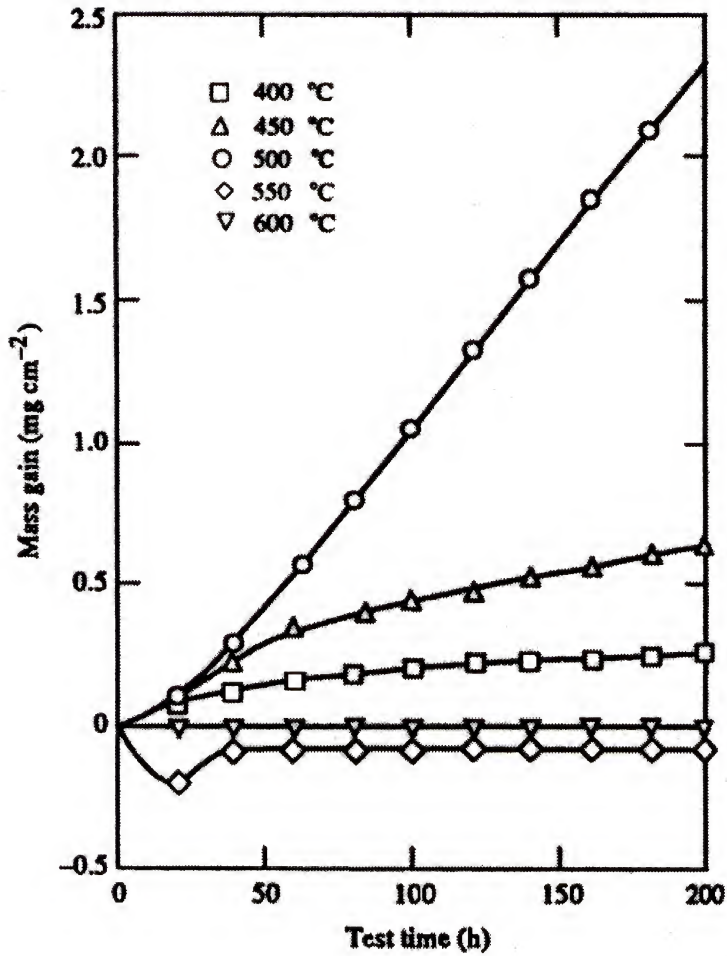
Figure 2.4 Cyclic oxidation behavior of MoSi$_2$ in dry air as a function of temperature [27].

The resulting scale, a glassy silica layer, acts as a diffusion barrier to the further oxidation

of molybdenum [26, 28-31]. The silica scale is amorphous, and can maintain adherence to

the surface without spalling under cyclic temperature conditions (Figure 2.4). By

employing a preoxidation process to form the silica scale, MoSi$_2$ parts can be used without

detrimental oxidation over a range of temperatures and for prolonged heating cycles.

Without the preoxidation step however, there is an intermediate temperature regime where

the environmental sensitivity of MoSi$_2$ is so great that monolithic parts can disintegrate

within a matter of hours. This so-called "pest" of molybdenum disilicide was first noted by

Fitzer, who observed a type of rapid disintegration which occurred in air between 400° and

600° C [13]. The use of the term "pest" is inappropriate since it is based on the "tin pest"

phenomenon which is a result of an allotropic phase transformation, not an environmentally induced failure, yet the term remains pervasive in the literature. Between 400° and 600°C the formation of a mixed oxide scale permits the continued oxidation of molybdenum, to form MoO_2 and MoO_3. At intersections between lattice disruptions (pores, microcracks, and grain boundaries) and free surfaces the volumetric expansion from the formation of molybdenum oxides wedges the boundaries apart, leading to the ultimate disintegration of the part (Figure 2.5). Evaluation of the mechanisms of pest have revealed the rate and occurrence of disintegration are directly related to processing. It appears that the presence of grain boundaries, pores and microcracks all enhance the rate of disintegration by providing high-diffusivity paths for oxygen penetration, but it should be noted that even single crystal monoliths exhibit a form of degradation [26-30, 32-34]. Investigations in alloying to eliminate pest have revealed that a hyperstoichiometry of molybdenum will increase the pest rate while hypostoichiomtery of molybdenum results in the formation of a dark blue passivating layer of silica (Table 2). This "competition" between silicon and molybdenum for stable versus volatile oxide formation has directed
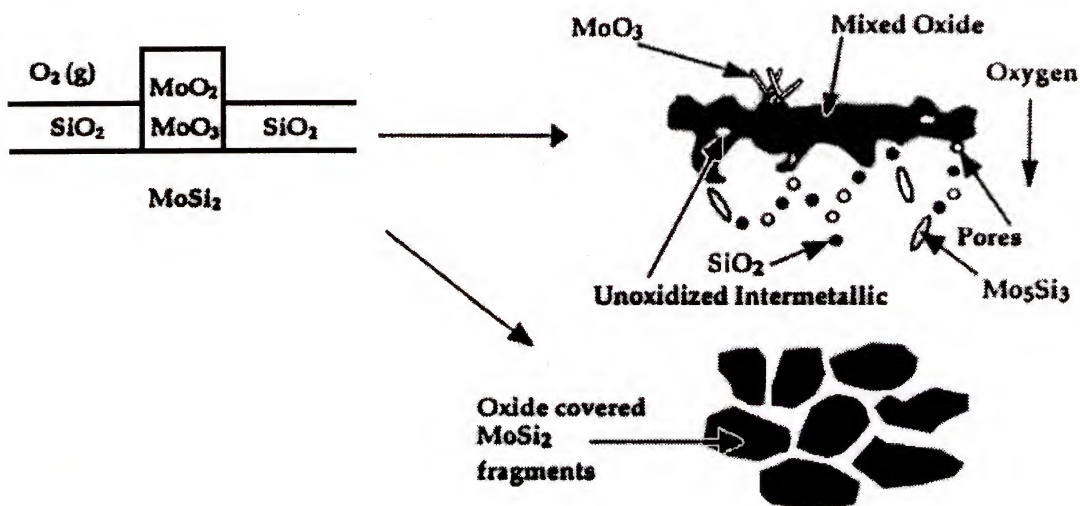

Figure 2.5 Schematic representation of the pesting of $MoSi_2$ between 400° and 600°C by ingress of environmental oxygen [26].

Table 2.1 Effects of stoichiometry and processing on the pest behavior of polycrystalline $MoSi_2$ compacts [28].

Production Method	Composition	Pest Behavior
Arc Melted	67% Si	Disintegrated (24-48 hrs.)
Arc Melted	68% Si (Si-rich)	No Pesting (72 hrs.)
Cold Pressed & Sintered	67.2% Si	Disintegrated (1/2 at 48 hrs.)
Cold Pressed & Sintered	65.4% Si (Mo-rich)	Disintegrated (1/3 at 24 hrs.)
Cold Pressed & Sintered	70.0% Si (Si-rich)	No Pesting (168 hrs.)
Hot Pressed	67.2%	No Disintegration/ Oxide Present (241 hrs.)
Hot Pressed	65.4% Si (Mo-rich)	Disintegrated (one corner at 118 hrs.)
Hot Pressed	70.0% Si (Si-rich)	No Pesting (240 hrs.)

alloying efforts to replace molybdenum with more stable oxide formers (i.e. Cr, W, Ti, Nb) as well as replacing silicon with aluminum in hopes of producing an adherent mullite scale [27, 28, 35-41]; as yet, these efforts have been met with limited success.

2.2 Mo - Si Based Multicomponent Systems

Due to deficiencies in the intrinsic properties of molybdenum silicides, many investigators have proposed that traditional alloying techniques could enhance these properties while maintaining the desirable attributes of the binary compounds [42]. Efforts in the alloying of molybdenum silicides have included both substitutional and interstitial additions. Among the interstitial additions, boron and carbon have been studied the most extensively. While neither carbon nor boron shows appreciable solubility in $MoSi_2$, both form ternary phases based on the 5-3 silicide which have become the focus of much

interest. Substitutional alloying additions have been explored as a means of providing better oxidation resistance as well as improved mechanical properties on the basis of solid solution strengthening and altered crystal structure. As mentioned previously, considerable efforts have concentrated on carbon and aluminum alloying for the elimination of silica in powder processed $MoSi_2$ in combination with the additional advantage of the *in -situ* formation of reinforcing phases to impart toughness and creep resistance [16, 19, 20].

2.2.1 The Mo-Si-B System

The Mo-Si-B system has been studied since the 1950's, and still plays a large role in the development of Mo-Si based materials. The addition of boron to Mo_5Si_3 based materials has been shown to provide an improvement in oxidation behavior, due to the formation of an adherent borosilicate scale [43]. An examination of available binary and ternary phase diagrams of refractory metals indicates that there are few oxidation resistant intermetallic compounds in two-phase equilibrium with refractory metal solid solutions. One of the most notable exceptions is the T_2 phase (Mo_5SiB_2) in the Mo-Si-B ternary system which has been shown to exhibit superior creep resistance and comparable oxidation resistance to $MoSi_2$ without the presence of a moderate temperature "pest" regime [43, 44]. There is strong evidence to suggest that a sufficient volume fraction of dispersed T_2 may provide a molybdenum solid solution matrix with a passivating borosilicate scale in high temperature oxidizing environments [45].

Recent investigations into the equilibria of the Mo-rich portion of the Mo-Si-B phase diagram confirm the existence of a two-phase equilibrium between the solid solution Mo phase and the ternary T_2 phase [46]. Attempts to produce alloys with a two-phase microstructure using traditional arc melting techniques have met with limited success, in that the resulting structures contained coarse matrices of either molybdenum solid solution or T_2 [46-48]. These coarse multiphase microstructures required a minimum of 150 hours
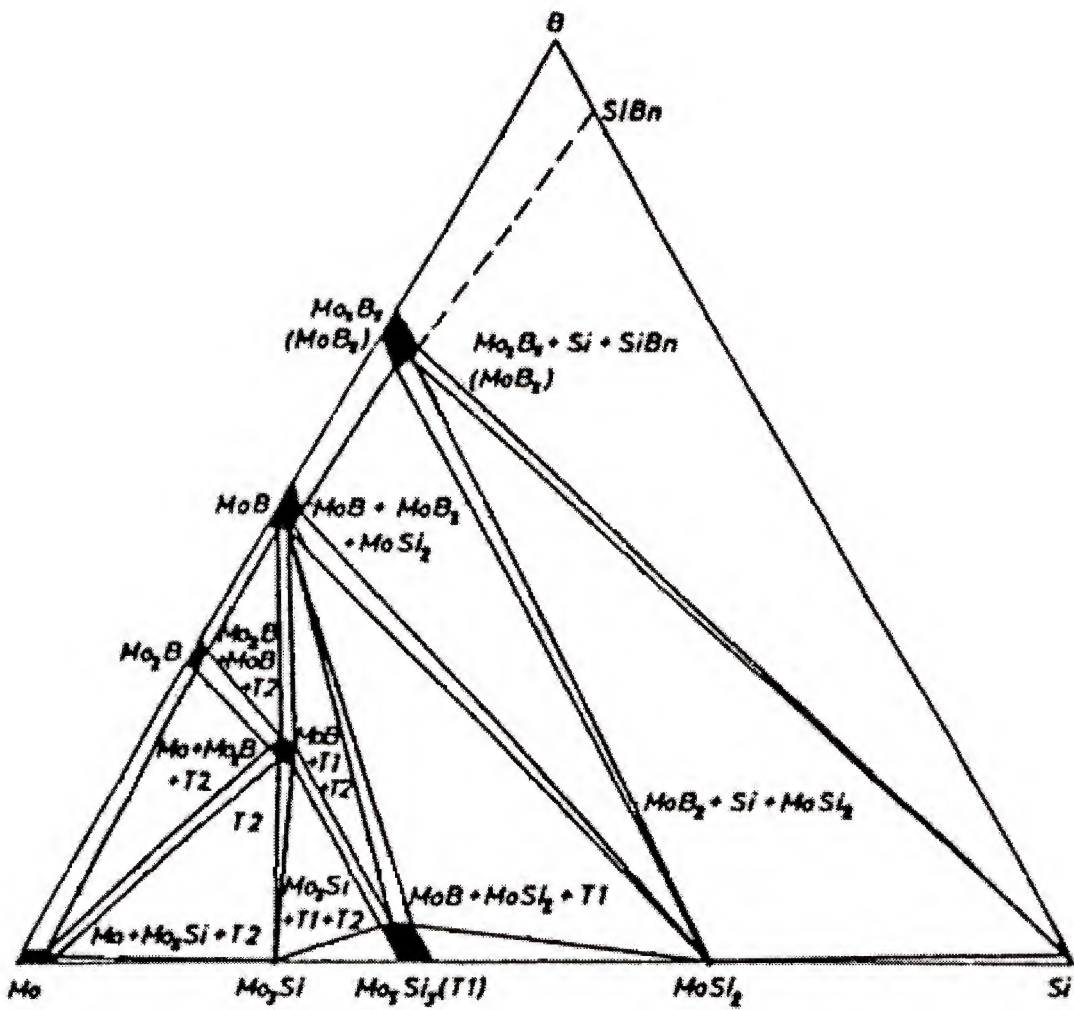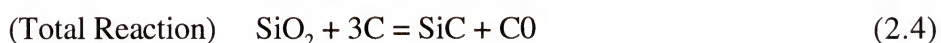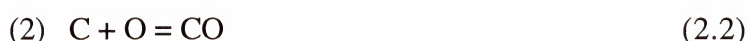
Figure 2.6 Proposed 1600°C isotherm for the Mo-Si-B system [9].

at 1600°C for equilibration to the final two-phase structure. It was concluded that the sluggish dissolution of Mo_5Si_3 or Mo_2B that form during solidification necessitate the lengthy heat treatments. Efforts in rapid solidification of these alloys indicate that splat quenching suppresses Mo_5Si_3 and Mo_2B formation and greatly reduces the time and temperature required for equilibration [46]. It has been suggested that powder processing of Mo_{ss}-T_2 alloys may permit the ability to tailor the solid state reaction sequences by proper choice of precursor materials to prevent the formation of the intermediate Mo_5Si_3 and Mo_2B phases.

2.2.2 The Mo-Si-C System

Due to the necessity of powder processing, elimination of oxides on the surface of powders must be achieved during fabrication of the compact. As stated previously, the addition of carbon has been employed in $MoSi_2$ processing for the purpose of reducing silica to form SiC reinforcements. The addition of carbon has been shown to reduce existing silica by means of the following reaction sequence:

$$(1) \quad SiO_2 = SiO + O \qquad\qquad (2.1)$$

$$(2) \quad C + O = CO \qquad\qquad (2.2)$$

$$(3) \quad \underline{SiO + 2C = SiC + CO} \qquad\qquad (2.3)$$

$$\text{(Total Reaction)} \quad SiO_2 + 3C = SiC + C0 \qquad\qquad (2.4)$$

resulting in a final structure of $MoSi_2$, SiC, and Nowotny phase (Figure 2.7) [49, 50]. The distribution of these phases as well as their morphologies are subject to the processing conditions of the material. Continued interest in SiC-reinforced $MoSi_2$ led to current studies of the Nowotny phase, which is often present due to the narrow two-phase equilibrium between $MoSi_2$ and SiC [19, 21, 51]. Silicon-carbide-reinforced molybdenum disilicide has shown both improved creep resistance and yield strength, as well as superplastic behavior [16, 21, 52].
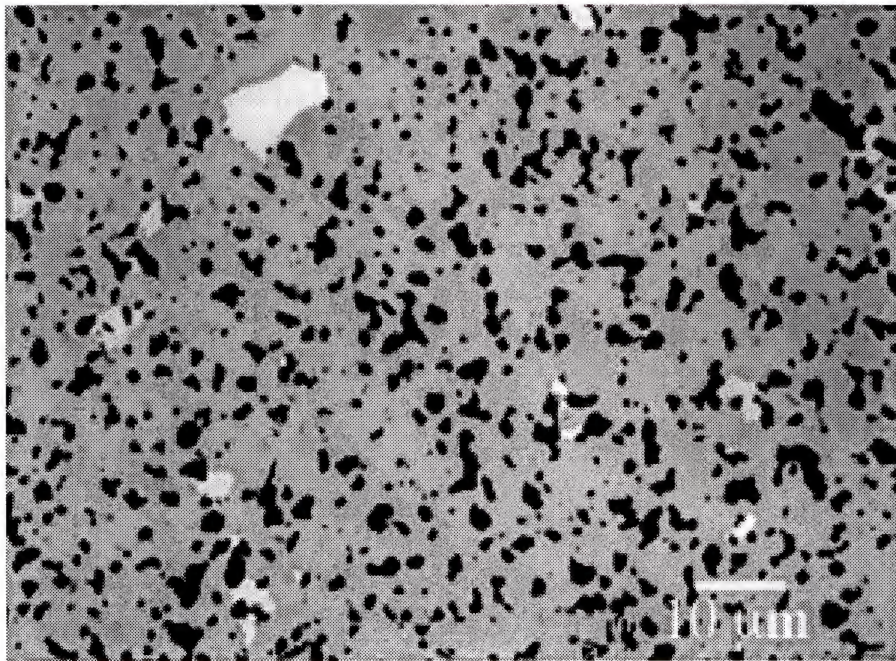
Figure 2.7 Backscattered electron image of SiC reinforced MoSi$_2$. The dark, medium, and light phases are SiC, MoSi$_2$, and Nowotny phase respectively [16].
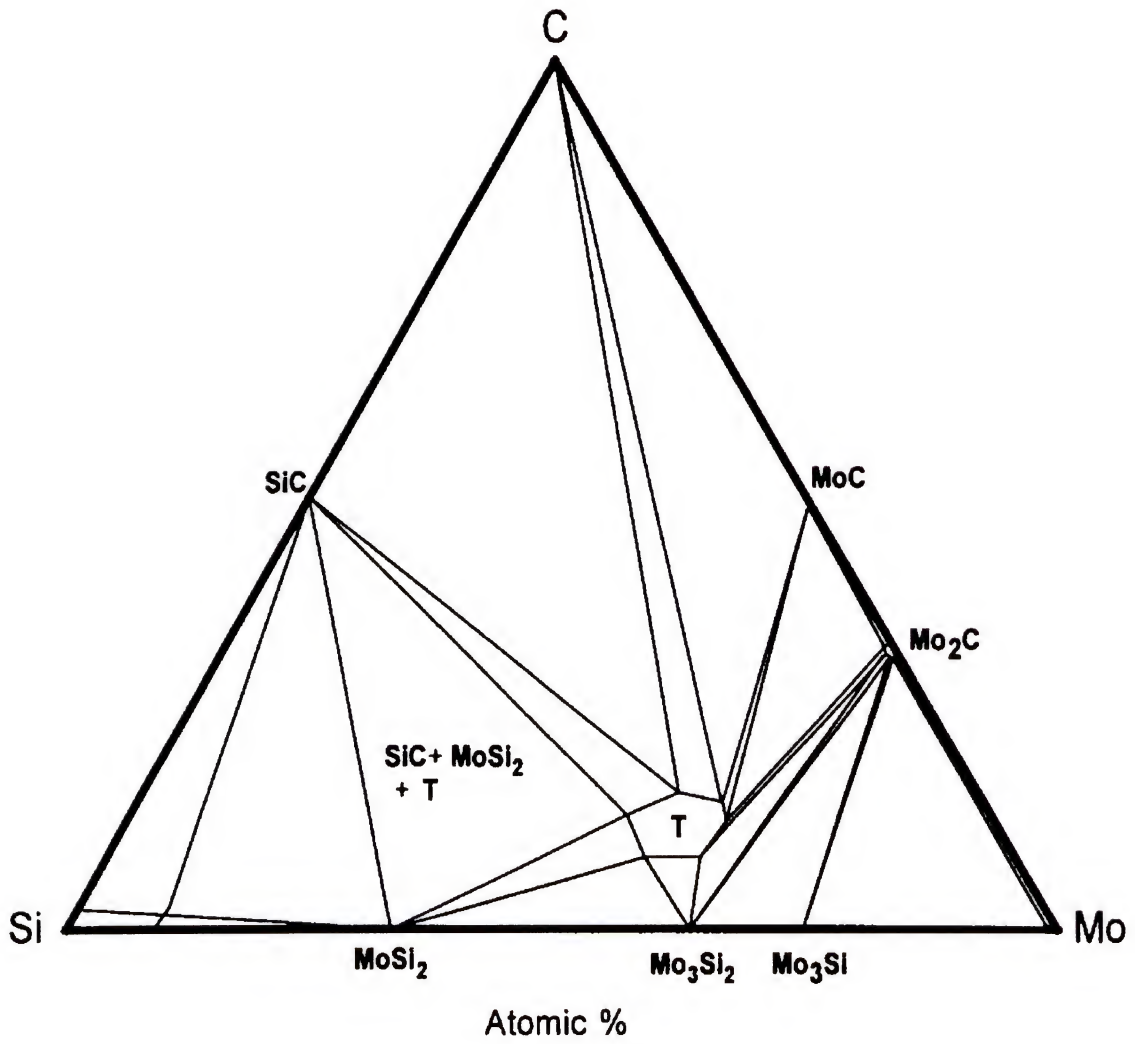
Figure 2.8 Proposed 1600°C isotherm for the Mo-Si-C [10].

2.2.3 The Mo-Si-Al System

The Mo-Si-Al system displays two ternary compounds as well as extensive ternary solubility in most of the binary compounds (Table 2.2). Atomic substitution for silicon accounts for the large aluminum solubility in the 5-3 silicide as well as the complete solubility of the 3-1 compound. Aluminum is the only thoroughly studied material with ternary solubility in molybdenum silicides by means of silicon replacement. Since silicon is the primary source of the passivation of molybdenum silicides (through silica formation), many studies have focused on the effect of its replacement by aluminum on oxidation properties [36, 40, 41, 53].

Aluminum alloying efforts have been pursued as a means of imparting a more "metallic character" to $MoSi_2$ by producing the ternary C40 phase which has a higher symmetry structure [42]. The replacement of silicon with aluminum in excess of 8 At.% results in a ternary compound with the hexagonal C40 crystal structure which is related to the tetragonal $C11_b$ structure of the binary silicide [12]. Aluminum additions have been shown to reduce existing silica via *in-situ* reactions as well [20, 21, 52]. The following reaction and conditions were set forth by Costa e Silva as the governing restrictions for the use of aluminum in silica reduction:

$$4Al + 3SiO_2 = 2Al_2O_3 + 3Si \tag{2.5}$$

$$Al_T \geq 2/3O_T + Al_R \tag{2.6}$$

$$(Si + Al_R)/Mo = 2 \tag{2.7}$$

$$Al_R \leq Al_S \tag{2.8}$$

Where Al_T is the total aluminum added to the alloy, Al_S is the solubility limit of aluminum in molybdenum disilicide, and Al_R is residual aluminum in solution after complete reduction of the silicon dioxide. The resulting $MoSi_2$ - Al_2O_3 structures are shown to be

Table 2.2 Summary of the binary and ternary phases of the Mo-Si-Al system.

| System	Compound	Structure	Remarks	Source
Mo-Si	Mo_3Si	$Pm\bar{3}n$	Complete ternary solubility with Mo_3Al	[1]
	Mo_5Si_3	I4/mcm	Some ternary solubility	[1]
	α - $MoSi_2$	I4/mmm		[1]
	β - $MoSi_2$	$P6_222$	Does not exist as binary	[3]
Si-Al			No binary phases exist	
Mo-Al	Mo_3Al	$Pm\bar{3}n$	Complete ternary solubility with Mo_3Si	[54]
	MoAl	No reference	1470° - 1720°C	[54]
	$Mo_{37}Al_{63}$	No reference	1490° - 1570°C	[54]
	Mo_3Al_8	C2/m		[54]
	$MoAl_4$	Cm		[54]
	$MoAl_5$	$P6_3$		[54]
	$MoAl_{12}$	cI26		[54]
Mo-Si-Al	$Mo(Si,Al)_2$ (C40)	$P6_222$	8-35 At.% aluminum	[11]
	$Mo(Si,Al)_2$ (C54)	Fddd	45 At.% aluminum	[11]
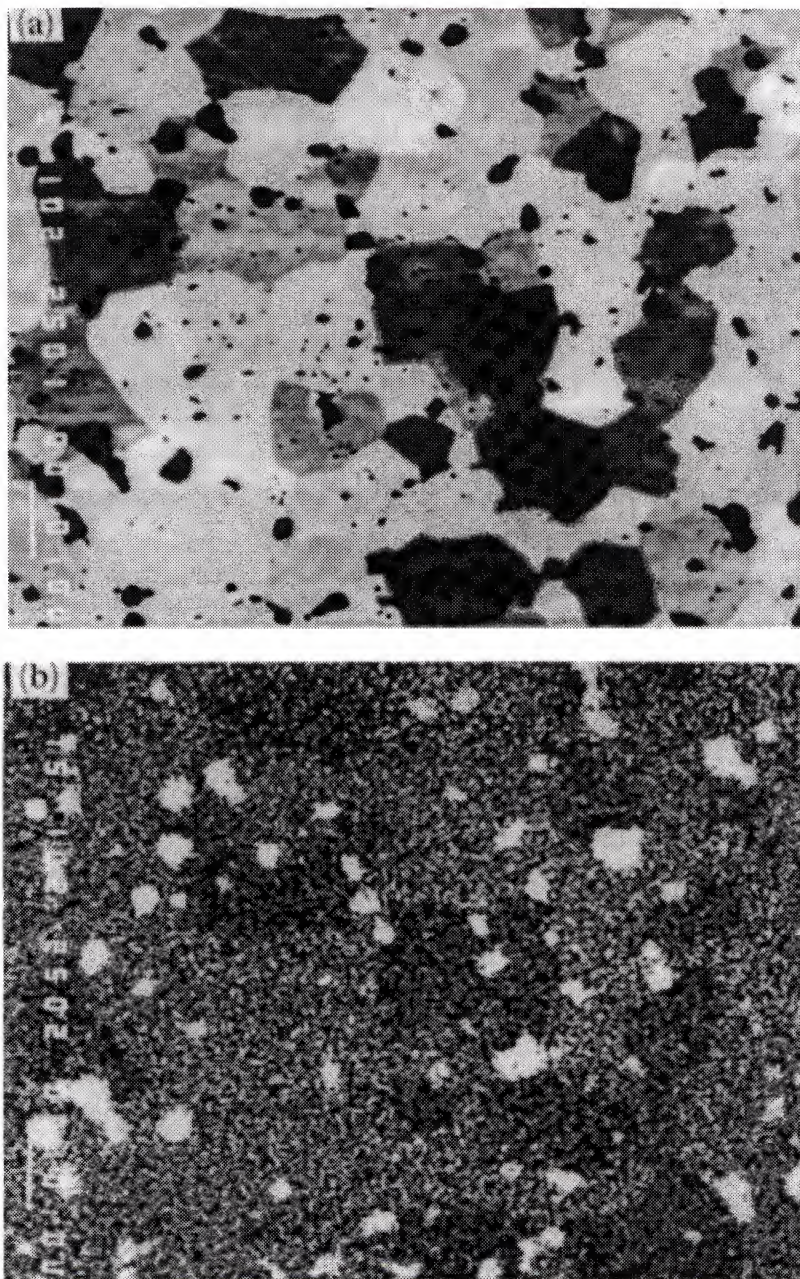
Figure 2.9 Electron micrographs of an Al_2O_3-$MoSi_2$-$Mo(Si,Al)_2$ composite. (a)
Backscattered electron image of alumina reinforced $MoSi_2$ (b) Al K_α x-ray map of
same region [21].

thermodynamically stable (Figure 2.9), yet there has been limited subsequent work concerning the properties of these alumina-reinforced composites [7, 14, 15, 21, 55].

The ternary isotherms proposed for the Mo-Si-Al system by Brukl (Figure 2.11) and Yanigahara (Figure 2.12) display discrepancies with each other and are inconsistent with recent experimental results. Errors in the Brukl diagram include the Mo-Al "side" of the isotherm which is not in accordance with the currently-accepted Mo-Al binary phase diagram (Figure 2.10), as well as the absence of any liquid phase at 1600°C. It should also be noted that the Brukl isotherm is not truly an isothermal section of the diagram, but instead slopes down from 1600°C on the Mo-Si side to 1350°C on the Al-rich portion of the diagram. The Yanigahara isotherm (at 1550°C) includes the liquid phase which is ignored by Brukl, but excludes the presence of the C54 phase. The Yanigahara diagram also neglects the presence of the $Mo_{37}Al_{63}$ phase which is present at 1550°C. Both diagrams agree on the relative placement of the C40, $C11_b$, and T1 phases but differ with respect to their ranges of solubility.
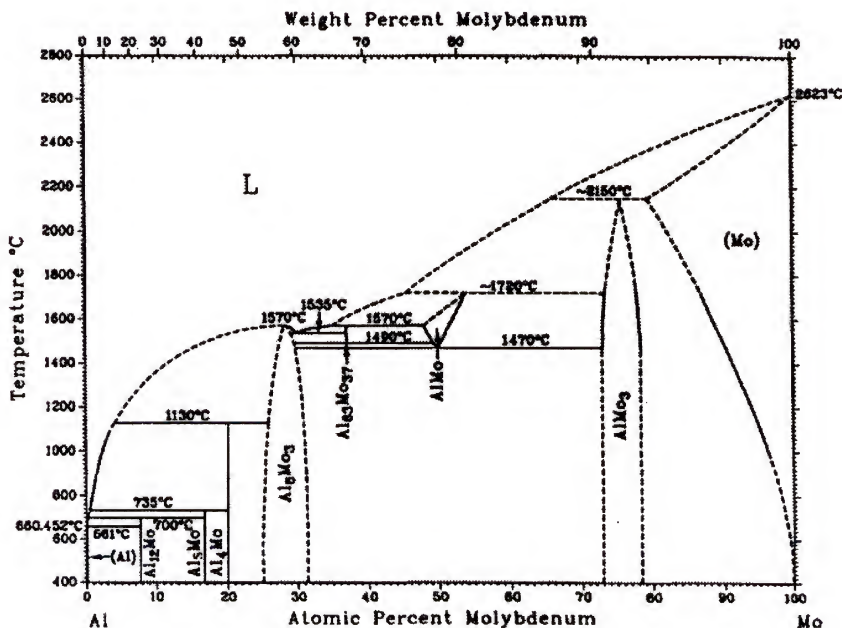

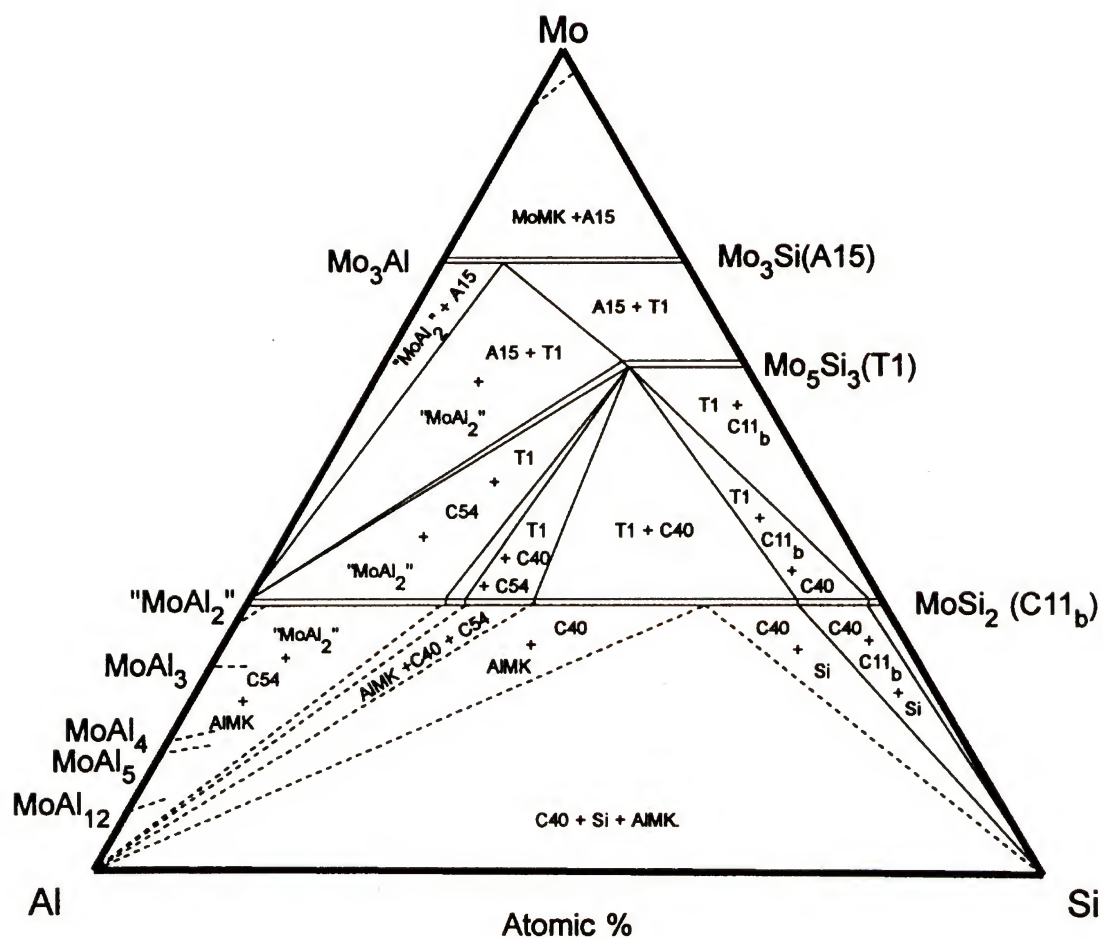Figure 2.10 The Mo-Al binary phase diagram [54].

Figure 2.11 Ternary phase diagram isotherm at 1600°C of the Mo-Si-Al system proposed by Brukl and coworkers in 1961 [11].
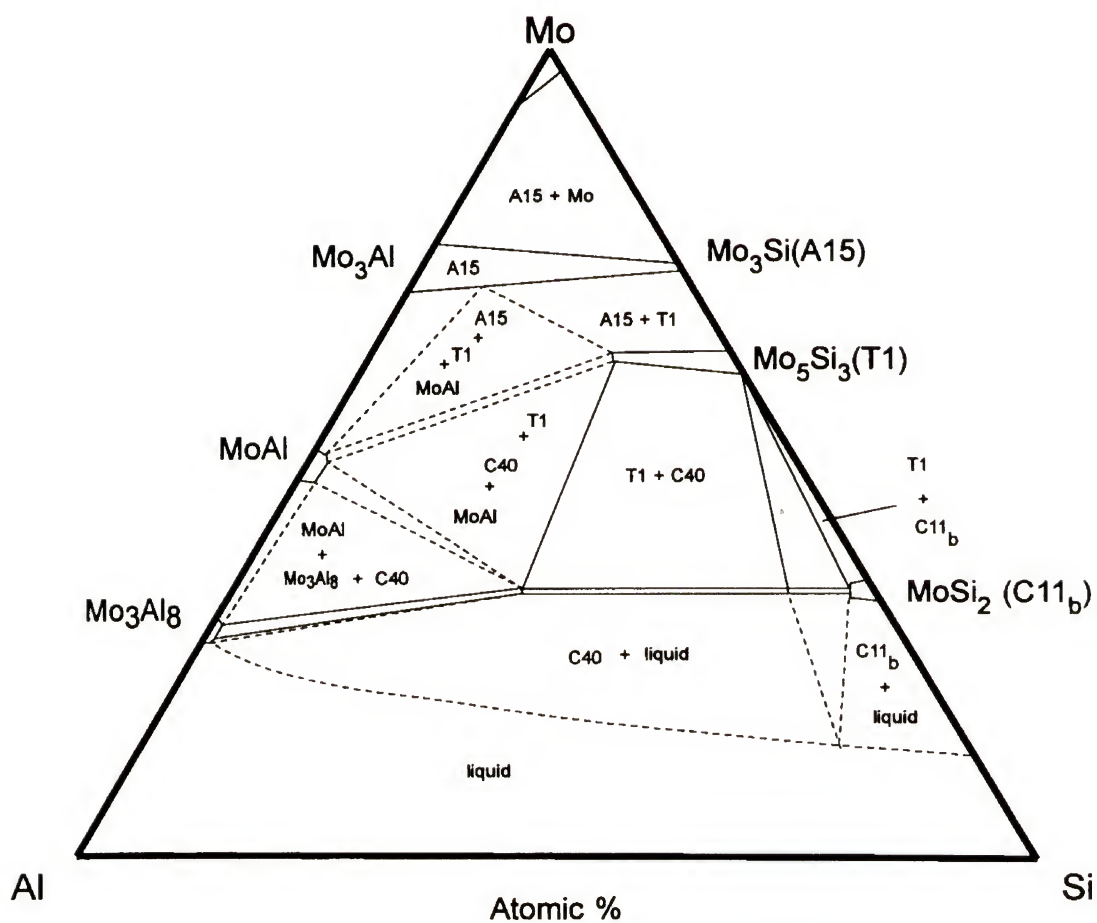
Figure 2.12 Ternary phase diagram isotherm at 1550°C of the Mo-Si-Al system proposed by Yanigahara and coworkers in 1993 [40].

2.2.4 Mo-Si-X Systems

Substitutional alloying of molybdenum silicides can be performed by occupying either the molybdenum or silicon atomic site with an appropriate species. As mentioned earlier, there are few known elements that will replace silicon in this manner, and therefore, much of the substitutional alloying in molybdenum silicides has been performed by the replacement of molybdenum with other refractory metals (Table 2.3). The elements shown in the table are considered to be the best possible "replacements" for Mo in $MoSi_2$ due to their atomic radii, electronegativity and structure [56]. Boettinger has reviewed a series of alloying studies which focused on the replacement of molybdenum with elements that form similar silicide structures (Ti, Cr, Ta, W, Nb) [3]. The result is a listing of ternary isotherms and quasibinary phase diagrams of the disilicide and 5 - 3 silicide compounds (Figure 2.13). In Boettinger's study it was also concluded that there is no high temperature C40 polymorph in binary $MoSi_2$ [3]. Assessment of the $MoSi_2$ - $TiSi_2$ quasibinary revealed that the C40 phase, which was suspected to form from an allotropic transformation above 1860°C in $MoSi_2$ was actually formed by a peritectic reaction between liquid and a solid solution with the formula $(Mo,Ti)Si_2$. It was concluded that the observed C40 $MoSi_2$ phase was the result of impurities in the "binary" material.

An inspection of the disilicide quasibinaries reveals that two crystal structures, $C11_b$ and C40, are known to form as solid solutions of most $(Mo,X)Si_2$ alloys. The hexagonal C40 phase is present in nearly all of these ternary systems, often with large (>10 at.%) solubility ranges. This phase, which possesses a higher symmetry structure than the tetragonal $C11_b$ of the binary disilicide has inspired alloying to be considered as the best approach to impart more active slip systems to $MoSi_2$ (Figure 2.14) [3, 11, 12, 35, 42, 57].
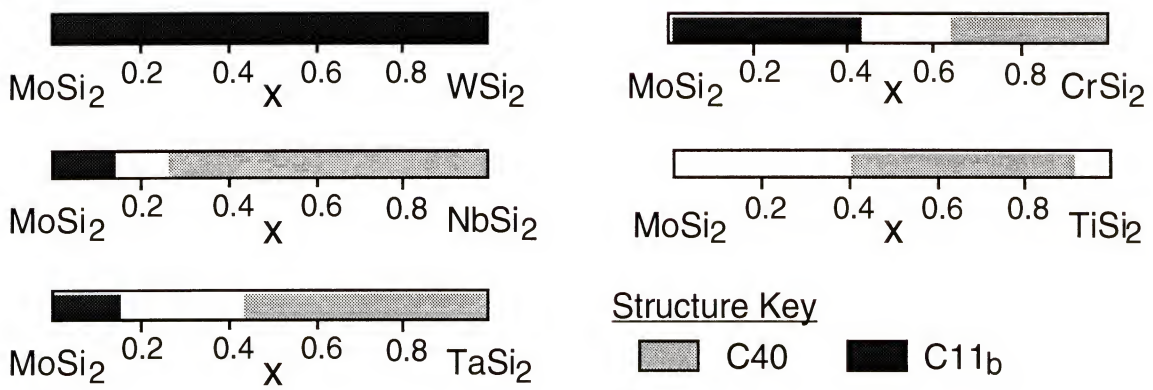
Figure 2.13 Homogeneity ranges of $C11_b$ and C40 in molybdenum disilicide based quasibinary systems at $1600°$ C (except $NbSi_2$ based system which is at $800°$ C) [3].

Table 2.3 Characteristics of suitable alloying elements for atomic substitution of Mo in $MoSi_2$.

| Element (X)	Electron Configuration	Atomic Radius (Å)	Electroneg-ativity	r_X / r_{Mo} (Atomic)	Crystal Structure
Cr	$3d^54s$	1.27	1.66	0.91337	bcc, hcp
Co	$3d^74s^2$	1.25	1.88	0.8993	hcp, fcc
Fe	$3d^64s^2$	1.26	1.83	0.9065	bcc, fcc
Hf	$5d^26s^2$	1.59	1.30	1.1438	hcp
Ni	$3d^84s^2$	1.24	1.91	0.8921	fcc
Nb	$4d^45s$	1.46	1.60	1.0504	bcc
Ta	$5d^26s^2$	1.46	1.50	1.0504	bcc
Ti	$3d^24s^2$	1.47	1.54	1.0576	hcp, bcc
V	$3d^34s^2$	1.34	1.63	0.9640	bcc
Te	$4d^55s^2$	1.36	1.90	0.9784	hcp
Re	$5d^56s^2$	1.37	1.90	0.9856	hcp
Ru	$5d^56s^2$	1.34	2.20	0.9640	hcp
W	$5d^16s^2$	1.39	2.36	1.0000	bcc
Zr	$4d^55s^2$	1.60	1.33	1.1511	bcc
Mo	$4d^55s$	1.39	2.16	1.0000	bcc
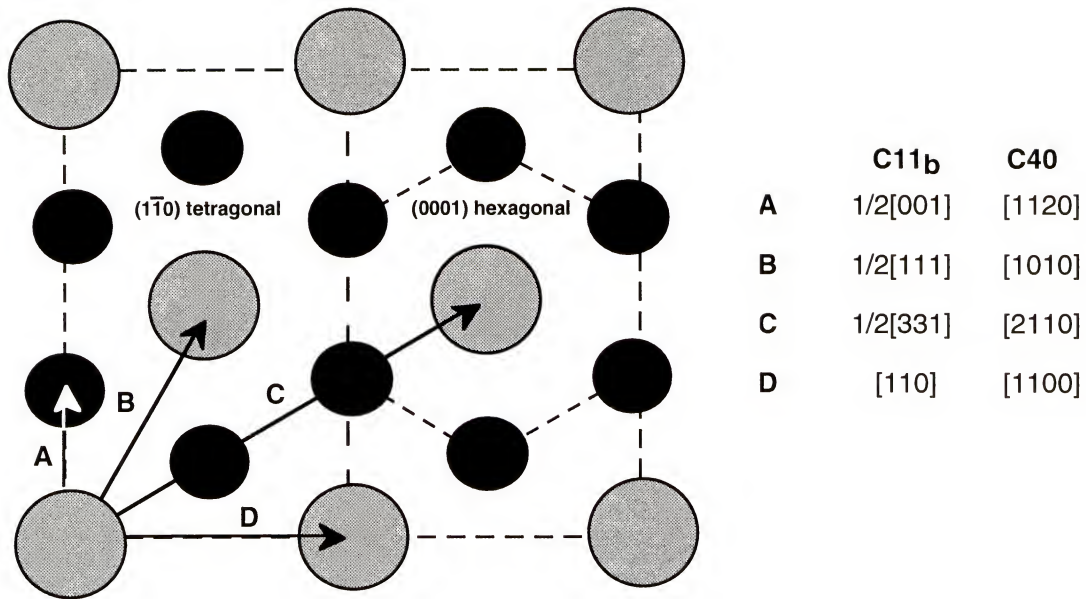
Figure 2.14 Atomic arrangement and orientation relationship of the $C11_b$ and C40 phases. Gray cricles indicated placement of refractory metals atoms (Mo,W,Ta, etc.) atoms. Black circles indicate placement of Al or Si atoms.

2.3 The Mo(Si,Al)$_2$ C40 phase

The C40 phase can also be produced from MoSi$_2$ by the replacement of silicon with aluminum in excess of eight atom percent to form Mo(Si,Al)$_2$. Despite 40 years of investigation there is little consensus concerning the properties of this phase. The proposed Mo-Si-Al isotherms agree on the placement of the C40 phase, but differ greatly with respect to the presence and composition of adjacent phases. Reports of enhanced mechanical properties and cyclic oxidation have been countered with the findings of increased high temperature oxidation rate, and the existence of an anomalous room temperature pest phenomenon [8, 11, 20, 21, 35, 38-41, 51, 53, 58, 59]. As mentioned in Chapter 1, this investigation has yielded some of what is currently known about the Mo(Si,Al)$_2$ compound, tying this section of the text closely to results from this investigation. Therefore, some experimental results will be briefly discussed as needed to explain currently studied phenomena.

2.3.1 Mechanical Properties of Mo(Si,Al)$_2$ C40

The mechanical behavior of the Mo(Si,Al)$_2$ C40 phase remains largely unexplored. Some work with single crystal material indicates fewer active slip systems than in the binary silicide, discounting earlier beliefs that the increased symmetry of the C40 crystal structure would bring about increased ductility (Figure 2.15) [58]. Efforts in assessing the mechanical properties of polycrystalline materials have focused mainly on two-phase mixtures of C40 and C11$_b$ in which the room temperature microhardness of C40 shows a 25% increase over that of MoSi$_2$ [35]. In the same investigation the hot hardness of the C40 phase shows comparable decrease compared to the values of MoSi$_2$. The processing methods used in the investigation were somewhat suspect, and these results are not necessarily considered applicable to single-phase C40. To date there is little information on the mechanical behavior of polycrystalline, single-phase C40. Preliminary experiments in this study revealed extensive grain boundary decohesion in a shear band that formed during hot compression testing at 1400°C (figure 2.16). Attempts to assess the room temperature microhardness were also plagued by grain boundary decohesion (Figure 2.17). This decohesion extended several grains into the matrix, making the data measured from the indent invalid for microhardness evaluation. These observed grain-boundary phenomena were assumed to be associated with the environmental susceptibility of the boundaries. Thus, further mechanical property investigations were postponed pending a better understanding of this behavior.
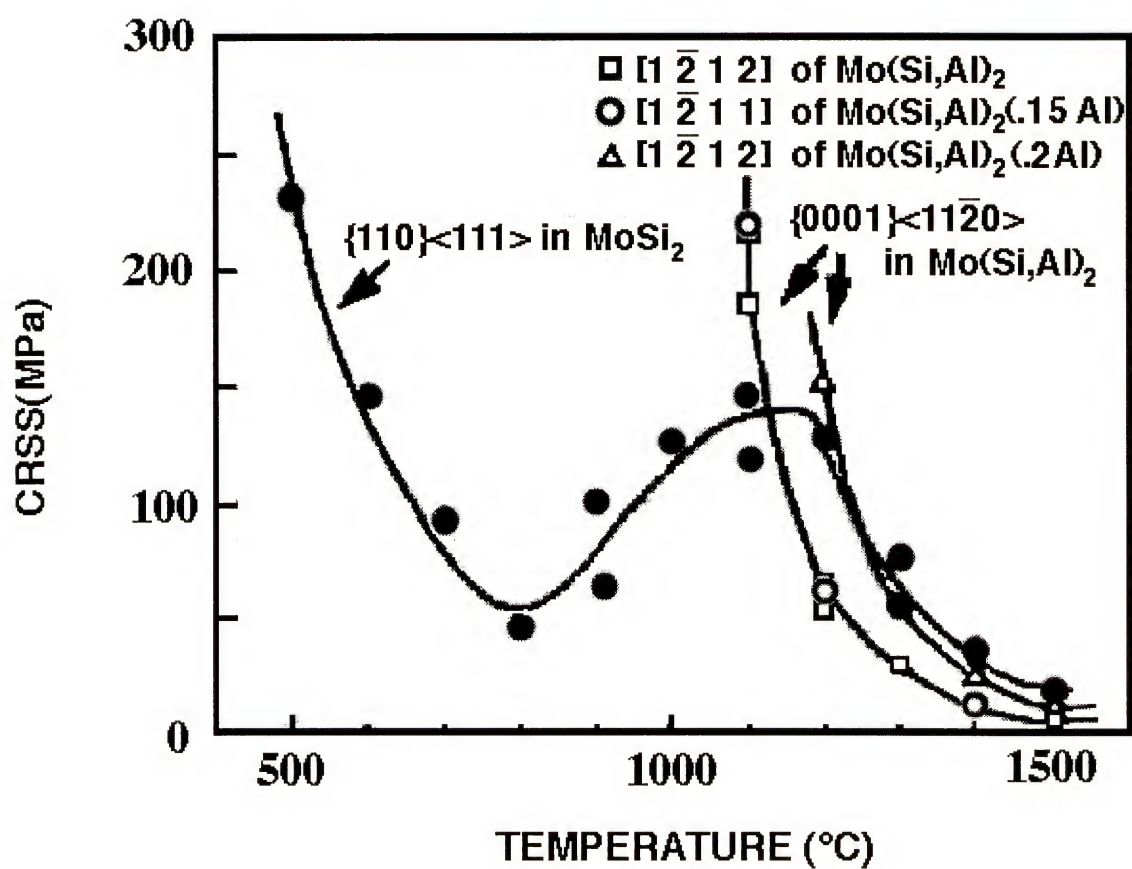
Figure 2.15 Temperature dependence of CRSS for basal slip in Mo(Si,Al)$_2$ single crystals. The CRSS-temperature curve for {110}<111> slip in MoSi$_2$ is also illustrated [58].
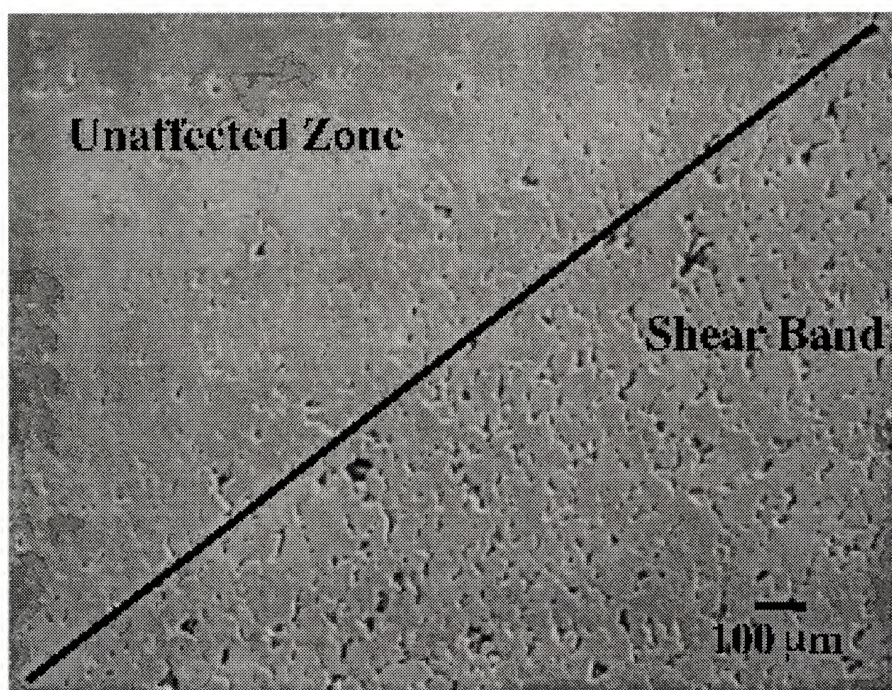
Figure 2.16 Secondary electron micrograph of a shear band formed during compression testing at 1400°C with a strain rate of 10^{-4}. Diagonal black line is drawn to denote the approximate boundary of the shear band.
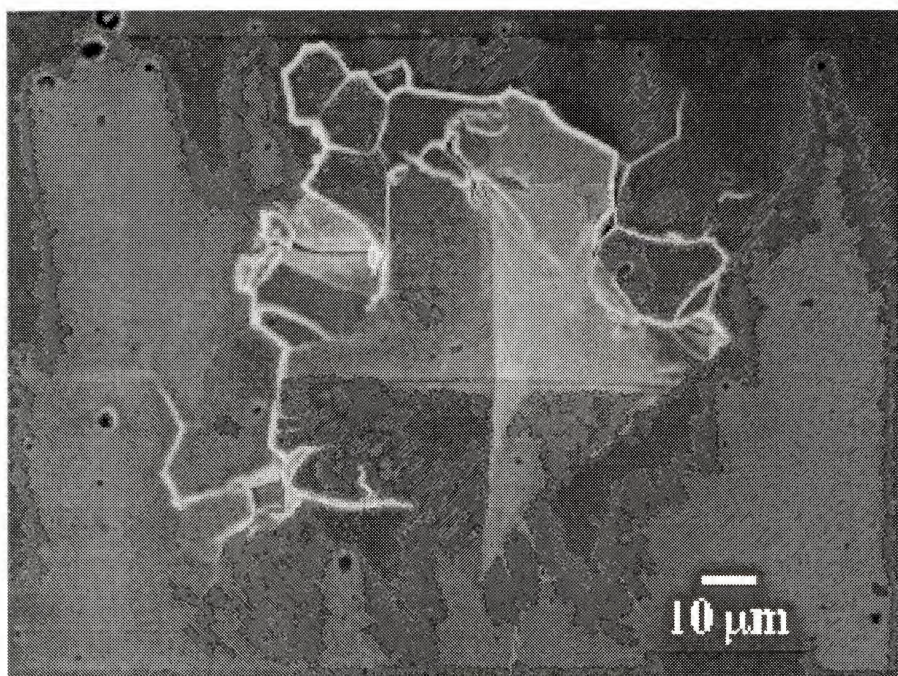
Figure 2.17 Secondary electron image of a Vickers microhardness indent in the C40
Mo(Si,Al)$_2$. Note the grain boundary decohesion.

2.3.2 Environmental Properties of C40-Mo(Si,Al)$_2$

Most studies of the environmental properties of the C40 phase have focused on the high temperature oxidation behavior of Mo(Si,Al)$_2$ in both static and cyclic temperature conditions. These studies almost universally conclude that the high temperature passivation of C40 is achieved by the formation of an adherent, multilayered scale consisting of Al$_2$O$_3$, mullite and SiO$_2$. Differences in these reports concern the rate of oxidation which has been reported to be both slightly higher and lower than that of MoSi$_2$ [35, 38-41]. These differences may be attributable to both the sample compositions as well as the resulting sample microstructures, although a thorough examination of these factors has not been performed. The most extensive study of the high temperature oxidation of Mo(Si,Al)$_2$ was performed by Yanigahara and coworkers, whose investigations provided insight into the nature of the layered oxide scale that forms on the surface of C40 [40, 41]. This scale, comprised of Al$_2$O$_3$ and SiO$_2$ resists spalling under conditions of cyclic oxidation, but is subject to liquification due to the eutectic type reaction between the two oxides. During liquification, oxygen transport to the base materials is enhanced and the scale does not passivate as effectively as the SiO$_2$ scale on binary MoSi$_2$ (Figure 2.18).

As mentioned earlier, during the course of this study an anomalous room temperature degradation of C40 was observed. This degradation phenomenon occurs in air at room temperature over a period of months and is marked by decreased grain boundary strength and an apparent loss of material to a vapor product (Figure 2.19). The resulting samples display increased porosity along grain boundaries most often at triple points (Figure 2.20). Attempts to accelerate this phenomenon by heating in air at 200°C have resulted in similar structures to those observed in samples that have been maintained at room temperature for 17 months.
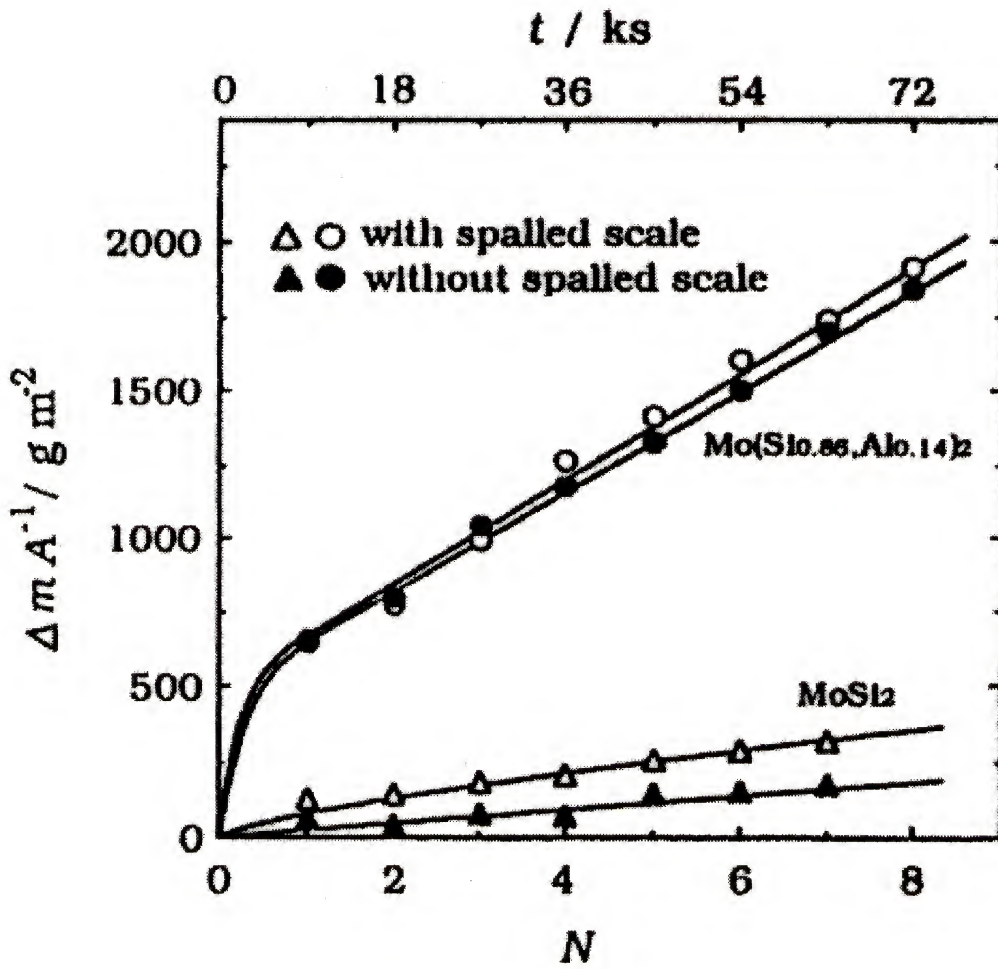
Figure 2.18 Cyclic oxidation behavior of Mo(Si,Al)$_2$ and MoSi$_2$ at 2023 K. Note the increased oxidation rate of the Mo(Si,Al)$_2$ alloy, despite the resistance to scale spalling [40].
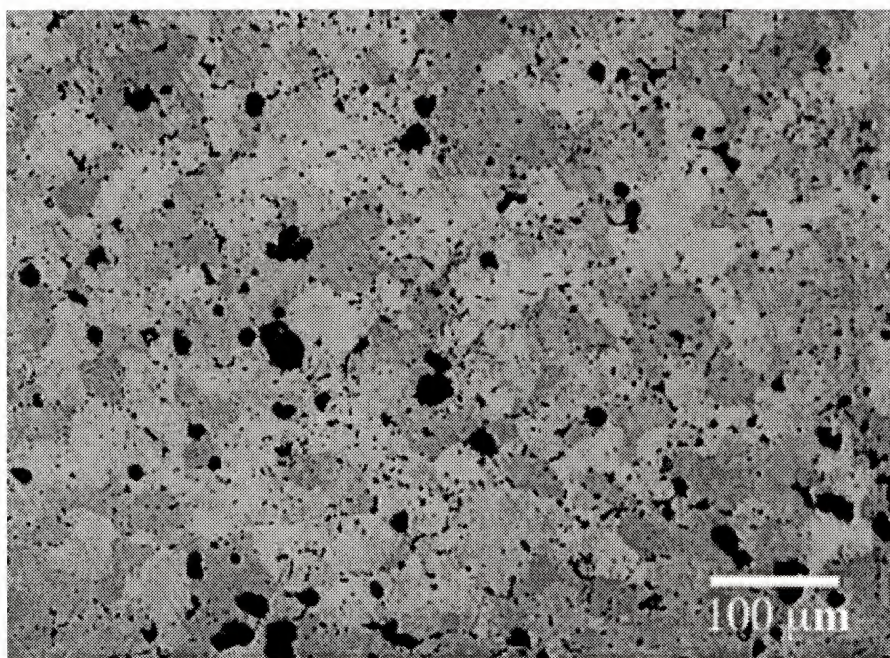
Figure 2.19 Secondary electron micrograph of a Mo(Si,Al)$_2$ C40 exposed to air at room temperature for 17 months. Gray regions are C40 matrix. Black regions are pores, remnant from environmental attack.
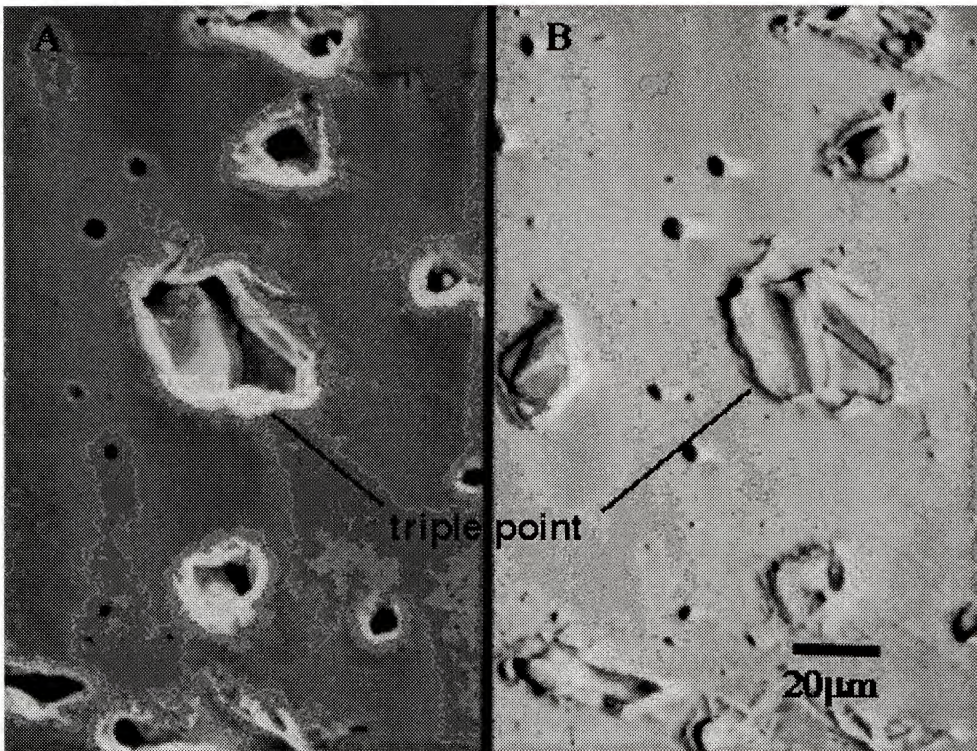
Figure 2.20 Split-screen electron micrograph of attacked grain boundary triple-point after sample exposure to air at 200°C for 160 hours. A) Secondary electron image; B) Backscattered electron image.

2.4 Environmental Properties of Intermetallics

2.4.1 Pesting of Intermetallics

The term "pest" (as it pertains to intermetallics) was first applied to the behavior exhibited by molybdenum dislicide in the temperature range between 400 and 600°C [13]. Since then, the term has become associated with the unusual environmental behavior of many intermetallic compounds. This behavior can include disintegration, embrittlement and material loss as a result of environmental factors. Because molybdenum disilicide is not the only intermetallic material to exhibit pest behavior, much attention has been paid to the nature of the anomalous environmental sensitivities of this class of materials. In their seminal paper, Westbrook and Wood [60] established a criterion for pest disintegration, which provides the standard for phenomenological identification of pest in intermetallics. The criteria are as follows:

1. The attack is predominantly intergranular (although a considerably moderated form of disintegration has been observed in single crystals).

2. Attack does not occur in inert atmospheres.

3. Disintegration will occur under either isothermal conditions or thermal cycling conditions as long as there is some exposure in the critical range.

4. Disintegration occurs at a time and place where the volume fraction of oxide formed is negligible.

5. The temperature range for the effect is specific to a given compound.

6. The period of rapid oxidation during which the powdering reaction occurs is preceded by an incubation period.

7. The effect can be aggravated by the presence of moisture
   in the atmosphere.

8. The effect can be aggravated by the presence of minor
   impurities in the compound.

9. The effect can be moderated by high temperature
   preoxidation or by appropriate alloying.

These nine features are among the most commonly observed pest phenomena, but they do not represent an exhaustive or universal description for pest in all intermetallic materials. In recent years, investigation of environmental sensitivity of intermetallic compounds has led to the distinction between different pesting mechanisms including internal surface oxidation and grain boundary embrittlement.

One proposed mechanism of pesting concerns the rapid oxidation of internal surfaces which leads to phase-change-induced volumetric expansions, forcing boundaries and cracks to separate. The phenomenon is dependent on the ingress of oxygen along the various high diffusivity paths (grain and interphase boundaries, cracks and pores). It has been shown that, in molybdenum disilicide, the formation of voluminous oxides along grain boundaries is responsible for the disintegration of polycrystalline parts [28-30, 33, 61-63]. The pest effect in $MoSi_2$ can be reduced by making parts of greater than 95% density where it is suspected that the reduction in open porosity acts to reduce the oxygen ingress into the material [63]. The disintegration of polycrystalline parts is dependent on the mechanism of grain boundary tenslie stresses from the creation of the oxide phases, but is also dependent on the brittle nature of the intermetallic itself. These materials usually exhibit negligible plastic deformation at room temperature, making internal stresses much more detrimental to the part. Without the ability to yield plastically, the formation of voluminous oxides literally forces the grains away from each other. Internal oxidation can occur in ductile materials, as well, but it does not lead to disintegration since there is sufficient ductility to absorb the strain from expansion along the interfaces.

Oxidation is not the only environmental sensitivity that can cause pesting in intermetallic materials. There is speculation that an acceleration of the pest rate in molybdenum disilicide is related to a hydrogen effect supplied by excess moisture in the atmosphere [63]. In recent years, studies have shown that some pest phenomena are actually a result of the combined mechanisms of oxidation and embrittlement [64-74]. Studies in oxygen-doped $NbAl_3$ have shown that surfaces with implanted oxygen layers do not react sufficiently to cause disintegration, and act as barriers to further diffusion of oxygen [68]. From this experiment it was concluded that the pest in niobium aluminide was the result of embrittlement from oxygen dissolution in the boundary adjacent matrix rather than the cation diffusion and oxide phase formation previously suspected. The embrittlement of the boundaries was the cause of disintegration in $NbAl_3$.

Evidence that gaseous species embrittle grain boundaries has been observed in traditional metals for decades. There are still many theories as to the exact nature of the phenomenon, but most mechanisms involve the dissolution of hydrogen, oxygen or nitrogen which affect the ductility of the material adjacent to the boundary as well as the surface energy of the boundary. It is suspected that the embrittling elements cause a drastic reduction in the "toughness" of the boundary by decreasing the ductility of the adjacent matrix material while altering the surface energy of the boundary to facilitate crack propagation. The surface energy is altered such that crack formation and propagation is facilitated, and the hardened boundary material does not deform plastically to absorb the crack energy. The boundaries, in effect, become so weak that internal stresses from otherwise negligible sources (i.e. slight thermal variations) may be strong enough to cause disintegration. Oxygen embrittlement was one of the first suspected causes of pest in $MoSi_2$ and there is still some speculation that it may play a role in the phenomenon [60]. Nitrogen is known to embrittle AgMg such that disintegration occurs at room temperature leaving behind particles comparable in size to the original grains [60].

Hydrogen, being the smallest atomic species, can diffuse rapidly through most materials, and does so below the detection threshold of most analytical techniques. As shown in Figure 2.21, hydrogen can be supplied by several mechanisms, transports by mulitple mechanisms and targets many different microstructural features as sites for embrittlement. Hydrogen is abundant in moist air and can rarely be eliminated, although it can be compensated for. Because of the precarious nature of hydrogen detection, many of the theories involving hydrogen embrittlement are still just theories, but there are some widely accepted notions concerning the observed phenomena. The proposed mechanism for embrittlement begins with the dissociation of atomic hydrogen from water by an oxidation reaction with an active metallic species. The "free" hydrogen is then able to diffuse through the material, often to regions of tensile stress in the lattice such as advancing crack tips, causing a decrease in the energy required in crack propagation. It has been shown that tensile ductilies of many intermetallics drop significantly in moist environments where hydrogen is abundant. The addition of alloying elements (e.g. B in Ni_3Al) has been shown to limit the extent to which hydrogen embrittles boundaries although the mechanisms by which these additions alter the embrittlement is still unclear [64, 69, 70, 72, 73].

2.4.2 High-Temperature Oxidation of Intermetallics

Passivation of materials in high temperature oxidizing environments is critical to components of gas turbine engines. The desired requirements for an ideal material would be the formation of a passivating scale which does not spall during the course of temperature cycles. As mentioned earlier, $MoSi_2$ is unique in its ability to form a silica scale at high temperatures, which acts as a diffusion barrier to further oxidation of the material. Unfortunately, most other intermetallics do not share this trait [62]. The silica scale on $MoSi_2$ remains amorphous which aids in its ability to resist spalling, and act as a
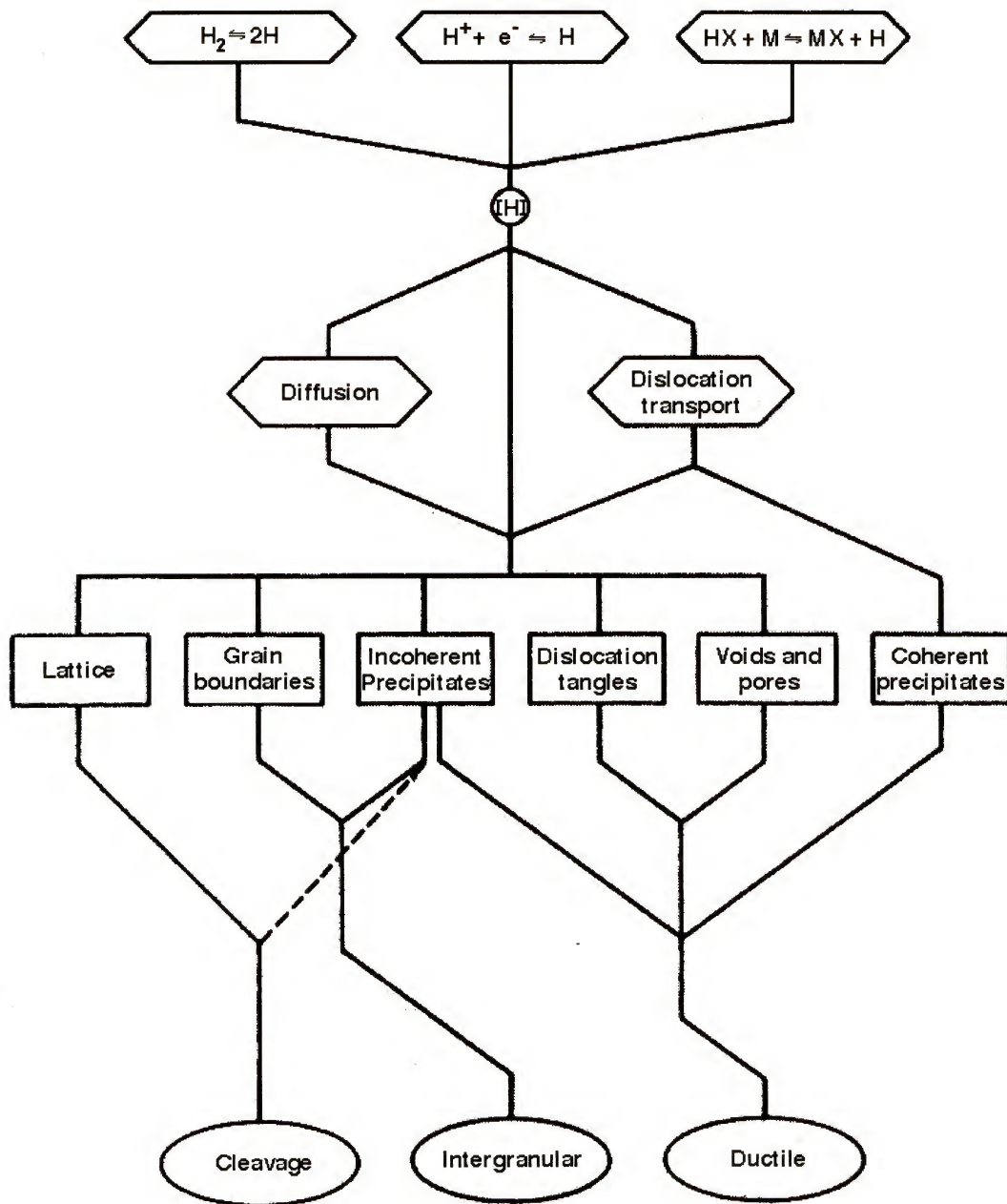
Figure 2.21 Flow diagram illustrating sources, transport paths and destinations of hydrogen leading to fracture mechanisms [75].

diffusion barrier. The oxides that form on most other intermetallics are crystalline in nature and, therefore, possess grain boundaries which can act as high diffusivity paths for further oxidation. Another unique characteristic of the scale on $MoSi_2$ is the fact that it is a single phase oxide, and not a mixture of oxide phases as in most intermetallics. Since the MoO_3 that forms on $MoSi_2$ volatilizes, the remaining scale is comprised entirely of SiO_2. The mixed crytalline oxides that form on most intermetallics possess interphase boundaries which can also act as diffusion paths for oxygen ingress.

Mechanisms of oxidation in intermetallics involve the formation of mixed oxide scales of varying morphologies, followed by diffusion of oxygen through the scale to the material, or diffusion of metal cations through the scale to the oxide surface. The oxide morphology is critical to the rate of further oxidation [39, 40, 62]. Oxide scale morphology is dependent on the composition of the base material as well as the oxidation characteristics of the individual metallic species present in the base material.

A departure from traditional parabolic diffusion rates can be allowed by short circuit diffusivity paths in the forming oxide scale [76, 77]. Layered oxides can reduce the diffusion of reacting species by providing complicated short circuit paths for diffusion, while columnar oxides can provide enhanced diffusion of reacting species by supplying direct diffusion paths between the materials and the free oxide surface (Figure 2.22). The example cases of columnar and layered oxide structures form the extreme ends of the spectrum of possible scale morphology. The real morphology of mixed oxide scales often lies somewhere between the two as do the oxidation rates [26, 61, 77].

2.5 Grain Boundary Phenomena

Grain boundaries are the interfaces that exist between individual crystals of differing orientation in a homogeneous solid. It is naive to assume that these boundaries are nothing more than two dimensional disruptions in the periodic order of a lattice, which act to only affect the mechanical properties of the material. The disruption in the bulk

Layered oxide Phases
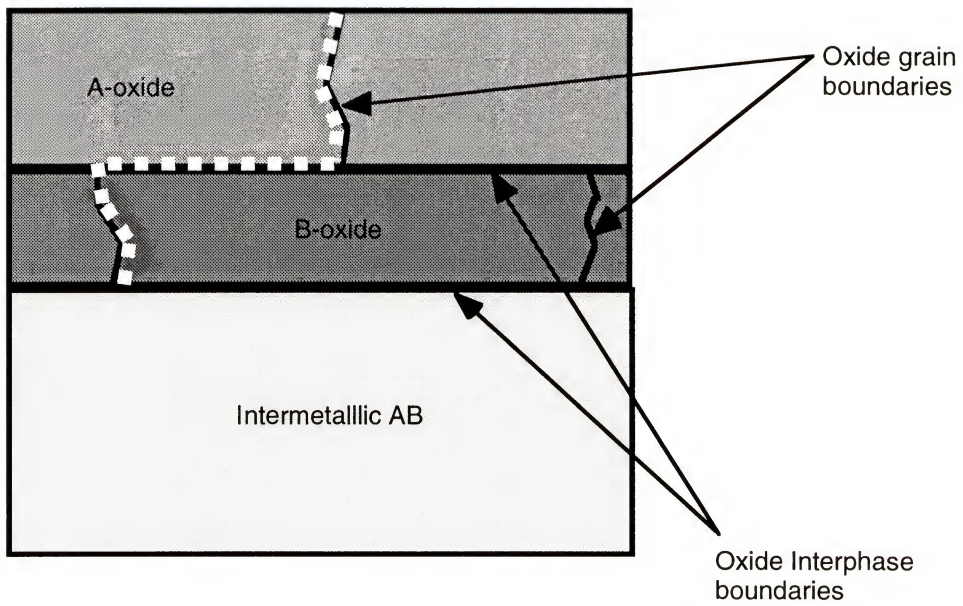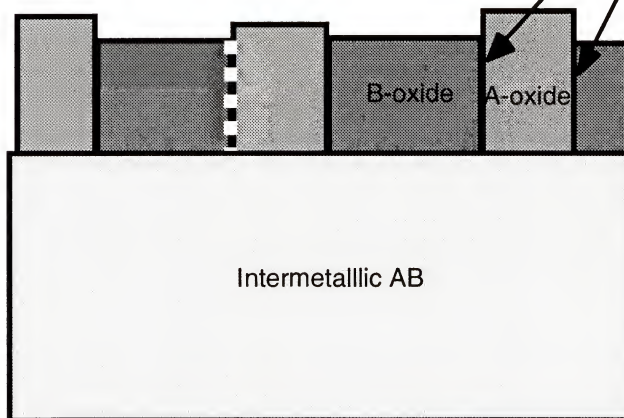

Columnar oxide phases

Figure 2.22 Schematic representation of mixed oxide morphologies. The white dashed lines indicate the short circuit diffusivity paths for the enhanced diffusion of either oxygen or reacting metal cations.

properties of the crystal associated with grain boundaries extends to the chemical properties as well. Grain boundaries can act as sinks for solute atoms rejected from solution, sites for the heterogeneous nucleation of secondary phases, and paths of enhanced diffusivity [78, 79]. In traditional metals, it has been shown that activation energies for grain boundary diffusion are often half those required for bulk diffusion at room temperature [78]. The chemical make up of grain boundaries can have direct consequences on the mechanical properties of a material by acting as sites for failure initiation and propagation due to the presence of secondary phases, embrittlement and stress corrosion cracking [76, 80]. In brittle materials, where the fracture path is most often intergranular, the grain boundary properties dictate much of the mechanical behavior of the material. Such is the case with intermetallics.

Energetically, grain boundaries are not favorable structures and have elevated energy compared to the bulk material. Eventually, a balance is reached between the driving force for boundary elimination and the ability to "move" boundaries out of the solid. The resulting structures reach a state of stability yet still have an interfacial energy associated with each boundary. The energy of these interfaces depends on the orientation between the adjacent grains, often referred to as the angle of the boundary. High angle boundaries exhibit more "misorientation" and have higher interfacial energies than low angle boundaries [79]. This elevated energy makes boundaries attractive as sites for nucleation of secondary phases. Three factors lead to the favorable formation of secondary phases at grain boundaries: 1) the variation in chemistry from the presence of material not incorporated into the matrix or solute atoms rejected from the matrix, 2) the reduction in surface energy from the formation of heterogeneous precipitates, and 3) diffusion along boundaries which enhances solute transport and expedites phase formation [79].

The presence of chemical segregation and secondary phases at boundaries can affect the environmental sensitivity of a material. Most of the literature involving the role of grain boundaries in environmental reactions concern traditional metal alloys. Little is known

about the surface energies and diffusion rates in grain boundaries of intermetallic compounds although the mechanisms observed in traditional alloys are expected to remain applicable [62]. Stringer established four major effects associated with the interaction of the environment with grain boundaries: 1) liquid metal embrittlement, 2) Intergranular corrosion, 3) intergranular stress corrosion cracking, and 4) grain boundary effects in high temperature oxidation processes [76]. Since it has been established that intermetallics are often susceptible to low temperature oxidation phenomena, it is expected that accelerated grain boundary transport plays a role in these mechanisms. As discussed in the section on observed pest phenomena, stresses from the formation of voluminous oxide phases can lead to disintegration of polycrystalline parts. The presence of oxidizing secondary phases at the boundaries could act as a mechanism to pest disintegration of a material that would not be susceptible to pest oxidation in the absence of the secondary phases.

2.6 The Al - SiC Equilibrium

The discovery of coupled particles of aluminum and silicon carbide in the grain boundaries of C40 during the course of this investigation necessitates a review of the properties of the Si-Al-C system with respect to formation and stability of the phases present in the system. The studies on this system have been driven largely by the desire to reinforce aluminum alloys with SiC particles. Work in the use of SiC reinforcements in aluminum alloys began in the 1970's [81]. Early experimenters were not equipped with a thorough understanding of the thermodynamics of the ternary system, thus compatibility of the Al and SiC phases was optimistically overestimated. The investigation into the equilibrium between pure aluminum and silicon carbide has also been clouded by the use of fiber coatings and alloying additions to the matrix which further reduce reactivity between the two phases. It has been shown that the two phases exhibit a precarious equilibrium at room temperature, which may be metastable in nature [81]. The possible reaction between Al and SiC is the following:

$$4Al + 3SiC = Al_4C_3 + 3Si \qquad (2.9)$$

This reaction was originally reported in the literature to proceed at high temperatures, when aluminum is in the molten state [82-85]. Viala showed that the reaction can occur at temperatures near the eutectic temperature of the Al-Si system (577°C) when both phases are in the solid state [81]. Formation of Al_4C_3 from Al and SiC has been recently observed at 450°C [82]. The mechanism of the reaction may explain why the phases appear to be in equilibrium at lower temperatures. Upon formation of the initial Al_4C_3 layer, silicon is rejected into the aluminum matrix. The presence of the silicon in aluminum shuts down the reaction by reducing the relative activity of aluminum [84]. This effect can be expected to intensify as temperature decreases and the solubility of Si in aluminum becomes negligible. Calculation of the driving force for the reaction at room temperature gives a negative change in the Gibbs free energy of 2.673 kJ/mol. This change, although mild, does indicate that these species are not in true thermodynamic equilibrium. Viala also showed that, at very high temperatures (1500°C), silicon carbide will precipitate from an aluminum liquid rich in silicon and carbon, leaving behind a silicon-containing aluminum solution. Upon cooling, the sluggish dissolution of these SiC particles allows them to remain in the microstructure despite the lower temperature instability of the two phases [81].

2.7 Properties of Al_4C_3

The properties of Al_4C_3 have been studied extensively as they pertain to the behavior of Al-SiC and Al-graphite composites [84, 86, 87]. The formation of Al_4C_3 at the interfaces of aluminum matrix composites is of concern since the properties of the composite materials are dictated by degradation of the reinforcements as well as the presence of a brittle phase between the reinforcements and the matrix. Aluminum carbide is found in composites that are produced by liquid infiltration. The thickness of the reaction layer is dependent on many factors including composition of the aluminum alloy,

temperature of processing, and presence of coatings on the reinforcements. The reaction layers that have been observed in most studies are on the order of several microns in thickness [87]. The two properties of Al_4C_3 that are of the most concern are its intrinsic brittleness and its extreme environmental sensitivity.

The environmental sensitivity of aluminum carbide is of most interest to this investigation. Aluminum carbide is notoriously susceptible to attack in moisture-containing environments. The dissolution of aluminum carbide in water is shown in the following reaction:

$$Al_4C_3 + 18H_2O = 4Al(OH)_3 + 3CO_2 + 12 H_2 \qquad (2.10)$$

It has been shown that submersion of SiC_p/6061 composites in room temperature water for 48 hours causes severe pitting around the matrix/reinforcement interface from the complete dissolution of aluminum carbide [82]. Aluminum carbide is also plagued by a sensitivity to atmospheric moisture as shown by this equation:

$$Al_4C_3 + 1.5H_2O + 2.25\ O_2 = 1.5C_2H_2 + 2Al_2O_3 \qquad (2.11)$$

Exposure of aluminum carbide to moist air environments will cause extreme surface degradation in a period of 120 hours at room temperature [82]. For these reasons, the suppression of aluminum carbide formation in aluminum matrix composites has been the focus of many of the alloying efforts in these materials.

2.8 Ternary Phase Diagrams

A phase diagram is a graphical representation of the stability of constituents in a chemical system as defined by thermodynamic variables (temperature, pressure and composition). A ternary phase diagram is such a depiction for a chemical system comprised of three atomic components. Part of this investigation involved the reassessment of the Mo-Si-Al isothermal diagram at 1400°C. The basis for the strategy of

this endeavor requires a review of some thermodynamic concepts involved in multicomponent reacting systems. There are two kinds of information to assess in the determination of a phase diagram, 1) the layout of the phases present, identity of those phases, and the univariant equilibria in which they participate, and 2) the true temperatures and compositions along the phase boundaries in the system [88]. The determination of the former was the goal of this investigation. To that end, the basic thermodynamic concepts of a three-component system will be discussed.

The Gibbs phase rule is the defining law of phase diagram behavior. The phase rule dictates how a diagram can be represented graphically by telling the number of variables that must be assigned to define the state of the system [89, 90]. The Gibbs phase rule is as follows:

$$f = c - p + 2 \qquad\qquad (2.12)$$

Where c is the number of atomic components in the system and p is the number phases involved in an equilibrium. A graphical representation on paper can display up to three "dimensions", but most often two dimensional depiction's are easier to interpret. Therefore, a system with two variable components can be represented in a clear manner by the definition of two independent axes. In binary (two atomic components) phase diagrams these two axes are often chosen to be temperature and composition (Note: in a binary system defining the fraction of one atomic species automatically sets the other, as both fractions must sum to unity). In a three component system, the fraction of two atomic species must be assigned to fully define composition for the system. For this purpose, ternary phase diagrams are usually plotted in triangular coordinates with the corners of an equilateral triangle depicting pure atomic species, thus allowing the selection of two independent atomic fractions. Setting the temperature and pressure as constants defines the graphical depiction as an "isobaric, isothermal" section of the diagram, though the term "isotherm" is used most commonly used to describe these figures. Looking at the Gibbs

phase rule we can now determine the maximum number of phases we can depict in in equilibrium in this system, allowing varying composition as our two degrees of freedom:

$$2 = 3 - p + 2 \qquad\qquad (2.13)$$

Solving for p, we find the maximum number of phases we can describe in equilibrium in this system is three. A three-phase equilibrium is represented by a "tie triangle" whose terminal ends represent the invariant compositions of the three phases in equilibrium. While shifting composition within a tie triangle will affect the relative amounts of the phases present, the compositions of the phases remain constant. By locating the three-phase equilibria in a ternary isotherm, the terminal compositions of three single-phase fields can be determined. These terminal compositions aid in determining the layout of phases present in the system. The other phase fields (single phase and two phase) must be assessed by the production of many alloys of incremented compositions to ascertain the true shape of the boundaries that border these equilibria. There are rules that govern the layout of phase diagrams which can simplify the process of determining an isotherm while greatly reducing the number of alloys that must be produced in the process [88]. The first rule is that "sides" of tie triangles must also be the terminal "tie line" of an adjacent two-phase field. It is impossible for a pair of three phase field to share an edge. The second rule is that the boundaries between one and two phase fields must always be convex with respect to the single phase field, and both must either project into or out any adjacent three phase field (Figure 2.23).
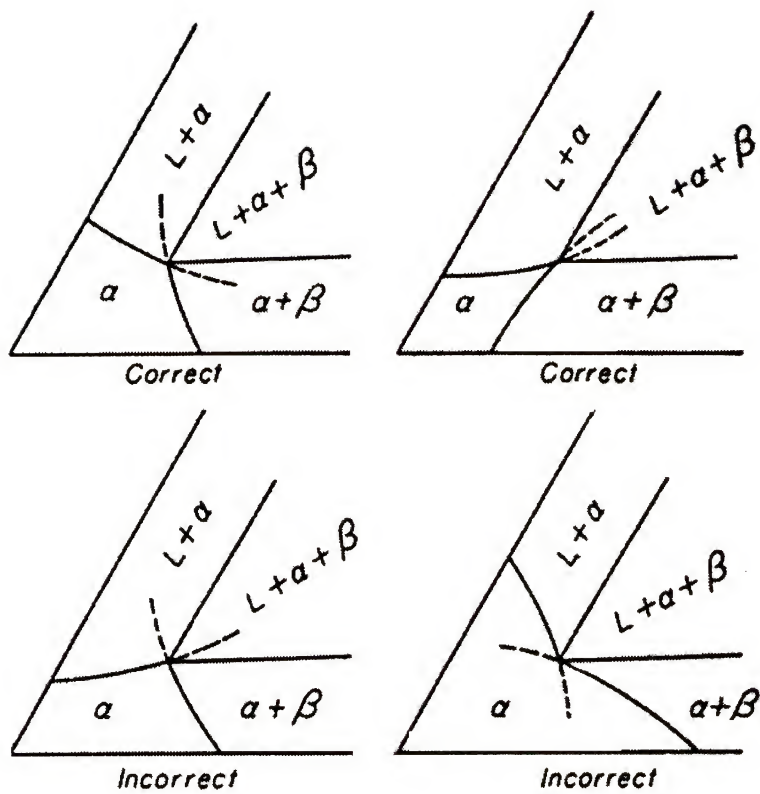
Figure 2.23 Possible arrangements of the boundaries of single phase fields in isothermal
sections of ternary phase diagrams. Labels indicate whether the arrangement is
allowed under the rules of free energy minimization [88].

CHAPTER 3
EXPERIMENTAL PROCEDURE

This investigation has encompassed three major areas in the study of the $Mo(Si,Al)_2$ C40 intermetallic compound: 1) processing 2) phase equilibria 3) environmental behavior. The processing investigation involved the assessment of production methods on the basis of reproducibility and efficiency for several techniques of hot-pressing charge production. The phase equilibria study was performed to reevaluate the Mo-Si-Al ternary isotherm at the desired processing temperature for the samples in this study. Finally, the investigation of the environmental behavior grew from observations of phenomena noted throughout the course of the aforementioned efforts. These three topics differ in both scope and nature of investigation. Accordingly, the proceeding information concerning the experimental procedure, results and conclusions will be addressed by topic.

3.1 Raw Materials

The materials used in this investigation were chosen as the highest purity commercially available materials to eliminate the possibility of contamination affecting the results of the study (Table 3.1).

Table 3.1 Listing of raw materials

Material	Size	Purity	Supplier
Molybdenum (rod)	3mm diam.	99.7 % WB	Johnson Matthey
Silicon (pieces)	<10 mm	99.9995 % WB	Johnson Matthey
Aluminum (shot)	<10 mm	99.7 % MB	Johnson Matthey
Molybdenum (powder)	<44 μm	99.999 % WB	Cerac
Aluminum (powder)	<44 μm	99.5 % MB	Johnson Matthey
$MoSi_2$ (powder)	<149 μm	99.995 % WB	Cerac
WSi_2 (powder)	<149 μm	99.995 % WB	Cerac
$TiSi_2$ (powder)	<149 μm	99.95 % WB	Cerac

3.2 Sample Processing

All samples in this investigation were produced by compaction of powders in hot uniaxial compression. The variation in processing schemes lies in the methods by which the powder charges were produced. Arc-melting and comminution, mechanical alloying and blending of powders were the different techniques compared in this study. The powder charges were loaded into graphite dies that had been lined with boron nitride spray and graphite paper. Samples were heated to 1100°C under a vacuum of $<10^{-3}$ torr, with no ram pressure applied, and held for one hour. The temperature was then increased to 1400°C and the chamber was partially back filled with argon to one-half atmospheric pressure. A pressure of approximately 45 MPa was then applied to the sample by the hydraulic ram. This condition was sustained for three hours by continually adjusting ram pressure to maintain constant load. The Sample temperature was measured with a two-color optical pyrometer which had been calibrated with a Type B (Pt-Rh) thermocouple to be within 25°C accuracy. Samples were allowed to cool in the hot press chamber to below 700°C within 30 minutes. Upon removal from the dies, contact surfaces were ground with silicon carbide paper to remove any reaction layer from the graphite paper. All samples for the single phase processing optimization study were produced with the same nominal composition:

Molybdenum	33.333% at.
Silicon	46.667% at.
Aluminum	20.000% at.

3.2.1 Arc-melting and Comminution

Molybdenum rod, silicon lump and aluminum shot were arc-melted under gettered argon to produce 25 gram buttons. To reduce volatilization, molybdenum was placed on top of silicon and melted first, then placed on top of the aluminum and melted around it. Buttons were turned over and remelted five times to ensure homogeneity. The pellets were

crushed with a steel crushing device and ground by hand with a mortar and pestle. The resulting powder was sieved and reground to a final powder size of <74 μm. The powder was analyzed by XRD for phase verification and consolidated by the method discussed above.

3.2.2 Mechanical Alloying

Elemental powders of molybdenum, silicon and aluminum were mechanically blended for preparation of the mechanical alloying process. To minimize the amount of incorporated oxides, the powder blend was stirred and placed into a steel alloying vial under a high purity argon atmosphere. A milling media of steel balls was added to the charge at a weight ratio of 3.5 to 1 (milling media to charge ratio). The vial was sealed in the argon glovebag to contain the inert atmosphere. The vial was placed on a Spex 8000 Mixer/Mill and milled for 12 hours. After completion of the milling, the charge was removed from the vial in an inert argon atmosphere and transferred to the graphite die for hot pressing. A small portion of the charge was retained for X-Ray powder diffraction analysis to assess the extent of formation of the C40 phase as a result of mechanical alloying.

A later experiment involved the use of an aluminum oxide vial and spherical alumina milling media to eliminate the contamination by iron picked up from the steel milling apparatus. All other aspects of processing remained the same. Spalling of the alumina milling media was detected and this method dismissed as a possible route for processing.

3.2.2 Hot Pressing of Blended Powders

Powders of molybdenum disilicide, molybdenum and aluminum were placed in a plastic vial and tumbled for one hour to break up agglomerates and mechanically blend the powders. The blend was placed in the graphite die under normal atmospheric conditions

and hot pressed according to the standard scheme with the intent of C40 phase formation during the heating cycle of the press. No pre-pressed powders were X-Rayed since a reaction would not be expected from blending under ambient conditions.

3.3 Mo-Si-Al Ternary Phase Diagram Reassessment

Vital to this investigation was the development of a "working phase diagram" for the Mo-Si-Al ternary system. The term "working phase diagram" is used since the goal of the assesment was not to determine the exact compostions of the phases participating in all equilibira. The approach was based on determining the presence and location of the ternary phases in the system, and the nature of their equilibira with the C40 phase field. Therefore, a phase diagram was established that provides an accurate placement of phase boundaries for the C40 phase field, and relations to adjacent phases.

3.3.1 Alloy Composition Selection

Seven alloy compositions were chosen based on the location of phases in the Brukl isotherm with the strategy of producing multiphase structures having compositions near the terminal ends of the C40, C54, T1 and Mo_3Al_8 phase fields (see Figure 3.1). The compositions were chosen for their locations in two- and three-phase fields, to provide the most information possible about the boundaries of adjacent phases. Samples were produced from powders of $MoSi_2$, Al and Mo. The powders were mechanically blended to break up agglomerates and insure homogeneity, then charged into graphite dies and densified by the standard hot pressing scheme.

3.3.2 Equilibration and Analysis

The fully dense compacts were heat treated in a tube furnace at 1400°C under flowing gettered argon for 50 hours to equilibrate the microstructures (alloys 5, 6 and 7 did not undergo 50 hour heat treatment as they displayed two-phase eqilibrium structures after

Figure 3.1 Compositions selected from the Brukl isotherm for assessment of the 1400°C isothermal phase diagram.

the intitial hot pressing). The alloys were sectioned, polished and analyzed for both qualitative and quantitative phase identification. The remaining sections of the heat treated alloys were ground in a high purity alumina mortar and pestle and examined by powder X-Ray diffraction.

3.4 Atmospheric Testing

The environmental degradation of the C40 compound was initially observed after long term exposure to room temperature air. The 17 month duration of exposure made replication of the effect at room temperature prohibitively slow. Therefore, it was decided that mild heating of the material would be used in an attempt to accelerate the effect without altering the mechanism at work. Samples were exposed to laboratory air at 200°C in a horizontal tube furnace for periods of 20, 40, 80 and 160 hours. Initial exposure treatments did not involve any atmospheric regulation, thus the ends of the furnace tube were left uncovered. When it was observed that moisture had an effect on the phenomenon, subsequent treatments involved the use of commercial grade air bubbled through a warm water bath to increase the moisture content of the air in contact with the samples (see Figure 3.2).

One control sample was vacuum encapsulated in a quartz tube and heated at 200°C for 160 hours to assess the need for atmosphere to induce attack. All but one sample were polished with 6 micron diamond suspension before exposure to produce mirror finishes which aided in the identification of attack. One sample was prepared for atmospheric exposure by producing a fresh fracture surface to assess the effect of grain boundary chemistry on the nature of attack. After exposure, samples were analyzed for chemical and topographical changes by SEM, EDS and optical microscopy.
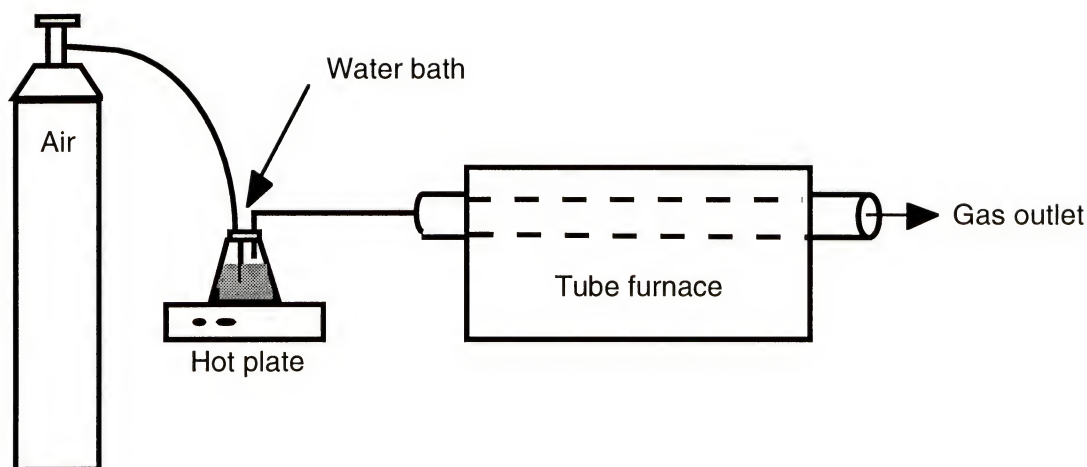
Figure 3.2 Schematic of environmental exposure apparatus.

3.5 Analytical Techniques

3.5.1 Metallographic Preparation

Samples were prepared by the following standard metallographic techniques for inspection by optical microscopy, secondary electron microscopy, backscattered electron microscopy and EDS and WDS. Samples were sectioned (if necessary) with a low speed diamond saw, and mounted in standard epoxy mounts. Grinding was performed on wet silicon carbide papers from 120 to 1200 grit folowed by polishing with a six micron diamond suspension on napless cloth. In cases where the surface condition was critical, the samples were polished with a 0.2 micron silica suspension on a Vibramet polisher. After polishing, samples were placed in a sonically vibrated methanol bath to remove any grinding and polishing media embedded in the surface. Scanning electron microscopy was performed with JEOL 35CF and JEOL 6400 microscopes the latter equipped with a Tracor System II EDS system. Wavelength dispersive spectroscopy was performed on a JEOL 733 SUPERPROBE using Mo, SiC, Al, Al_2O_3, W and Ti standards. The JEOL 733 SUPERPROBE was also employed in the production of X-ray dot maps.

3.5.2 X-Ray Diffraction

Both powder and consolidated bulk samples were examined by X-ray diffraction (XRD). The powders were placed on a glass slide using a drop of a quick drying organic solution which acted as an adhesive. Some samples were crushed after consolidation to create powder for the method just mentioned. The bulk samples were cut into thin sections using a low speed diamond saw, polished, and mounted on a glass slide with wax. Since bulk samples were fine polycrystals, the sections provided adequate diffraction for the analysis. The base of the glass slide was layered with tape to bring the surface level with the thickness of the thin section so the diffractometer would read the correct angles of diffraction. All XRD analysis was performed in a Philips APD 3720 diffractometer.

3.5.3 Auger Electron Spectroscopy

Auger electron spectroscopy (AES) was used for analysis of the grain boundary chemistry of the $Mo(Si,Al)_2$ phase. Due to the adsorption of atmospheric species affecting the grain boundary behavior, samples were fractured in the high vacuum ($<10^{-9}$ torr) chamber of the system immediately before analysis to avoid any contaminants. A Perkin-Elmer PHI 660 Scanning Auger Multiprobe equipped with an in-situ fracture stage was used for this analysis. Special sample preparation was required to produce the necessary sample for the fracture study (see Figure 3.3). Three millimeter diameter rods were cut longitudinally from hot pressed pellets by electric discharge machining. The rods were cut to the specified length with a low speed diamond saw and then polished with fine silicon carbide paper to improve surface quality. Since the materials in this study all exhibit very low toughenss the fracture notch geometry was assumed to be non-critical to the intiation of fracture and was machined in by hand with the low speed diamond saw. All AES samples were placed in an ultrasonically-vibrated bath of acetone, followed by ethanol, then finally methanol to remove any volatile species that would disrupt the high vacuum of the chamber. Once inside the chamber, the samples were placed in the fracture stage and the

SPECIMEN
LONG END

.45

.000 ± .010

MODEL 192 FRACTURE
SPECIMEN HOLDER

SET SCREW

.80

.45

90°±5°

$.125^{+.000}_{-.002}$ DIA.

.085 DIA.

.002 RAD. MAX.
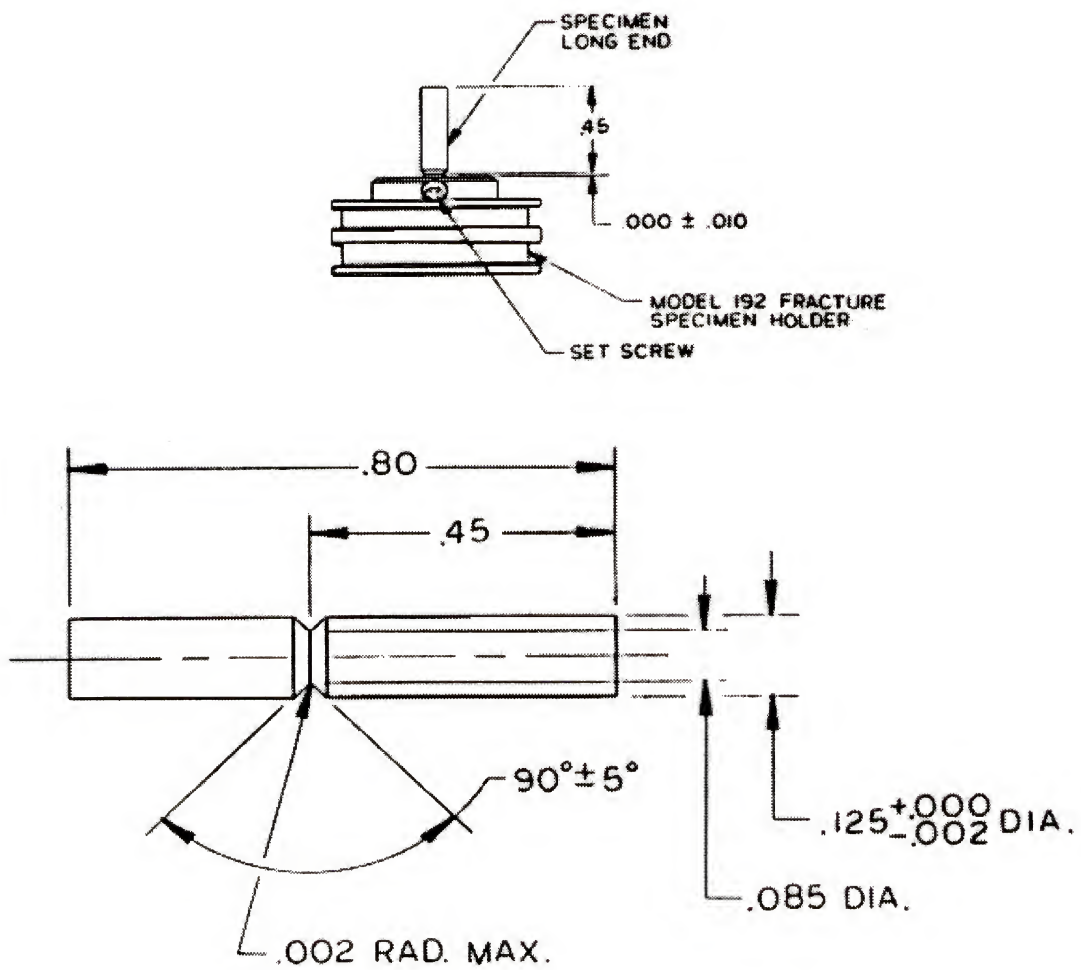
Figure 3.3 Sample fracture stage and dimensions for AES in-situ fracture experiment.

hammer device was actuated by striking the external portion of the device with a rubber mallet. Spectra were obtained from all initial fracture surfaces to asses the chemistry of the grain boundaries. Depth profiles were obtained by continually taking spectra while milling the surface by ion sputtering.

3.5.4 Transmission Electron Microscopy

For transmission electron microscopy (TEM) analysis, samples were prepared from the same hot pressed samples used for the other analyses. Thin sections were cut on the low speed diamond saw, and ground to approximately 300 micron thickness. Three millimeter disks were cut from the thin sections with an ultrasonic drill and silicon carbide abrasive media. The resulting disks were mounted and polished to approximately 200 micron thickness. The disks were dimpled to 20 micron thickness and ion-milled to produce the thin area for analysis. TEM was performed on JEOL 200CX, JEOL 4000FX, and Philips 420 microscopes, the latter two equipped with standard attachments.

CHAPTER 4
RESULTS AND DISCUSSION

4.1 Single Phase Processing Optimization

The first step in this investigation was to select an appropriate powder processing scheme for the production of dense, nearly-single-phase Mo(Si,Al)$_2$ C40. The reason for the term "nearly single-phase" comes from the previously mentioned fact that oxide particles are often incorporated into final powder compacts. Since it had been shown in previous studies that additions of aluminum to MoSi$_2$ powders reduced the existing silicon dioxide to form aluminum oxide, the powder-processed samples in this investigation were expected to contain a small amount of aluminum oxide. Part of the goal of this process optimization was to minimize the fraction of secondary phases so that the true properties of polycrystalline C40 could be investigated. The other aim of optimization was to identify an efficient and reproducible production method for nearly single phase material. Each of the processing techniques will be discussed on the basis of these two factors.

4.1.1 Arc-Melting and Comminution

Despite efforts to remelt samples for homogenization, the resulting arc-melted buttons showed evidence of incomplete homogenization. Continued attempts to melt the samples only resulted in vaporization of material and an unacceptable shift in composition. It was assumed that despite complete homogenization, the samples would still maintain the correct overall composition, and were processed according to the original procedure. The buttons were easily crushed into coarse powders measuring <1680 microns by sieving. The further comminution of these coarse powders proved to be the rate limiting step of the process. All grinding of powders was performed by hand using a high-purity, alumina

59

mortar and pestle. The powders were ground to <200 mesh in an attempt to limit the grain size in the resulting compacts. It required 10 hours of grinding to produce the ten grams of powder required for an adequate hot pressing charge. Powders produced by this method were shown by XRD to be mostly single-phase C40 (Figure 4.1), indicating that sufficient homogenization had occurred. Samples were then hot pressed and the resulting compacts were analyzed.

Bulk XRD of the samples showed that the compacts remained mostly single-phase C40 (Figure 4.2). Electron microprobe analysis of the resulting compacts revealed the matrix to be of the target composition in the C40 single phase field with the darker regions in the electron micrograph indicating alumina and porosity (Figure 4.3) . It is not clear as to the extent of porosity in the sample, since some of the dark regions that appear to be porosity could easily be from pull-out of alumina particles during polishing. It was decided that as long as the secondary phases observed in the microprobe were either alumina or
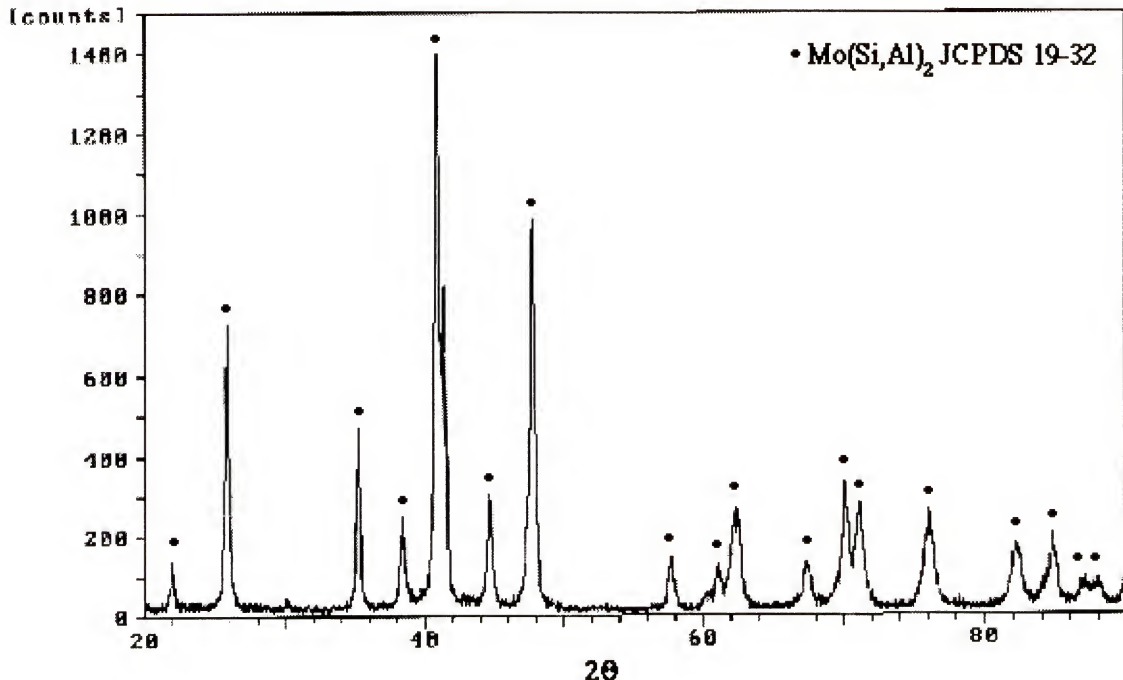
Figure 4. 1 Spectrum obtained from XRD of pre-pressed powders produced by arc-melting and comminution of Mo, Si and Al.
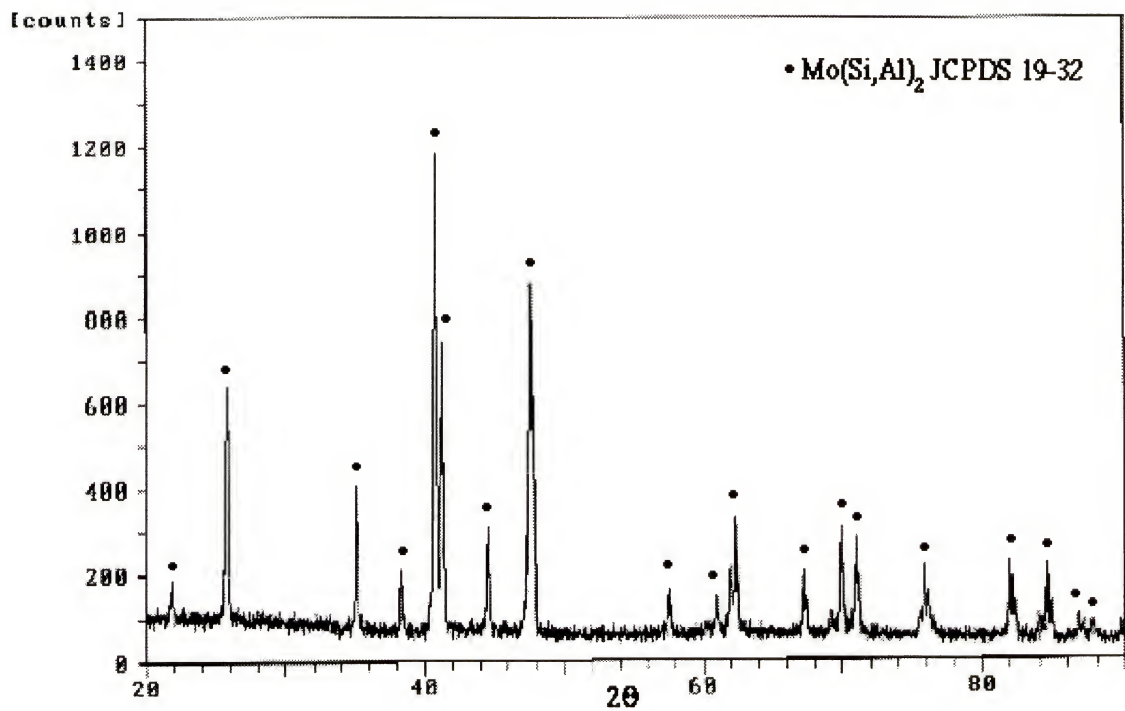
Figure 4.2 Spectrum obtained from XRD of hot pressed powders produced by arc-melting and comminution of Mo, Si and Al.
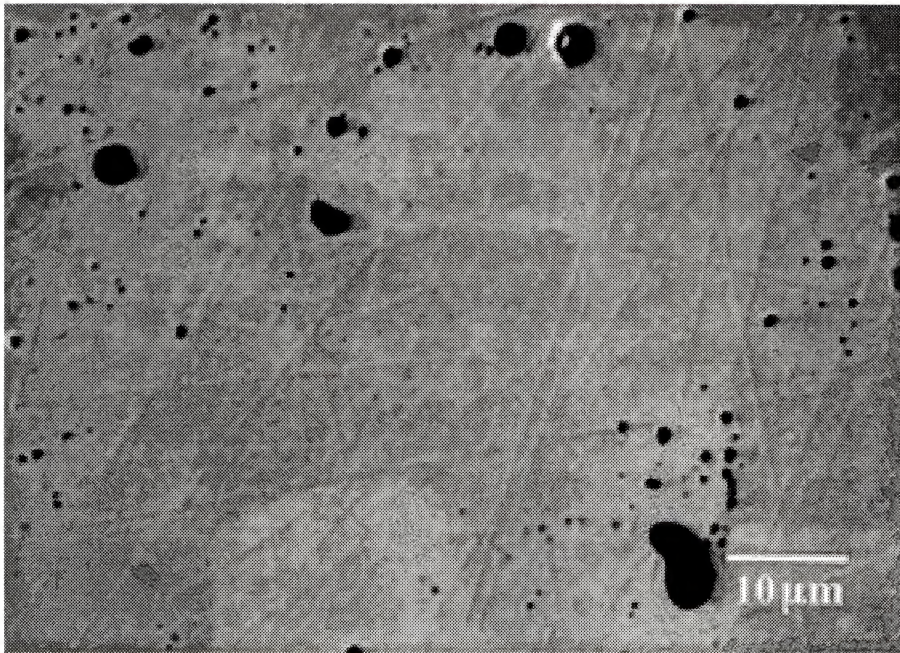
Figure 4.3 Backscattered electron image of hot pressed samples made from powders produced by arc-melting and comminution of Mo, Si, and Al. The light gray matrix is C40, the black regions are porosity and/or aluminum oxide.

porosity then no clear distinction would be necessary. This being the first method of processing attempted, it was impossible at this time to gauge the success of minimizing size and number of oxide inclusions and pores. This sample then became the benchmark for further comparison. This sample processing method was not investigated further due to the lengthy comminution involved in the production of the powders. It was clear from the EMPA, XRD and EDS results that the microstructure contained all of the expected constituent phases, but the difficulty in powder production made the processing route unappealing from the standpoint of efficiency. It was also suspected that because of the difficulty in comminution there would be little hope of refining the grain size in the final compacts by further reduction in powder size.

4.1.2 Mechanical Alloying

X-Ray diffraction analysis of the mechanically alloyed powders indicated a nearly complete conversion of the powders to the C40 compound (Figure 4.4). After the powders were pressed, inspection of the microstructure revealed a large amount of a high average-atomic-number phase (Figure 4.5). Analysis by EDS of this phase indicated high levels of iron, which is suspected to be a contaminant from the steel milling media and vial. Electron microprobe of the particle shows the stoichiometry to be consistent with the Mo_5Si_3 T1 compound containing Fe substituted for Mo.

While the presence of the T1 phase in the compacts made these samples unsuitable for further testing, it was noted that the refined scale of the microstructure was attractive from the standpoint of greater control of the grain size with this technique. It was clear that the iron picked up from the vial and media was partitioning to the T1 phase, thus making it an unacceptable contaminant. Since iron contamination is unavoidable when using steel vials and milling media, it was decided that an alumina vial and media would be used to further explore this processing route. Visual inspection of the resulting powders revealed that the media had spalled significantly during the milling procedure. The powders were hot
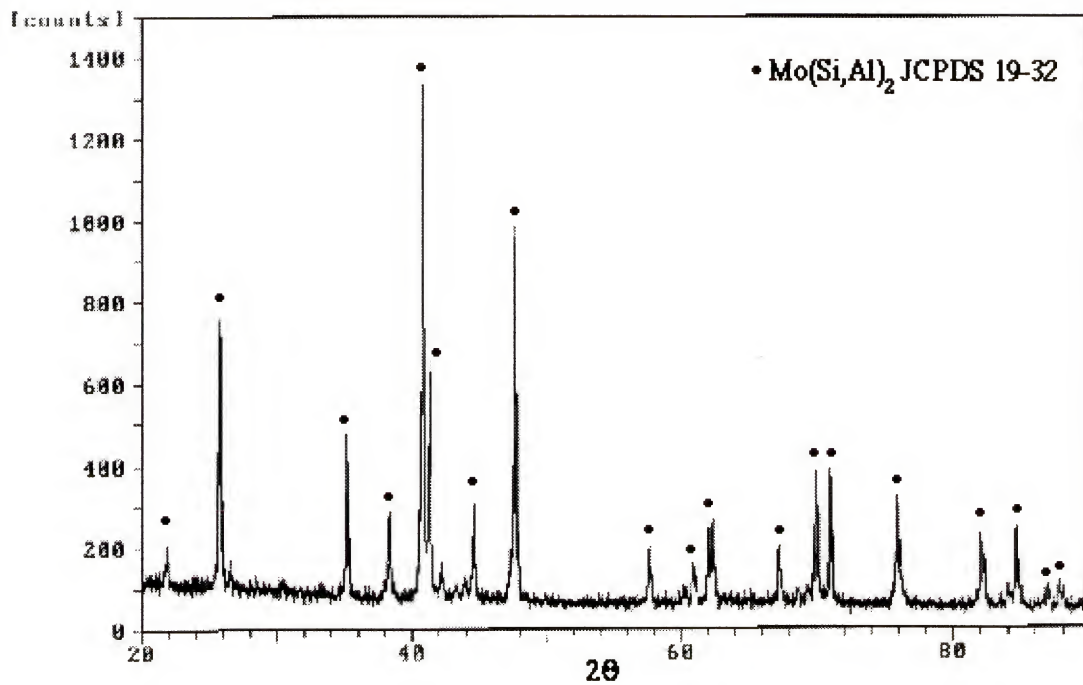
Figure 4.4 XRD spectrum obtained from Mo(Si,Al)$_2$ powders produced by mechanical alloying. Note: other small peaks appear consistent with the T1 phase.
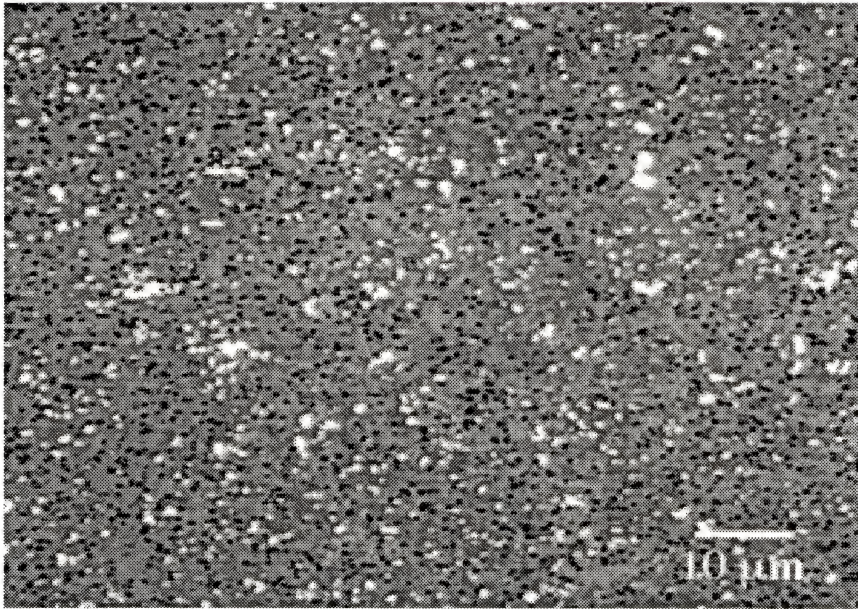
Figure 4.5 Backscattered electron image of hot pressed C40-Mo(Si,Al)$_2$ powders produced by mechanical alloying. The light gray regions are C40, the dark regions are oxide particles and/or porosity, and the white regions are iron containing T1 phase.
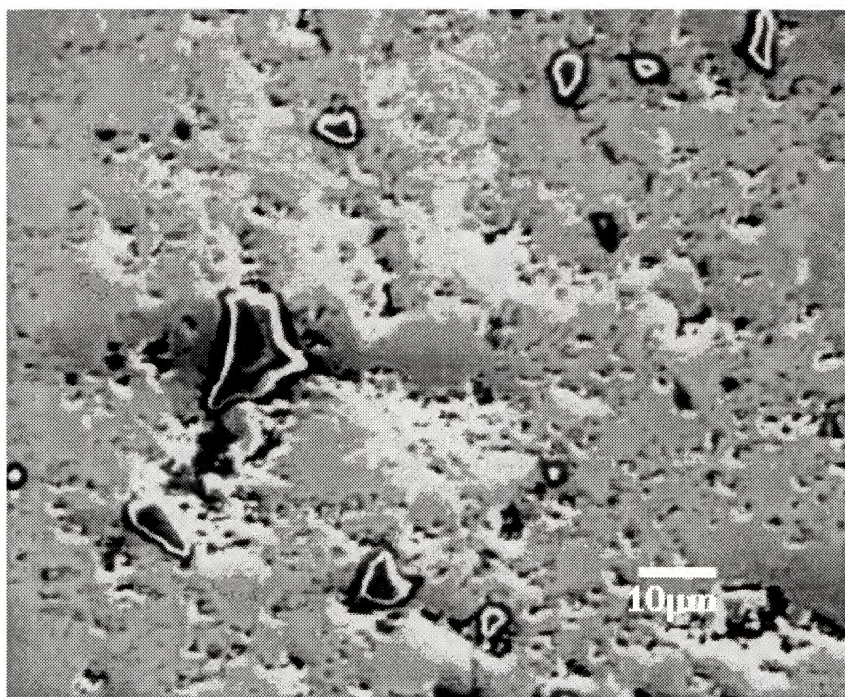
(a)
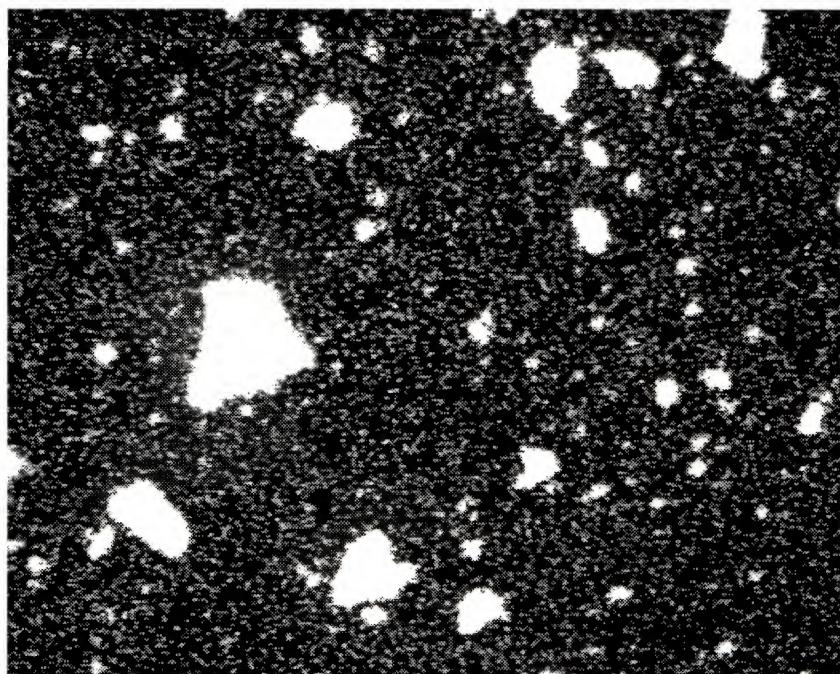
(b)

Figure 4.6 Micrographs of hot pressed C40 -Mo(Si,Al)$_2$ powders produced by mechanically alloying with an aluminum oxide vial and media. a) Secondary electron image of the microstructure with significant charging (bright regions) due to the electrical insulating properties of alumina. b)   Aluminum K$_\alpha$ dot map produced from the same region as the secondary electron image. White regions indicate high aluminum concentration.

pressed despite this observation in order to allow inspection of the alumina particles as well as an assessment of the extent of C40 phase formation. During microscopic analysis, alumina particles were observed to be on the order five to ten microns in diameter which made them unacceptable additions to the microstructure (Figure 4.6). It should also noted that there was no way of predicting the spall rate of the milling media; thus, little reproducibility was expected from this technique. Because of these complicating factors, mechanical alloying was discarded as a processing scheme for further investigation.

4.1.3 Hot Pressing of Blended Powders

As mentioned in the previous chapter, there was no reason to expect any reaction between powders blended at room temperature, thus, XRD was not performed on the pre-pressed powders. Electron microprobe analysis indicates complete formation of the $Mo(Si,Al)_2$ C40 phase during the hot press procedure (Figure 4.7). There was no variation in the matrix composition throughout the sample which was taken as evidence of complete reaction and equilibration of the final microstructure. To further characterize the microstructure, X-Ray dot maps were obtained to verify that the second phase produced from the process was indeed alumina (Figure 4.8). Transmission electron microscopy (TEM) was also used to verify the identity of the alumina secondary phase (Figure 4.9). Due to the relative ease of this method of processing, it was decided that optimization of the powder blend technique should be attempted.

Since the primary goal of this investigation was to study the properties of the single phase $Mo(Si,Al)_2$ C40 compound, optimization in processing of the blended powder technique was now focused on the minimization of secondary phases in the final dense compacts. Since the oxides that are incorporated during the process come from the surfaces of the powder charge, the amount of powder surface area was reduced by increasing particle size of the raw material powder. The molybdenum disilicide used in the powder blend was changed to allow an increase in particle size (<44 microns to <149
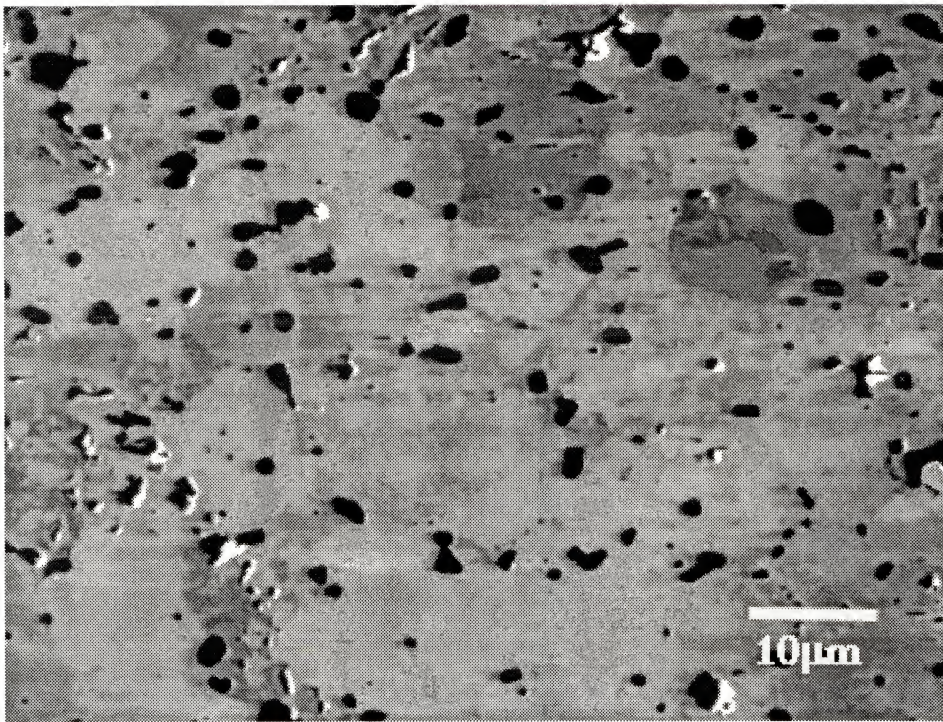
Figure 4.7 Backscattered electron image of the hot pressed powder blend. Powder blend consisted of Mo, $MoSi_2$ and Al podwers Gray regions are C40-Mo(Si,Al)$_2$, dark regions are alumina and/or porosity.
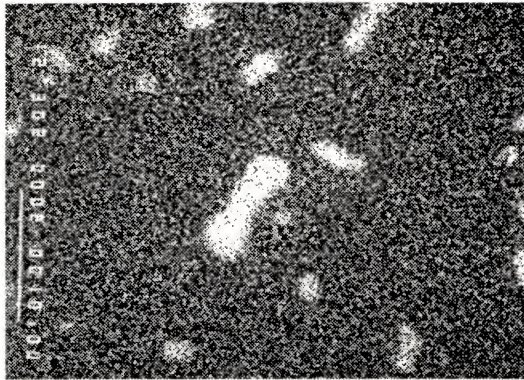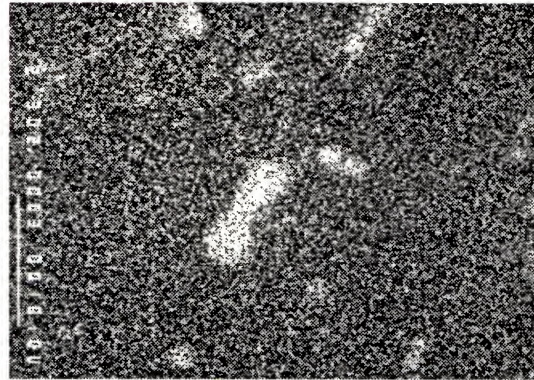
(a)   (b)
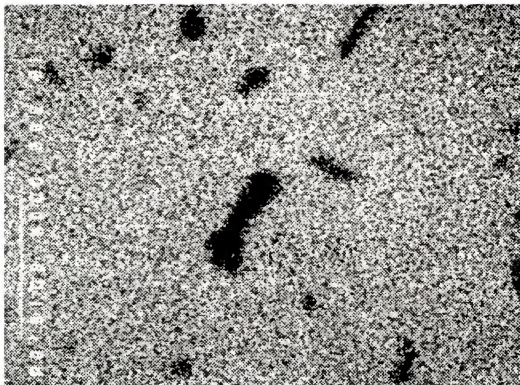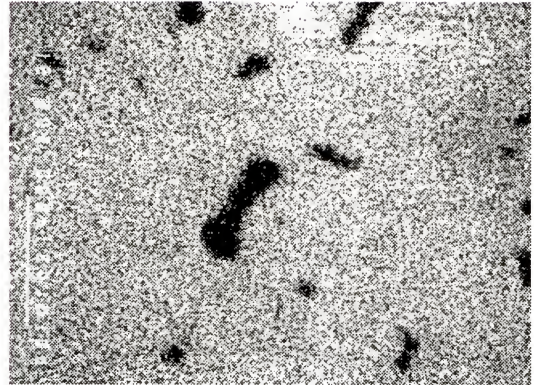
(c)   (d)

Figure 4.8 X-Ray dot maps of second phase particles in a C40-Mo(Si,Al)$_2$ sample
produced from blended powders. a) Aluminum K$_\alpha$ dot map, b) Oxygen K$_\alpha$ dot
map, c) Silicon K$_\alpha$ dot map, d) Molybdenum L$_\alpha$ dot map.
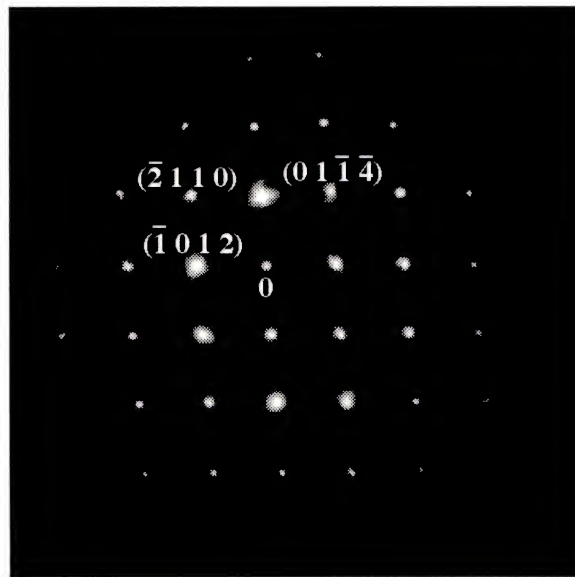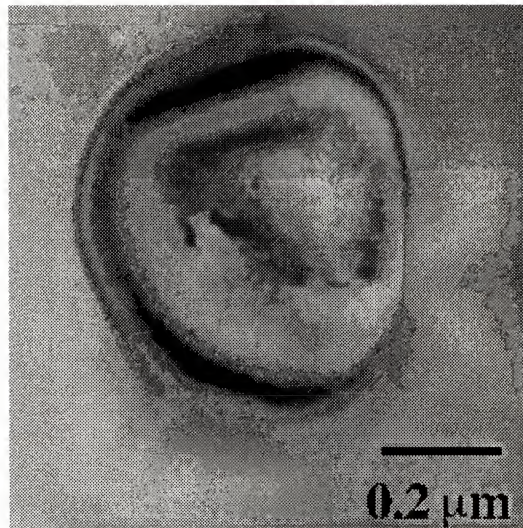
Figure 4.9 Transmission electron microscopy of an alumina particle in the C40 matrix. a) Bright field image of the alumina particle. b) Selected area diffraction pattern of the particle **B**=[0 2 $\bar{2}$ 1].

microns). The blending technique was employed in the same manner as before, and the resulting compacts were analyzed.

Bulk XRD of the samples produced from the larger powders indicates the formation of the C40 phase (Figure 4.10). Electron microprobe analysis revealed a decrease in both the size and number alumina particles versus the samples produced from smaller powders (Figure 4.11). It is suspected that the formation of an aluminum-rich liquid upon heating of the powders acts as a sintering aid, thus reducing much of the porosity seen in the other techniques. This improvement in the microstructure marked the most significant progress in the process optimization. The powder blending technique was notable for both simplicity and reproducibility.
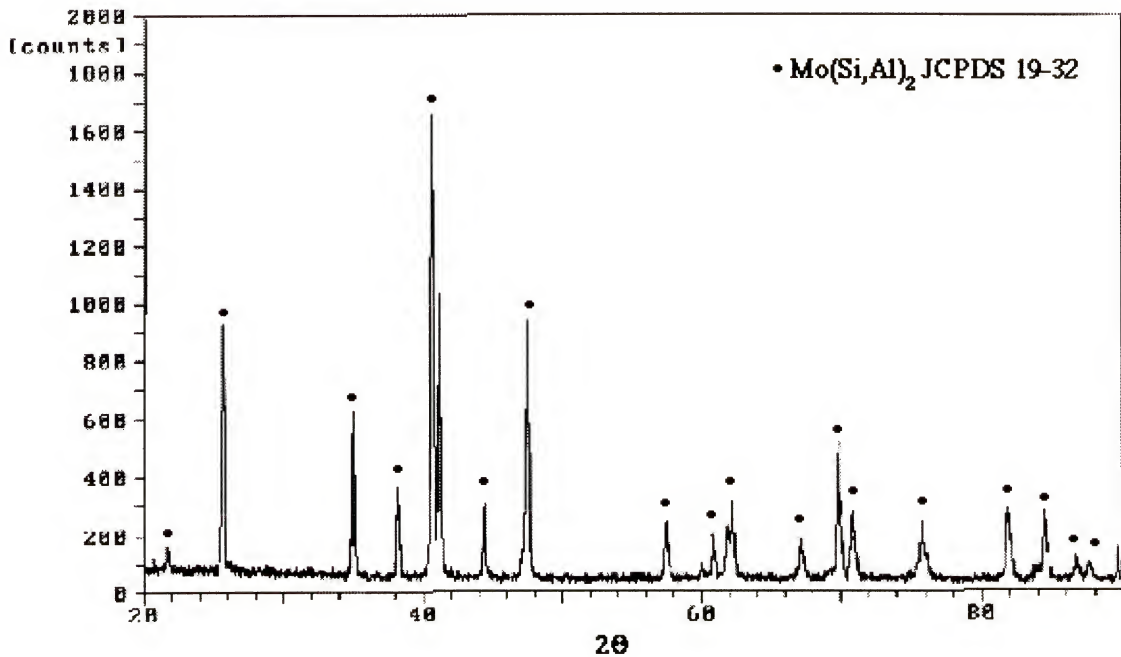
Figure 4.10 Spectrum obtained from XRD of a section of a compact pressed from blended powders of Mo, $MoSi_2$, and Al to form $C40-Mo(Si,Al)_2$.
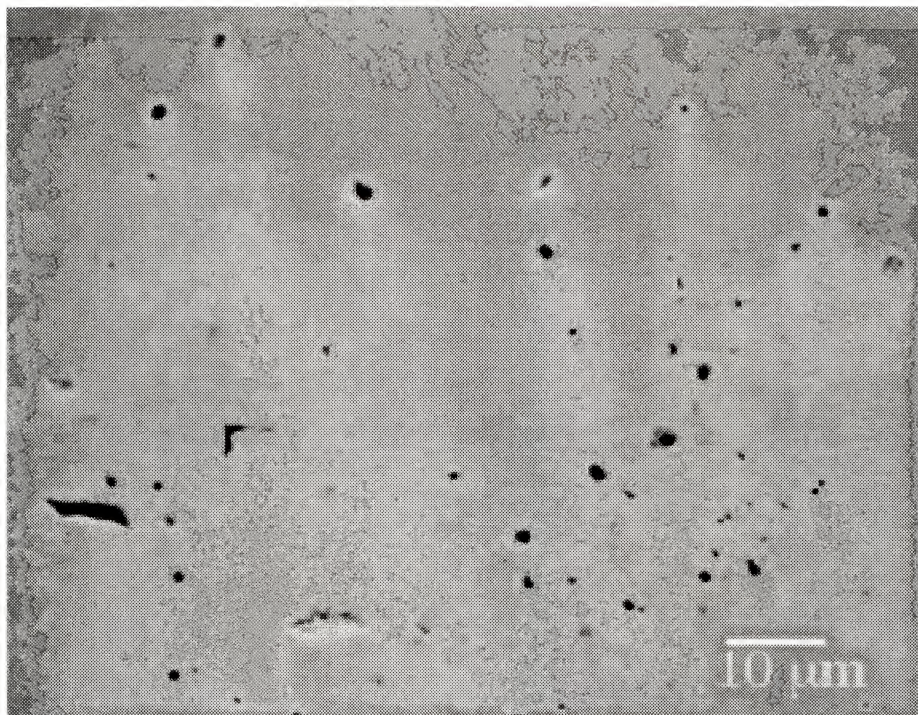
Figure 4.11 Secondary electron image of a hot pressed C40-Mo(Si,Al)$_2$ sample produced with large (-200 mesh) MoSi$_2$ powder. The gray area is the C40 phase and the dark regions are alumina and/or porosity.

4.2 Assessment of the Mo-Si-Al Ternary Isotherm at 1400°C

The isotherms proposed for the Mo-Si-Al system by Brukl and Yanigahara display discrepancies with each other and with recent experimental findings. During the course of process optimization, a liquid phase was present in alloys of higher aluminum content heated above 1500°C. The liquid phase, which was ejected from the hot pressing die during the heating cycle, was collected as a solid from the base of the hot pressing apparatus and ground for identification by XRD (Figure 4.12). The ejected liquid was discovered to be mostly single phase C40. The resulting compact did not appear to be significantly shifted from the target composition.   This finding brought into question the claims made in the Yanigahara diagram, which shows extensive solid phase stability of the C40 phase across the 1550°C isotherm. This lack of consistency with available diagrams made process optimization difficult. Since processing appeared to be adequately reproducible at 1400°C, it was decided that a reassessment of the 1400°C isotherm should be performed.

A series of seven alloys was produced with the compositions presented in section 3.3.2 of this document. Figures 4.13 through 4.17 show the microsturctures of the alloys used in the assessment. Identification of the phases in these alloys is discussed in the proceeding subsections. Table 4.1 shows the measured compositions grouped according to their respective phase equilibria. Each phase was measured in four random locations throughout the individual alloy microstructures. Alloys 2, 3 and 4 were found to lie within the same three-phase field, therefore, the compositions were averaged together due to their overlap. By plotting the EPMA results on triaxial coordinate paper, an isothermal section was constructed by overlapping data from each of the individual multiphase alloys. Each phase equilibrium will be discussed to address the specific issues raised by the conflicting Brukl and Yanigahara isotherms.
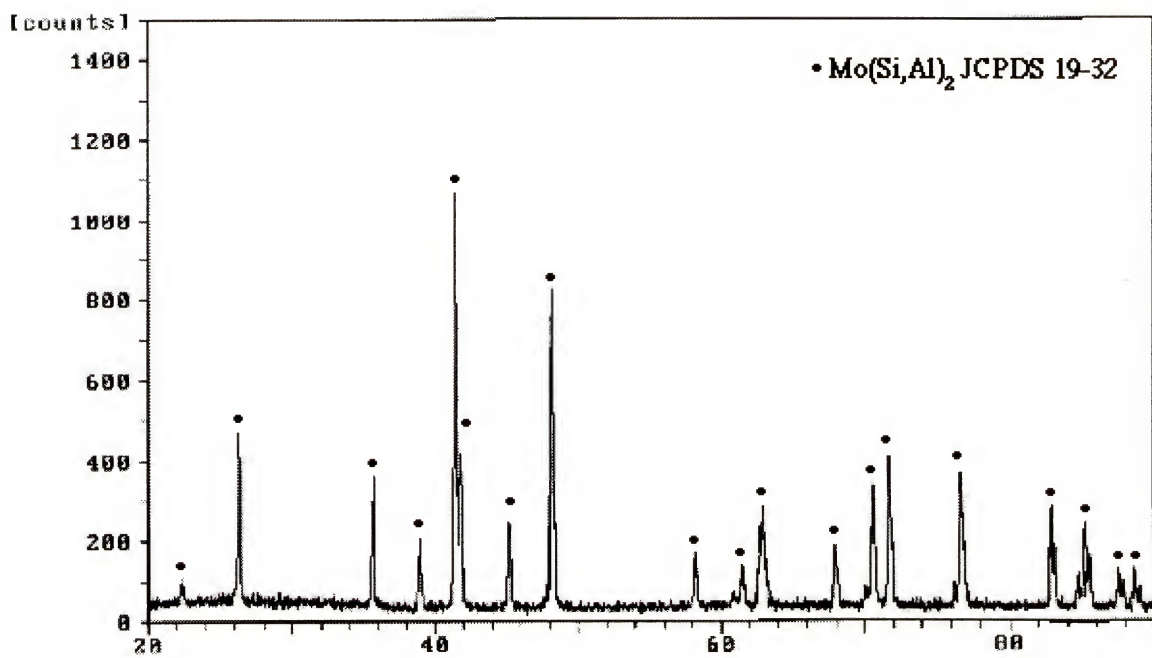
Figure 4.12 Spectrum obtained from XRD of a melt product collected from the base of the pressing die after hot pressing of blended powders of Mo, MoSi$_2$ and Al at 1550°C.
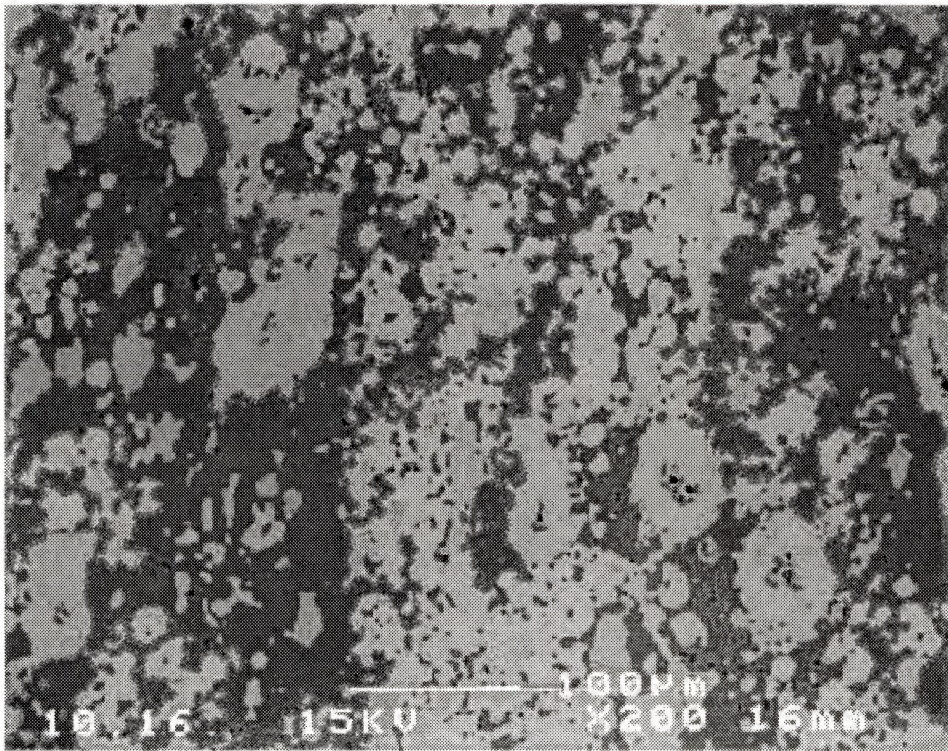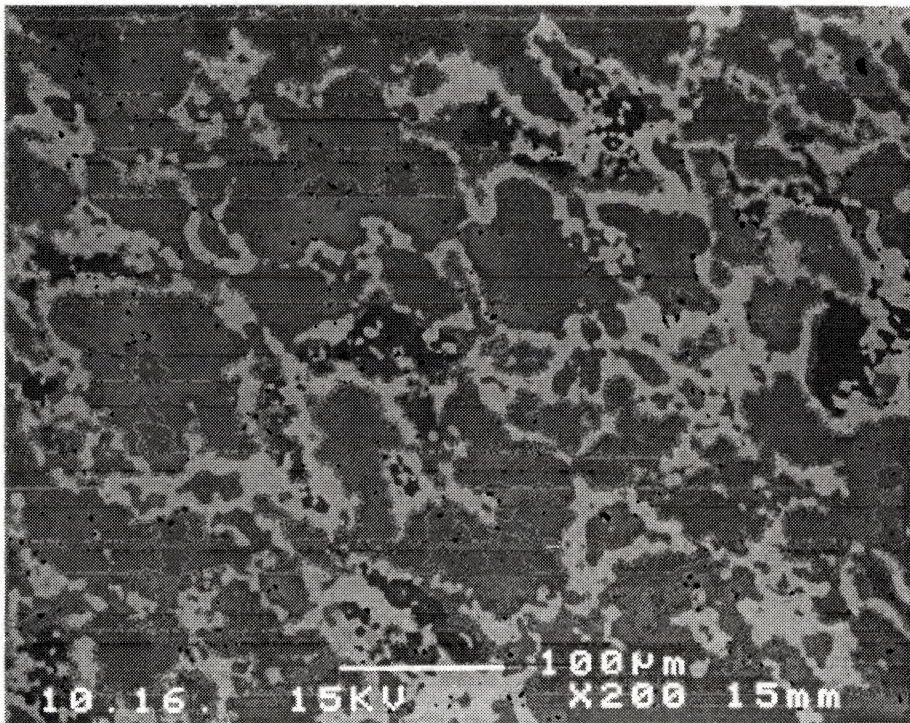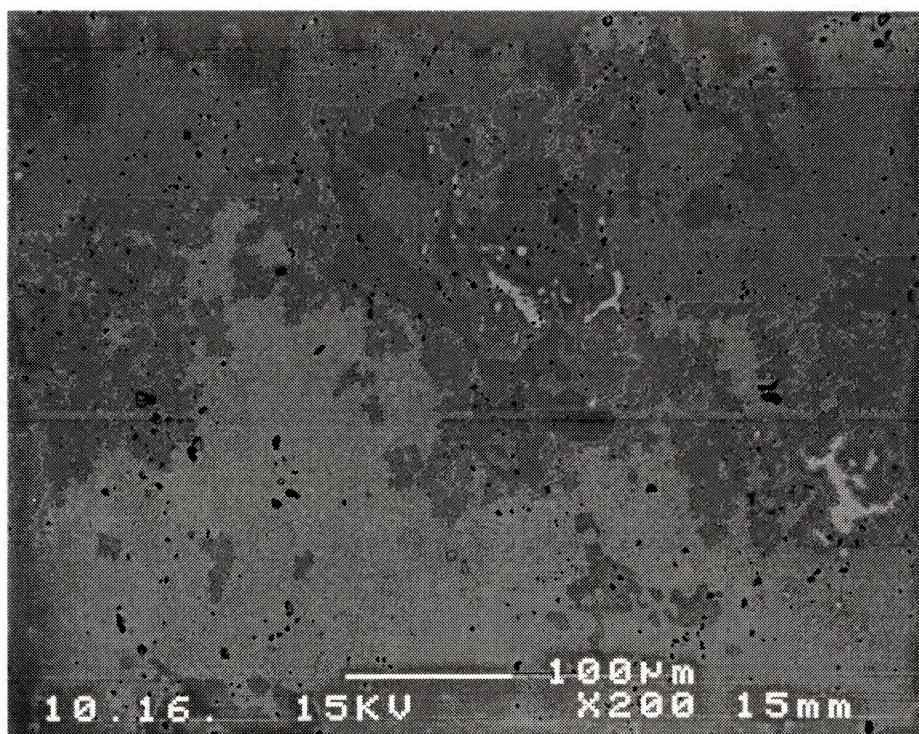
Figure 4.13 Backscattered electron image of the microstructure of alloy 1 after heat treating at 1400°C for 50 hours. The dark-gray phase is Mo_3Al_8 and the light-gray phase is T1. Black regions are alumina and/or porosity.
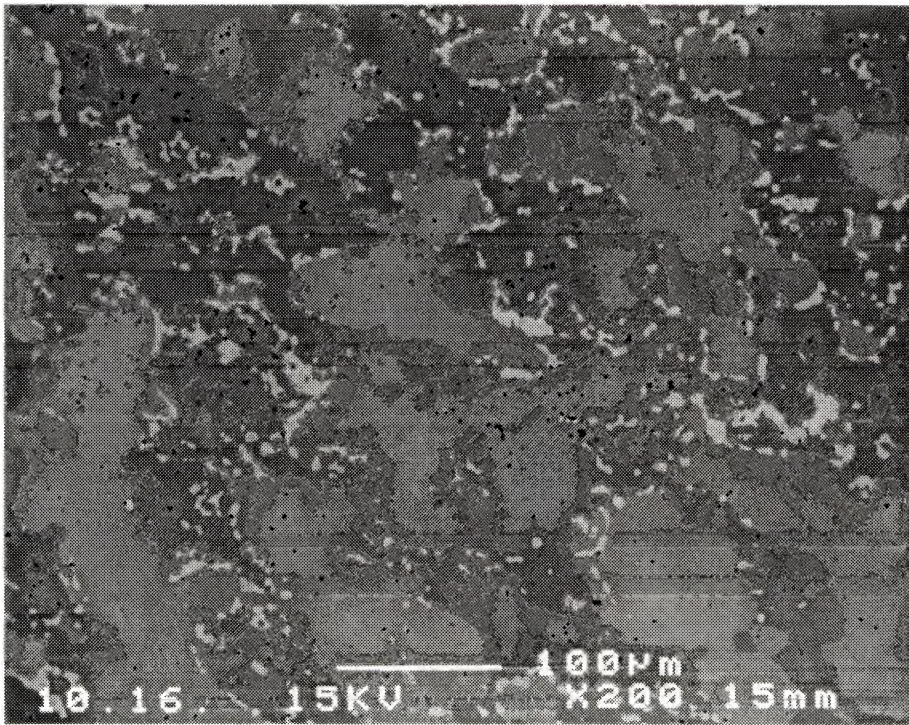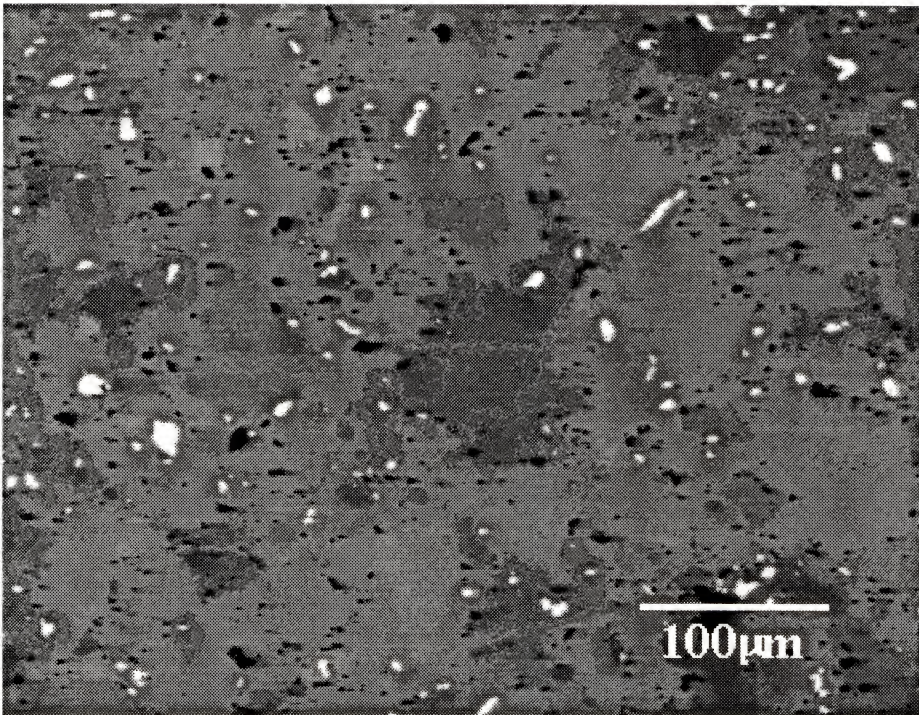
Figure 4.14 Backscattered electron image of the microstructure of alloy 2 after heat treatment at 1400°C for 50 hours. The dark-gray phase is Mo_3Al_8, the medium-gray phase is C54 and the light-gray phase is T1. The black regions are alumina and/or porosity.

Figure 4.15 Backscattered electron image of the microstructure of alloy 3 after heat treatment 1400°C for 50 hours. The dark-gray phase is Mo_3Al_8, the medium-gray phase is C54 and the light-gray phase is T1. The black regions are alumina and/or porosity.

Figure 4.16 Backscattered electron image of the microstructure of alloy 4 after heat treatment at 1400°C for 50 hours. The dark-gray phase is Mo_3Al_8, the medium-gray phase is C54 and the light-gray phase is T1. The black regions are alumina and/or porosity.

Figure 4.17 Backscattered electron image of the microstructure of alloy 7 after heat treatment at 1400°C. This sample was heat treated for only 5 hours. The gray matrix is the C40 phase, the white regions are T1 and the black regions are alumina and/or porosity.

Table 4. Measured equilibrium compositions from the seven alloys chosen for
reassessment of the Mo-Si-Al ternary isotherm.

		At. % Mo	At. % Si	At. % Al
Mo_3Al_8 - T1 Two-phase equilibrium (Alloy 1)				
	Mo_3Al_8	28	1	71
	T1	63	26	11
Mo_3Al_8 - T1- C54 Three-phase equilibrium (Alloys 2,3,4 data averaged)				
	Mo_3Al_8	27	2	71
	T1	61	30	9
	C54	35	23	42
C40 - T1 Two-phase equilibrium (Alloys 5,6,7 shown individually)				
#5	C40	34	39	28
	T1	61	32	6
#6	C40	34	46	20
	T1	62	33	5
#7	C40	33	54	13
	T1	60	35	5

4.2.1 The T1-Mo$_3$Al$_8$ Two-Phase Equilibrium

The current work indicates that at 1400°C T1 is in equilibrium with Mo$_3$Al$_8$ and not with the MoAl compound as shown on the Yanigahara isotherm. In addition, the measured Mo content of the T1 phase in Alloy 1 was ~1.7 % higher than that of T1 in equilibrium with C54 and Mo$_3$Al$_8$, suggesting that this higher-Mo T1 composition forms a terminal boundary for the T1 single-phase field (Figure 4.18). The T1 phase is not expected to display Mo-solubility greatly in excess of that of the binary 5-3 silicide, as observed in other systems where there is little deviation in Mo-solubility between Mo$_5$Si$_3$ and its associated ternary compound. Therefore, it is improbable that the field could extend into the diagram beyond this point.
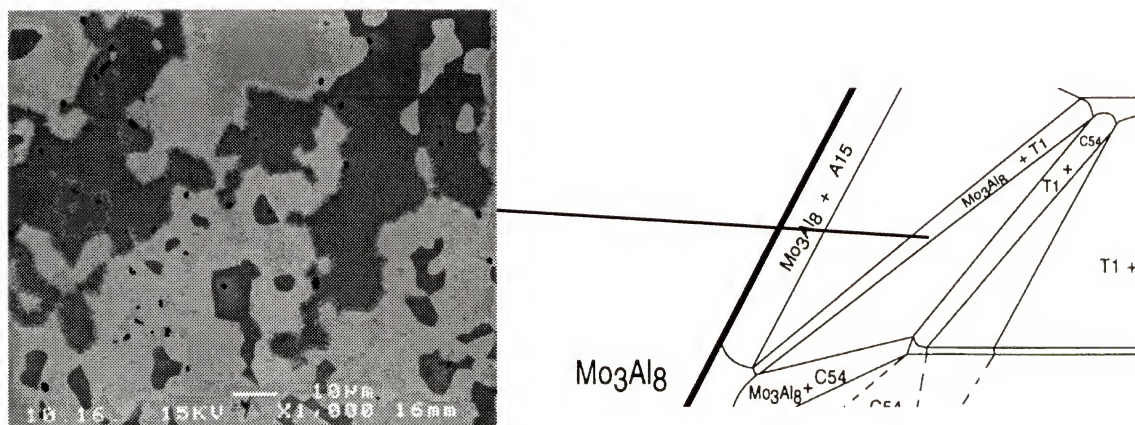
Figure 4.18 Backscattered electron image of Alloy 1 whose composition is indicated on the isotherm. Light, gray and black contrast corresponds to T1, Mo$_3$Al$_8$ and Al$_2$O$_3$ or porosity, respectively.

4.2.2 C54-T1-Mo$_3$Al$_8$ Three-Phase Equilibrium

The presence of the C54 phase, which is absent in the Yanigahara isotherm, is proven by the existence of this three-phase tie triangle. The placement of this field is confirmed by the degree of overlap in the data obtained from Alloys 2, 3, and 4 as well as the agreement of the relative amounts of the three phases with the location of the initial alloy compositions (Figure 4.19). Verification of the C54 crystal structure is shown by XRD (Figure 4.20) It should be noted that verifying the existence of the C54 phase at 1400°C does not directly dispute the Yanigahara isotherm since the phase may not be present at elevated temperatures, although its disappearance is unlikely based on data generated to date on these alloys. Further study is needed to determine the elevated temperature stability of the C54 phase.
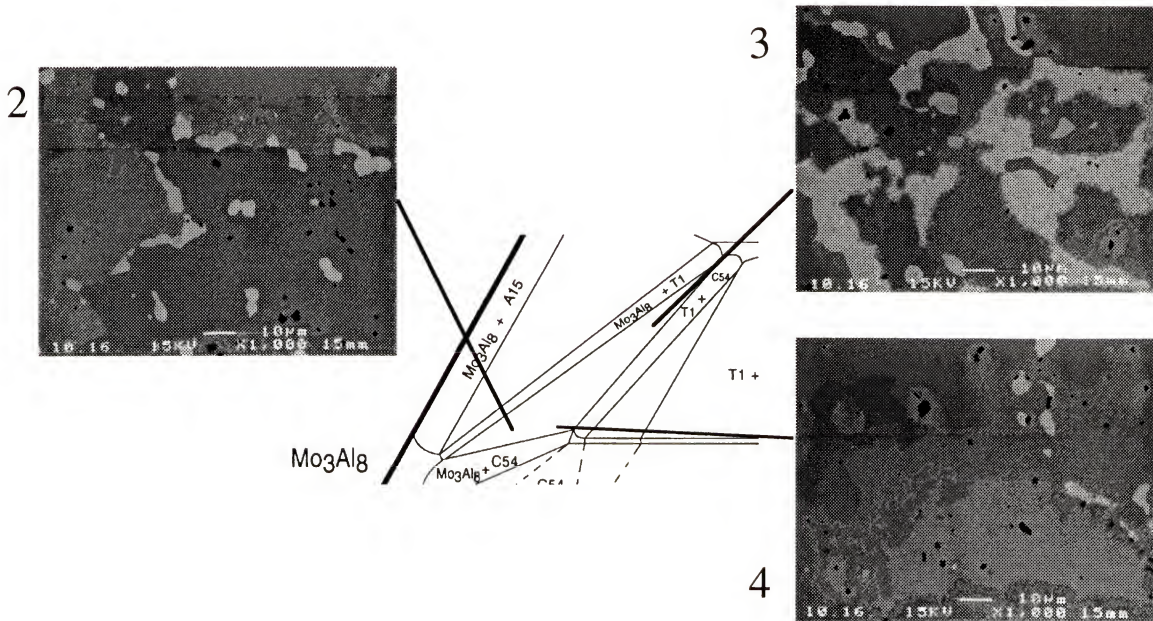
Figure 4.19 Backscattered electron images of Alloys 2, 3, and 4 at compositions indicated on the diagram section. Light, medium and dark gray phases are T1, C54 and Mo$_3$Al$_8$, respectively, while black regions are oxide or porosity.
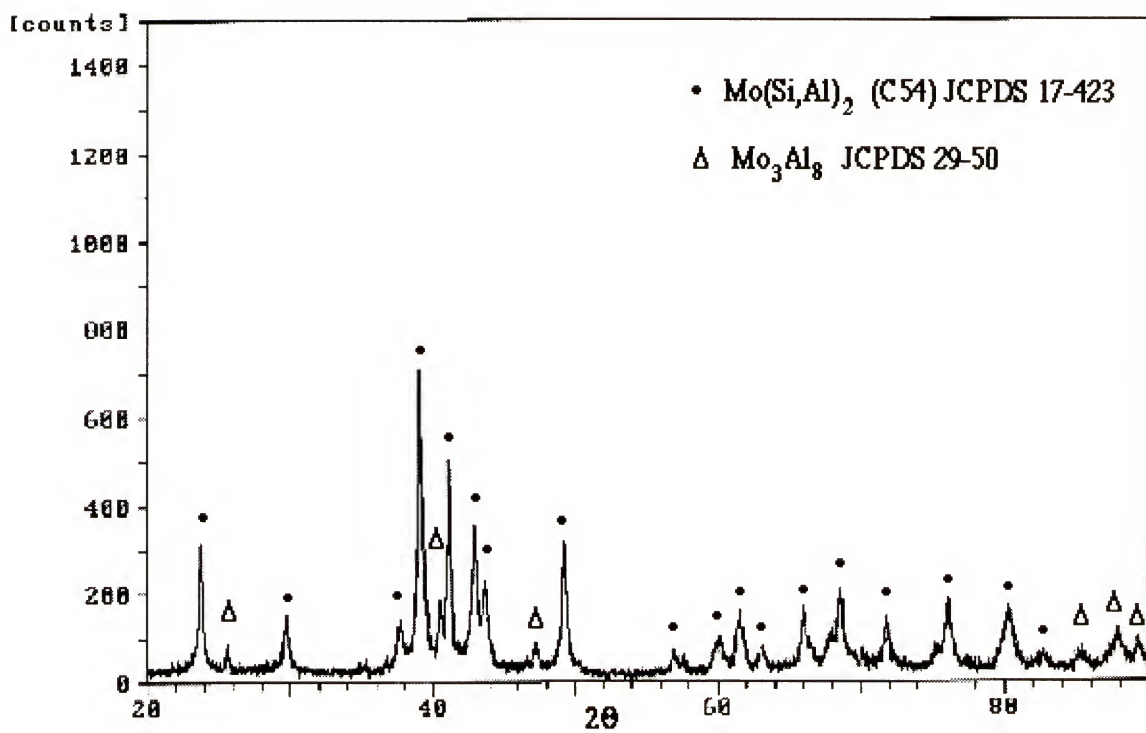
Figure 4.20 Spectrum obtained by XRD from alloy number four. The Spectra for the C54 and Mo_3Al_8 phases are both present. The T1 phase observed in the microstructure is suspected to be absent from this spectrum due to its small volume fraction in the alloy.

4.2.3 T1 - C40 Two-Phase Equilibrium

The Brukl and Yanigahara diagrams differ with respect to the range of T1 compositions in two-phase equilibrium with the C40 phase as well as the homogeneity range of the T1 single-phase field. Data from Alloys 5, 6, and 7 indicate that the T1 and C40 phases are in equilibrium over a wider range of compositions than reported by Brukl. These data also indicate a broader homogeneity range for the T1 phase (Figure 4.21).
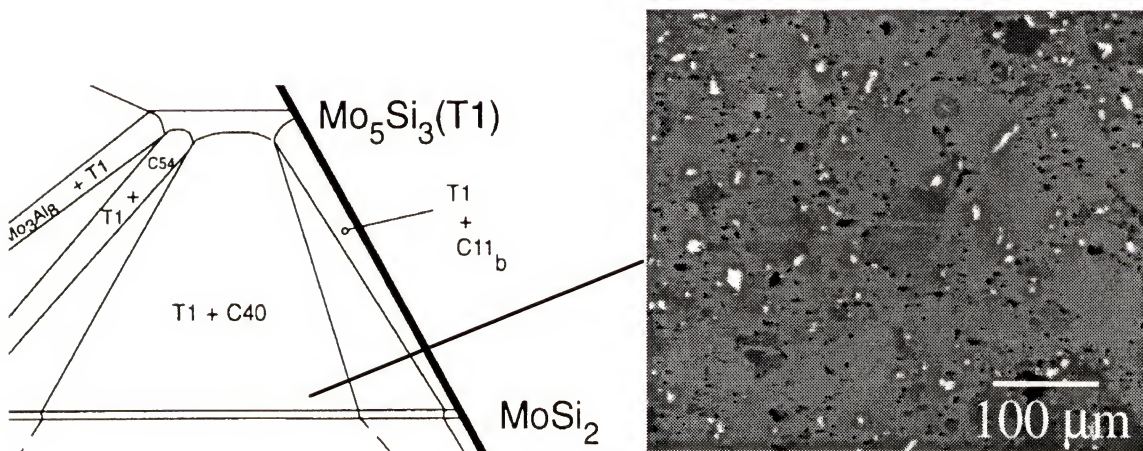
Figure 4.21 Backscattered electron micrograph of Alloy 7 whose composition is indicated on the diagram. Light and dark gray phases are T1 and C40, respectively, while black areas are oxide or porosity.

Based on the placement of the phase fields determined in this study, an isothermal phase diagram was produced for the Mo-Si-Al ternary system at 1400°C (Figure 4.22). This diagram should provide a more accurate guide for the production of Mo-Si-Al ternary alloys. It should be noted that all phase boundaries on this diagram were not assessed experimentally; they merely connect the experimentally-determined data in the most logical manner based on the Gibbs phase rule and knowledge about the other phase fields.
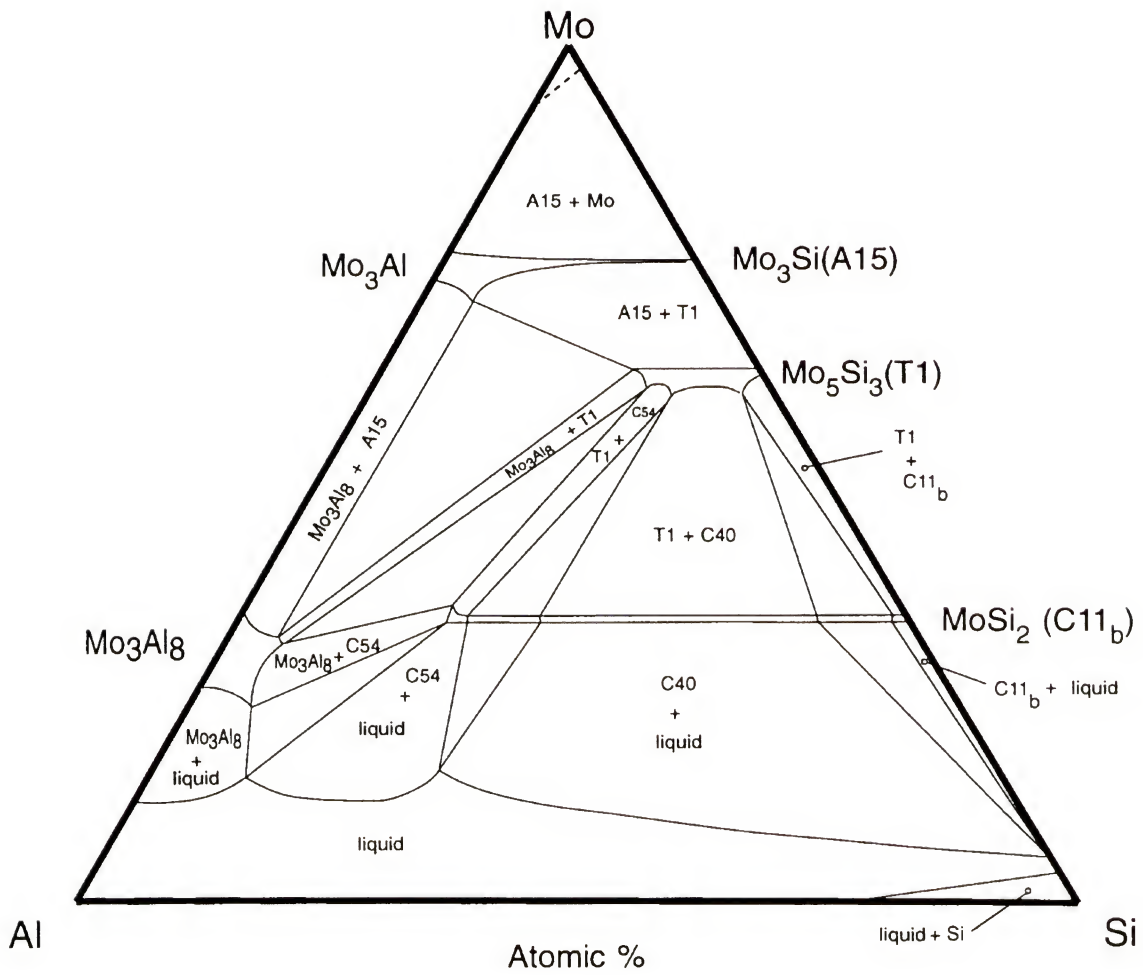
Figure 4.22 Proposed Mo-Si-Al isotherm at 1400°C.

4.3 Environmental Degradation Phenomenon

As mentioned in Chapter 2, much of what is known of the room temperature environmental behavior associated with the $Mo(Si, Al)_2$ C40 phase has been discovered through the course of this investigation. The phenomena discussed previously will be addressed as experimental results leading to the investigation of the anomalous room temperature degradation and grain boundary attack that has been observed. Much of the experimentation was guided by each new observation. Accordingly, the results will be presented (as possible) in the chronological order in which the study was performed.

4.3.1 Room Temperature Behavior

The first observation of room temperature attack occurred when samples produced by various processing techniques were being compared for the process optimization investigation. It was noted that samples produced 17 months prior had undergone attack at the grain boundaries and specifically at the triple points. There appeared to be either a loss of entire grains or the growth of pores to the scale of the matrix grain structure (Figure 4.23). Investigation of the attack in the SEM revealed the boundaries and, more often, triple-points had been attacked, leaving behind no discernible reaction product (Figure 4.24). It was evident that an extensive attack of the grain boundaries was occurring under ambient conditions. Despite the discovery of this effect, the initial investigation continued with an emphasis on the evaluation of room temperature mechanical properties under the assumption that the kinetics involved in the attack were sufficiently slow, and that reliable mechanical property information could be obtained prior to any significant degradation. Attempts at evaluating microhardness were met with inconclusive results due to excessive grain boundary decohesion surrounding the Vickers indents (Figure 4.25). Deformation from the cracking invalidated the microhardness test, and it was decided that further evaluation of mechanical properties should be reserved until the grain boundary deficiencies of the C40 sample could be assessed.
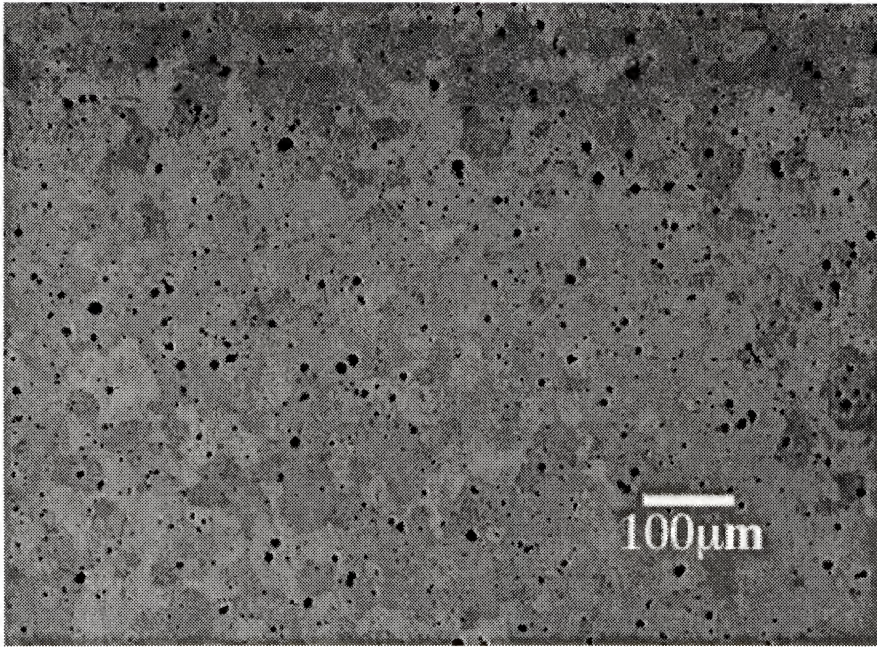
(a)
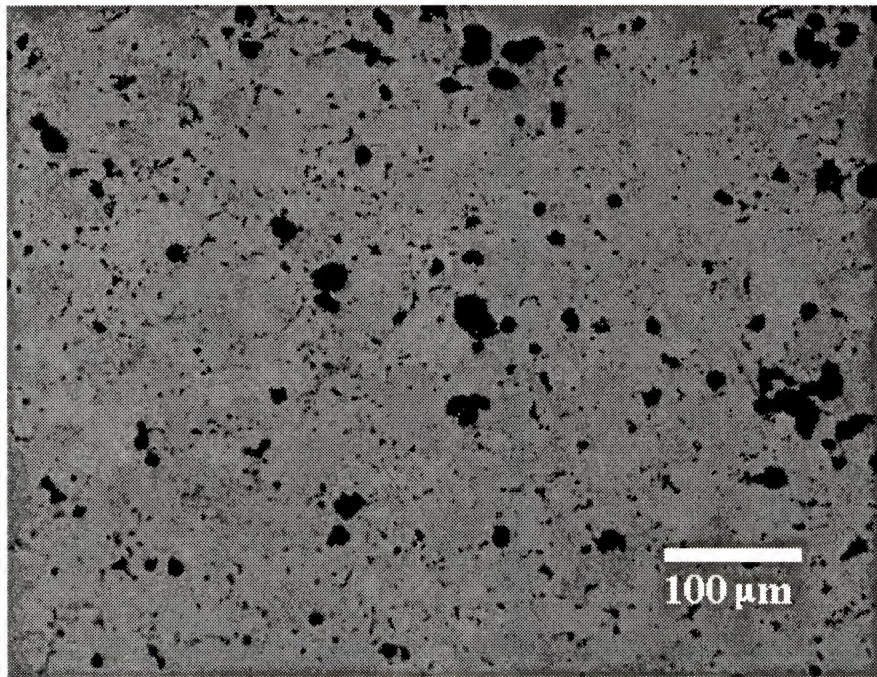
(b)

Figure 4.23 Optical micrographs of C40-Mo(Si,Al)$_2$ samples produced by the blended powder technique. a) Microstructure of a sample immediately after production. Black regions are alumina and/or pores. b)   Microstructure of a sample after 17 months in air at room temperature. Black regions are either sites of attack or preexisting alumina and pores.
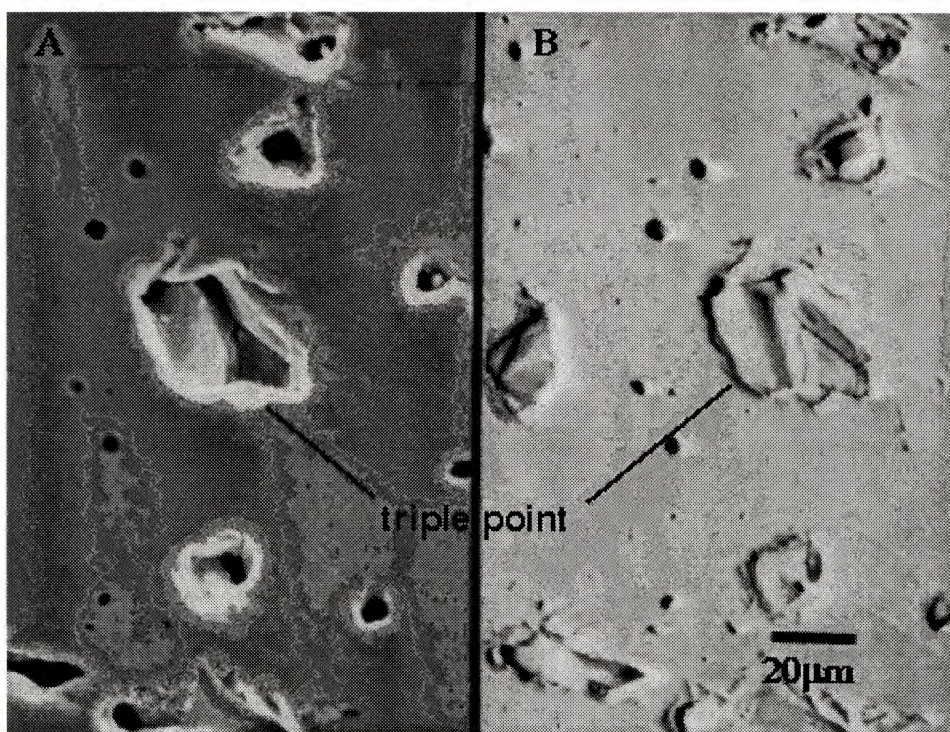
Figure 4.24 Scanning electron micrograph of a grain boundary triple point of a C40-
Mo(Si,Al)$_2$ sample after 17 months in air at room temperature. A) Secondary
electron image. Black regions denote alumina and/or pores. Light outlines on
pores are due to edge charging effects. B) Backscattered electron image of same
region.
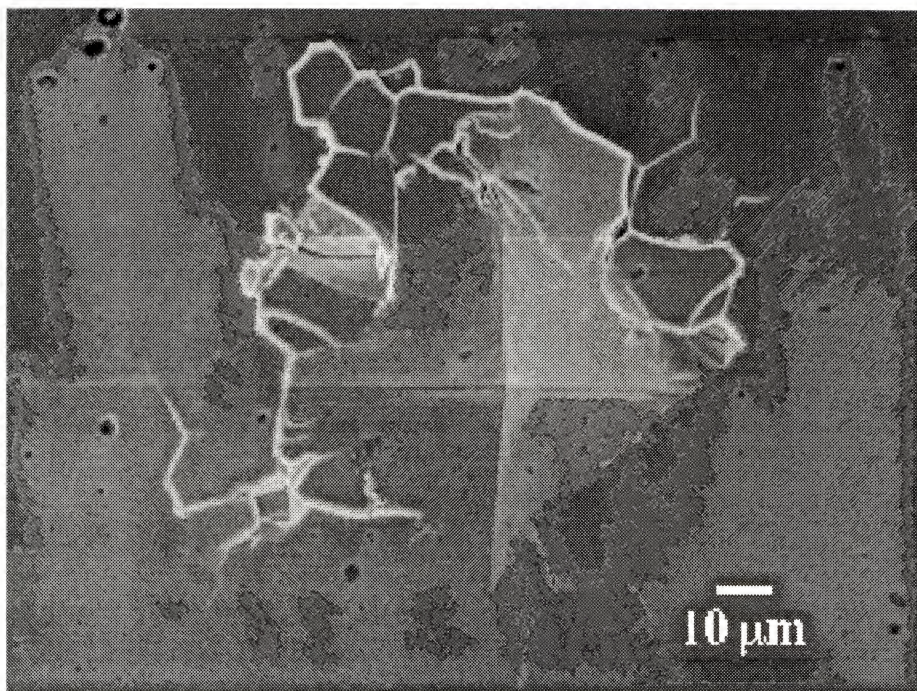
Figure 4.25 Secondary electron image of a Vickers microhardness indent in C40-Mo(Si,Al)$_2$. Note the grain boundary decohesion surrounding the indent.

4.3.2 Elevated Temperature Behavior

In order to enhance the reaction kinetics, samples were heat treated in a moist air environment at 200°C in attempts to expedite the process which occurred in 17 months at room temperature. The samples were removed from the furnace after 20, 40, 80 and 160 hours and inspected by SEM for signs of grain boundary attack. Scanning electron microscopy of the exposed surfaces showed little sign of attack up to 80 hours (Figures 4.26-4.28). Between 80 and 160 hours there was a noticeable change in surface quality as a result of grain boundary attack. The affected surface is marked by grooving along boundaries as well as what appears to be the lifting out of grain corners at boundary triple points (Figure 4.29). Inspection of the grain boundary surfaces exposed by the disappearance of grain corners revealed a dimpled surface, with the dimple features arranged in an evenly spaced, periodic manner. Secondary electron imaging of the dimples was difficult due to the lack of topography (the source of most contrast in secondary electron imaging) coupled with the fact that the features were not discernible at high magnification. The dimples became difficult to image when the electron beam diameter was reduced at high magnification. When the electron beam was widened, the dimples appeared with moderate clarity, but the size of the beam did not allow for good resolution of the image. Suspecting that the increased current was increasing the backscattered component of the secondary electron imaging, backscattered electron imaging was used to study the dimples (Figure 4.30). The backscattered images show the dimples with more contrast than in the secondary images. This suggests a chemical segregation in the dimpled regions, and that these regions have a lower average atomic number than the matrix. Otherwise, the backscattered images do not indicate any significant chemical variation on the surfaces of the grains. Energy dispersive X-ray spectroscopy (EDS) was used to compare the compositions of the dimple surfaces to the composition of the matrix (Figure 4.31). The resulting EDS spectra indicate that the "dimples" are rich in silicon relative to

the matrix. Unfortunately the fine scale of the segregation would not permit a quantitative analysis of the chemistry of the dimples.

When attempts were made to section the samples after exposure for 160 hours, the low speed diamond saw cut through the material at an accelerated rate. Attempts to polish the surface for metallographic inspection were frustrated by grain pullout which prevented production of an adequate surface condition for microscopy. It appeared the boundaries were weakened severely by the elevated temperature exposures.
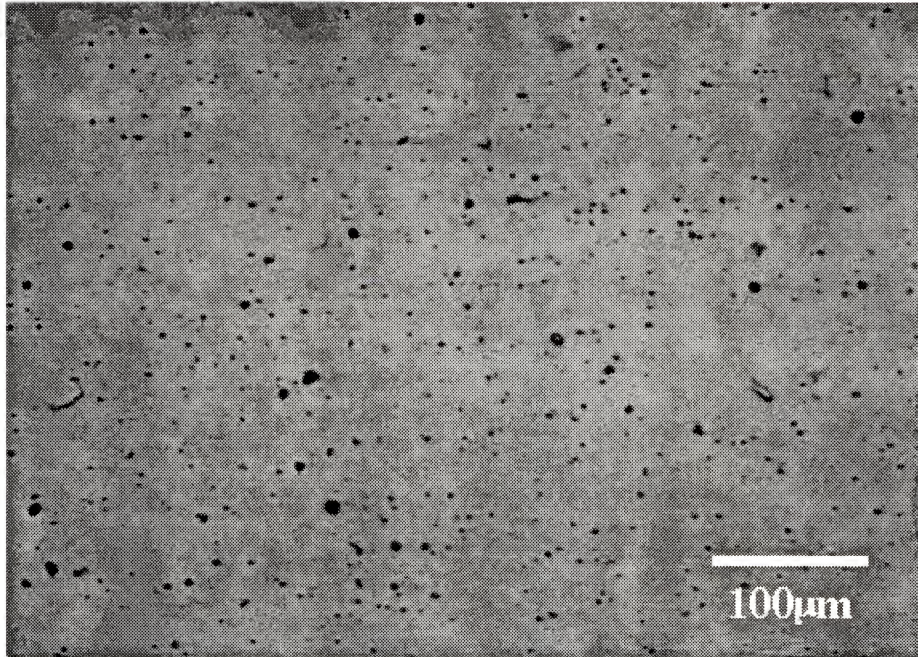
Figure 4.26 Backscattered electron image of a polished C40-Mo(Si,Al)$_2$ sample heated at 200°C in air for 20 hours. Surface shows no evidence of atmospheric attack along boundaries.
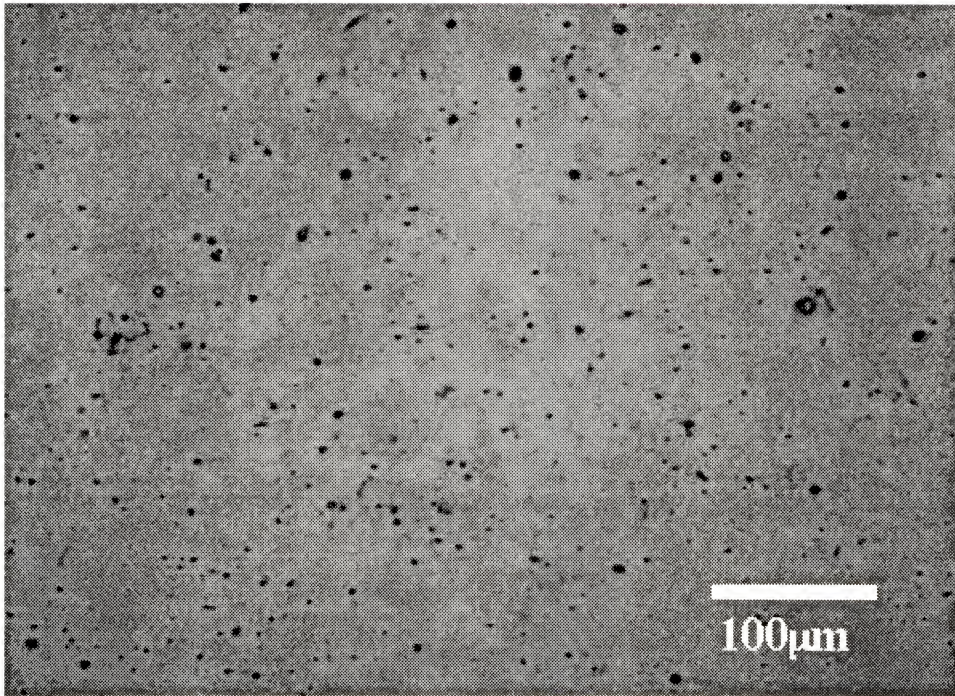
Figure 4.27 Backscattered electron image of a polished C40-Mo(Si,Al)$_2$ sample heated at 200°C in air for 40 hours. Surface shows no evidence of atmospheric attack along boundaries.
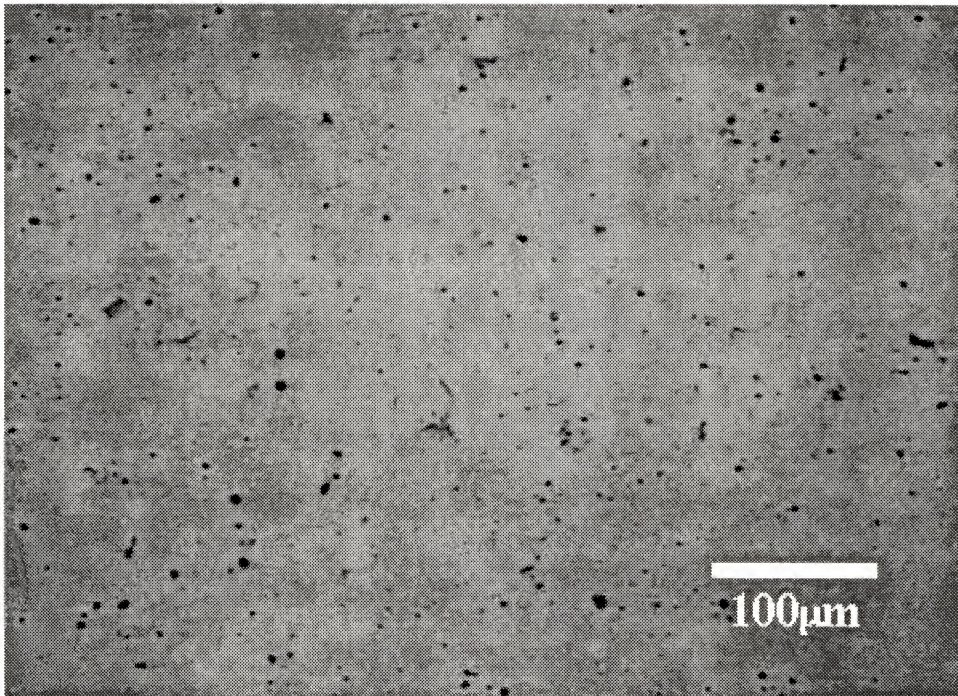
Figure 4.28 Backscattered electron image of a polished C40-Mo(Si,Al)$_2$ sample heated at 200°C in air for 80 hours. Surface shows no evidence of atmospheric attack along boundaries.
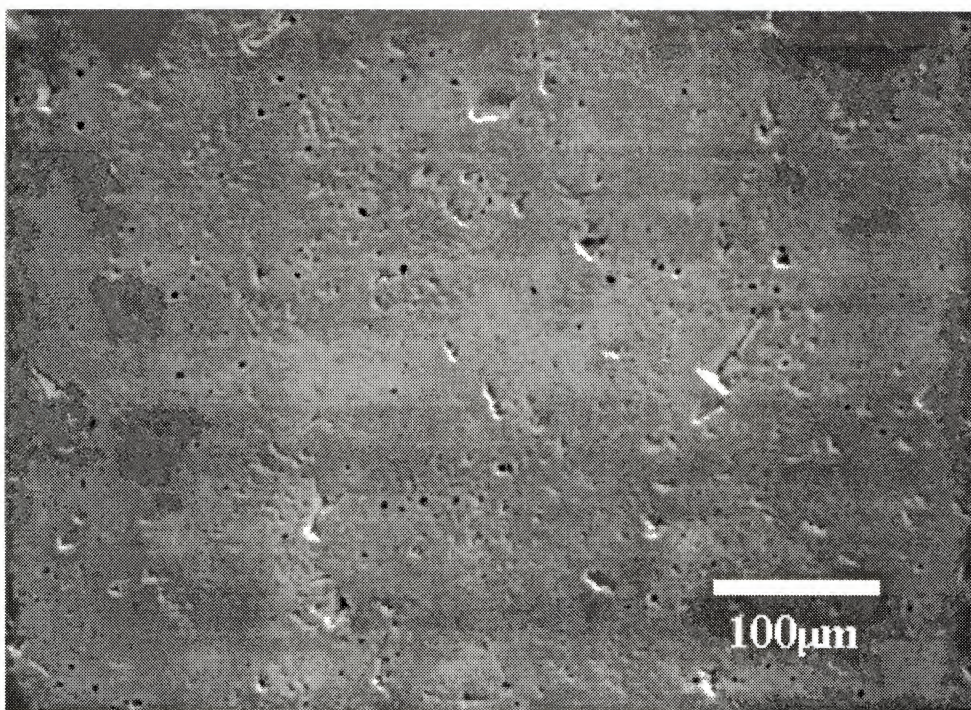
(a)
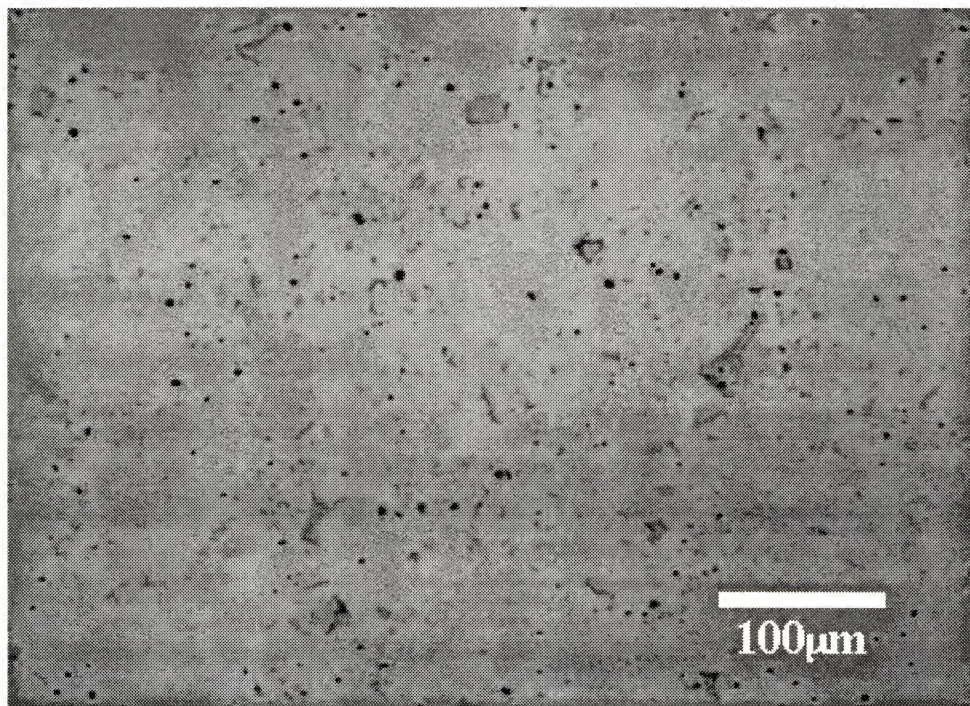
(b)

Figure 4.29 Electron micrographs of a polished C40-Mo(Si,Al)$_2$ sample heated at 200°C in air for 160 hours. a) Secondary electron image shows boundary grooving and loss of material a boundary triple points. b) Backscattered electron image shows no chemical segregation due to boundary attack at this magnification.

(a)
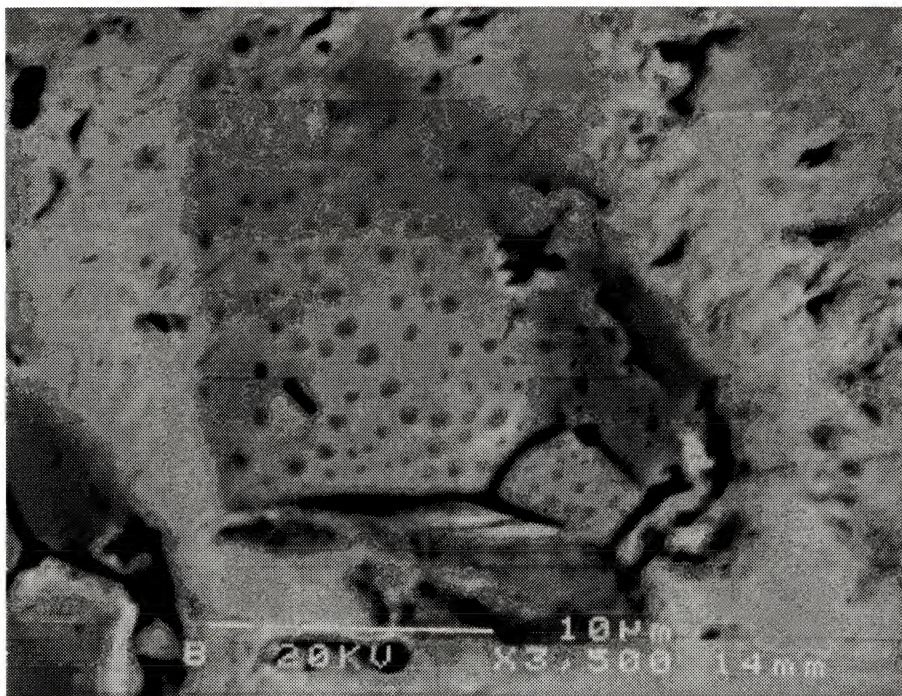
(b)

Figure 4.30 Electron micrographs of C40-Mo(Si,Al)$_2$ grain boundary triple point with grain corner removed. Surface of grain boundary marked with periodic array of dimples. a) Secondary electron image showing little contrast of dimple regions. Bright region due to charging due to wide electron beam   b) Backscattered electron image showing higher contrast of dimple regions.

University of Florida / MAIC
Cursor: 0.000keV = 0

Dimple Interior	Matrix

Si

Si

Mo

Mo

Al

Al

0.000   2:EXEC(7-D) DATA LABEL   VFS = 1024   10.240
20   1:EXEC(7-D) DATA LABEL   20
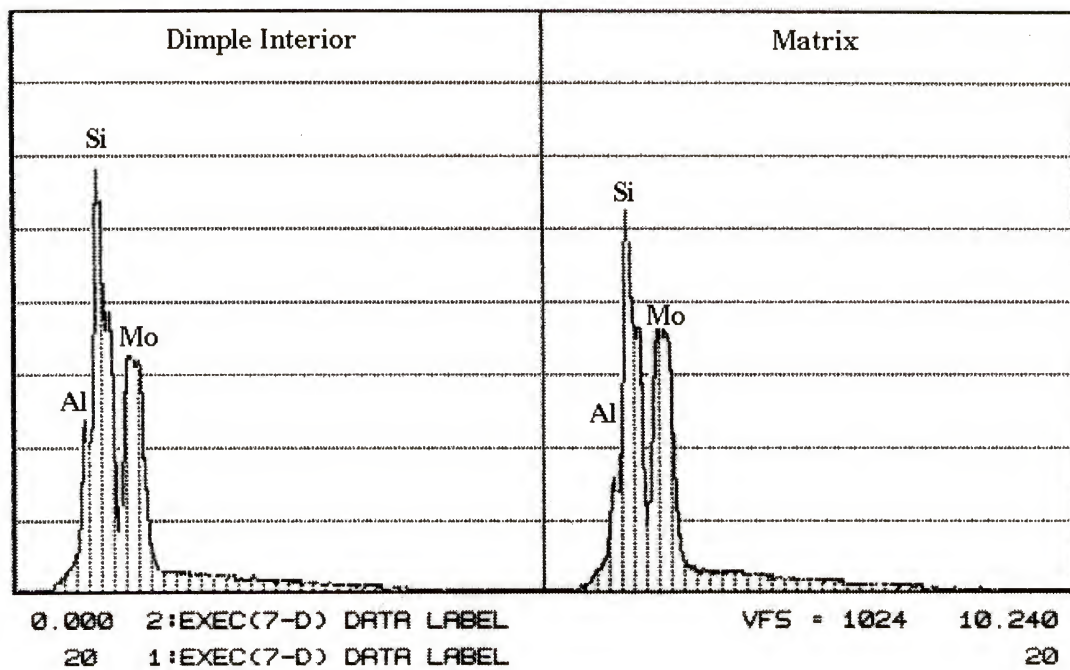
Figure 4.31 Spectra obtained by EDS from both a dimpled region and the adjacent matrix on an exposed grain facet of C40-Mo(Si,Al)$_2$. Relative peak heights of silicon to the other atomic species indicate an enrichment of silicon in the dimpled region.

4.3.3 Grain Boundary Investigation

Since the atmospheric attack was noted at grain boundaries and triple points, samples were fractured to expose grain boundary surfaces, then examined in the SEM (Figure 4.32). The surfaces exposed by the fracture were intergranular fracture, and allowed the investigation of grain boundary surfaces and triple points. It was noted that some of the boundaries displayed a contrast effect that could not be attributed to edge enhanced secondary electron emission. The morphology and scale of these bright regions made them too fine for good resolution by scanning electron microscopy. The EDS obtained from the charged regions indicated the presence of a small quantity of carbon (Figure 4.33). This evidence of carbon in the boundaries could not be taken as conclusive since fracture of the sample was performed in the ambient atmosphere, and exposure of the boundary to contamination was unavoidable. The data from the SEM investigation could not be used to quantify the extent of the carbon contamination because molybdenum, aluminum and silicon all have high absorbence of carbon signal in the EDS. Thus, it was decided that AES might provide a more accurate account of the role of carbon in the boundaries. Due to the high vacuum (typically 10^{-10} Torr), examination of surfaces fractured in the Auger chamber allowed inspection of the grain boundary surfaces without exposure to any atmospheric species. Again the fracture surfaces were perfectly intergranular and the spectrum obtained from these grain boundary surfaces indicated the presence of the expected atomic species (Mo, Al, Si, O) as well as the presence of carbon (Figure 4.34).

To ascertain the extent of the carbon impurity and segregation, AES depth profiles were generated and it was clear that the carbon observed in the initial spectrum drops off almost instantaneously as does oxygen (Figure 4.35). More surprising was the slight
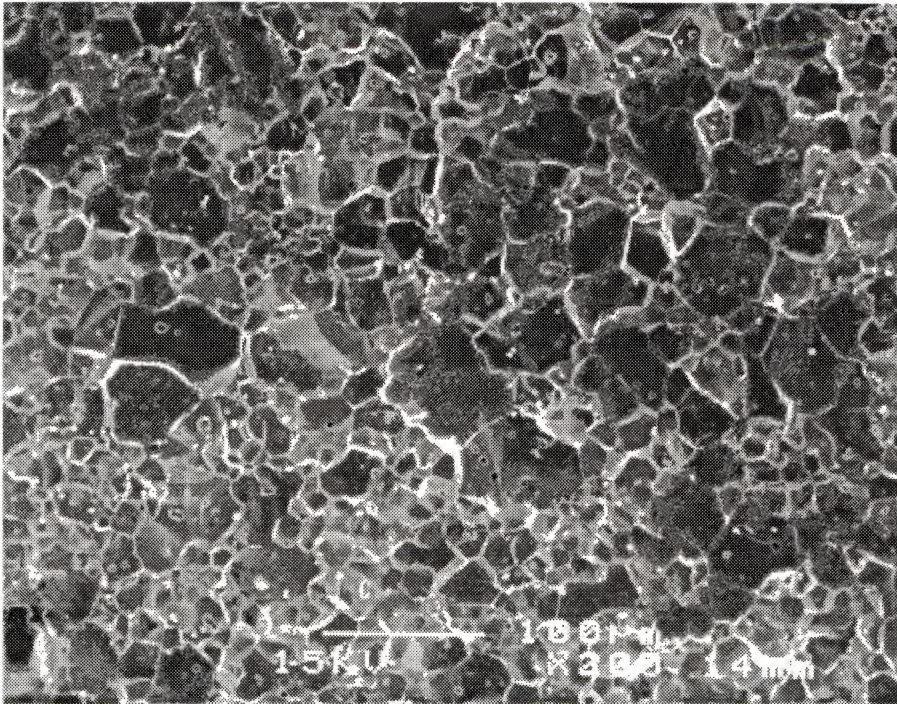
(a)
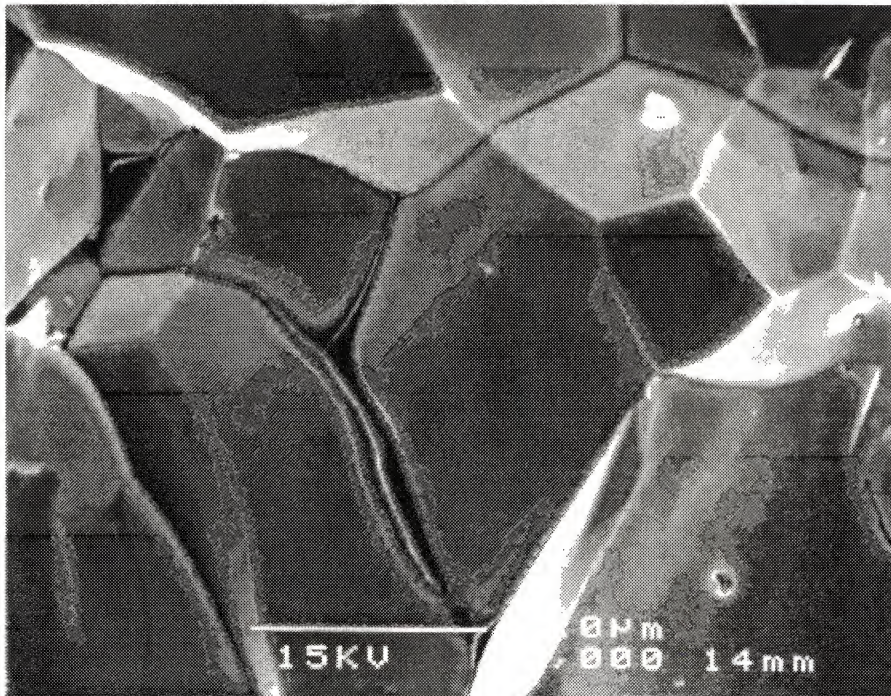
(b)

Figure 4.32 Secondary electron images of fracture surfaces of C40-Mo(Si,Al)$_2$. a) Image shows perfectly intergranular fracture surface. b) High magnification image shows contrast along grain boundary triple points.
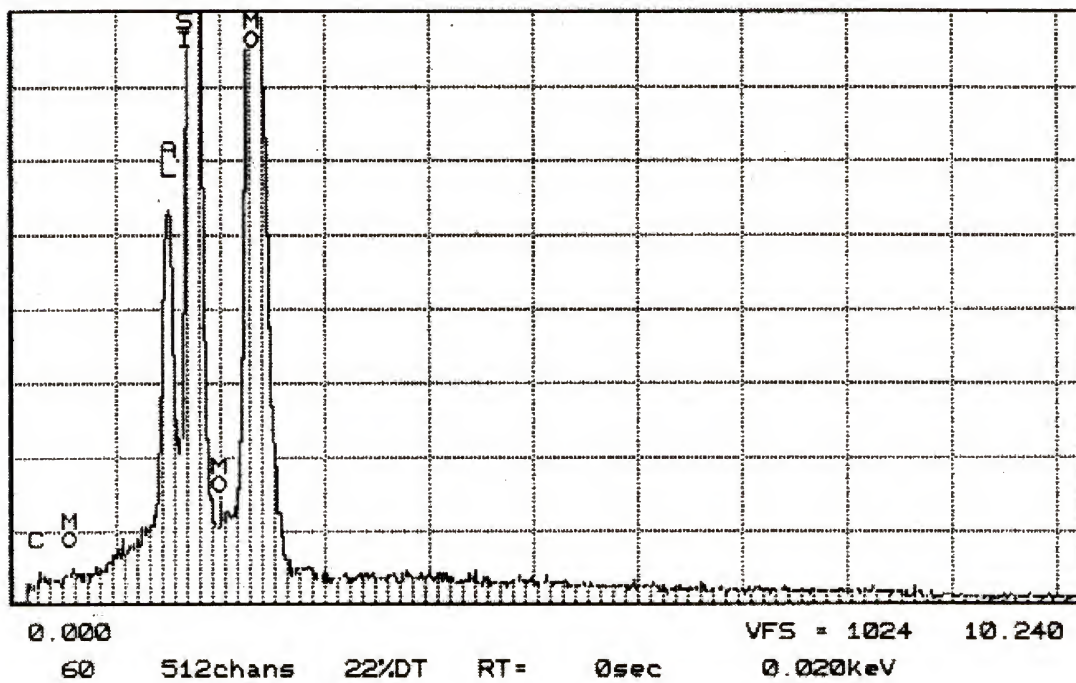
Figure 4.33 EDS spectrum from the ccontrasting regions of the C40-Mo(Si,Al)$_2$ grain boundary. Note the small carbon peak despite high carbon emission absorption by other atomic species.

enrichment of aluminum and silicon at the boundaries, and the associated depletion of molybdenum

The general nature of data from the AES begs the mention of some caveats to interpreting the apparent phenomena. First, the sputter rate of C40 is not known, therefore it is difficult to say what the true depth of this compositional variation is. Second, it should be noted that the spectrum is taken from an entire grain facet which may have local regions of chemical segregation which could exaggerate the appearance of overall bulk segregation. Third, the apparent drastic change in molybdenum concentration may be an artifact of a change in the bonding state of molybdenum near the boundaries. Despite these complicating issues, the AES is clear in showing the presence of elemental species at the boundary and the evidence of carbon contamination is taken as reliable data.

Fracture surfaces were exposed to moist air at 200°C to observe the behavior of the boundary surface. The resulting surface displayed regions of boundary recession around alumina particles as well as recession of some of the boundary triple points (Figure 4.36). The investigation by SEM also revealed an altered state of the regions which displayed charge prior to atmospheric exposure (Figure 4.37). The regions were characterized by a loss of material along the boundaries in a segmented fashion. Within each segment of receded boundary appeared an acicular particle concentric to the shape of the formed cavity. Analysis of the particles by EDS suggests that they are alumina (Figure 4.38). The acicular alumina particles found in these cavities do not possess the same globular morphology as alumina formed from the initial reduction of silica in processing, and are therefore assumed to have formed as a result of the atmospheric attack. The particles in the boundaries showed no sign of carbon, nor did the surrounding cavity, suggesting that carbon evolution is a mechanism involved in the attack.
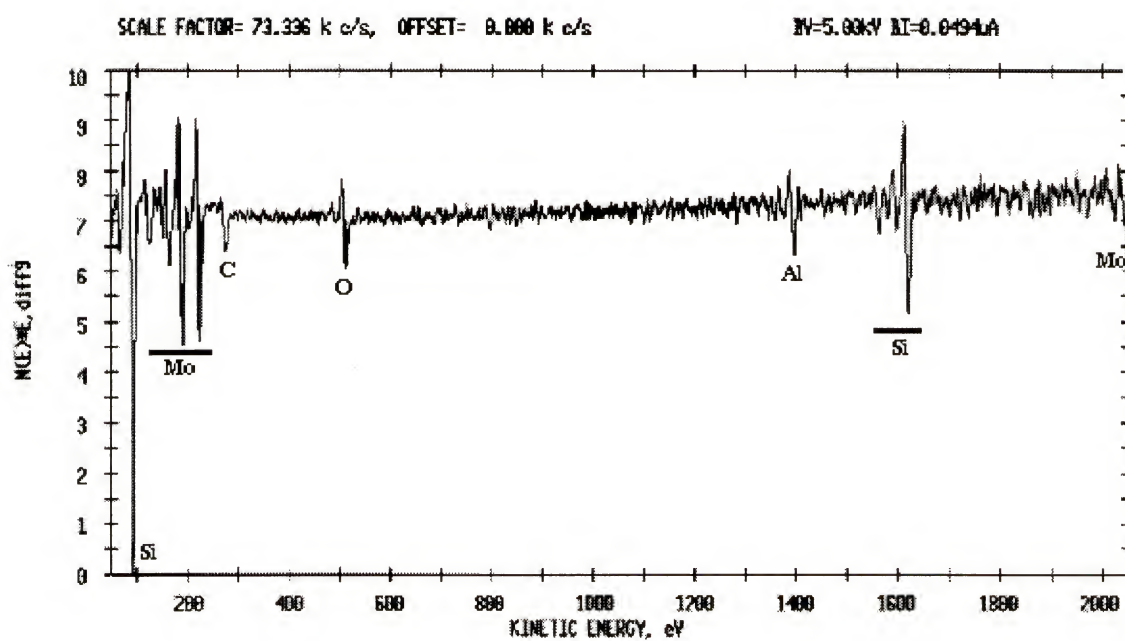
Figure 4.34 Spectrum obtained by AES from fracture surface of C40 Mo(Si,Al)$_2$.
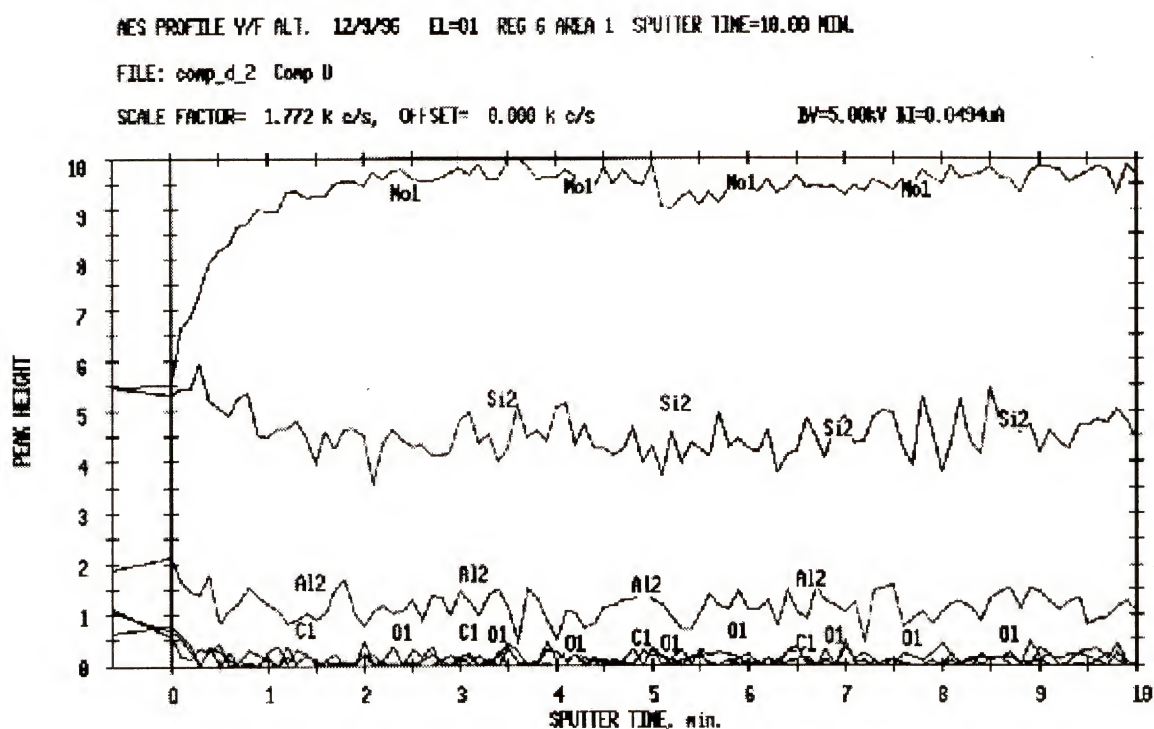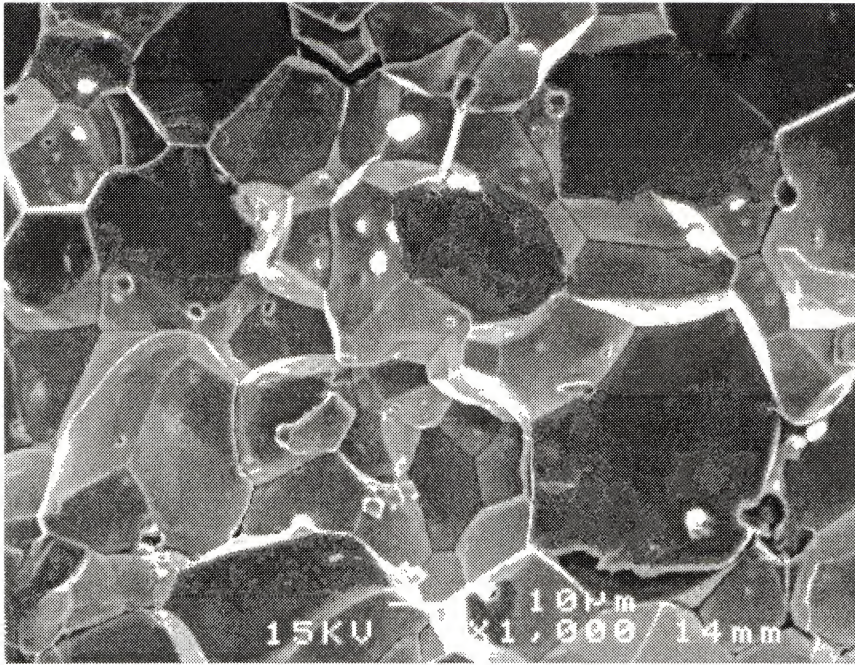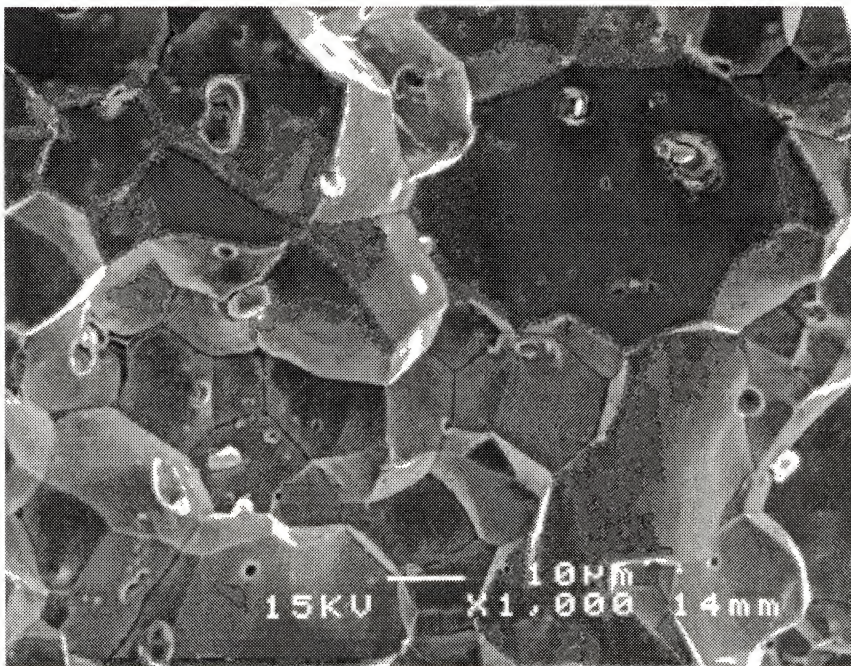Fracture was perfromed in the high vacuum chamber of the AES.

AES PROFILE Y/F ALT. 12/9/96 EL=01 REG 6 AREA 1 SPUTTER TIME=10.00 MIN.

FILE: comp_d_2 Comp D

SCALE FACTOR= 1.772 k c/s, OFFSET= 0.000 k c/s   BV=5.00kV II=0.0494uA

Figure 4.35 Chemical depth profile obtained by AES of the C40-Mo(Si,Al)$_2$ fracture surface. Sputter time represents depth into the grain.

(a)

(b)

Figure 4.36 Scanning electron micrographs of fracture surfaces of C40-Mo(Si,Al)$_2$. a) Secondary electron image of sample surface before exposure to air at 200°C for 160 hours. Small bright spots are alumina b) Secondary electron image of sample surface after atmospheric exposure. Note the recession of material around alumina particles and along some boundaries.
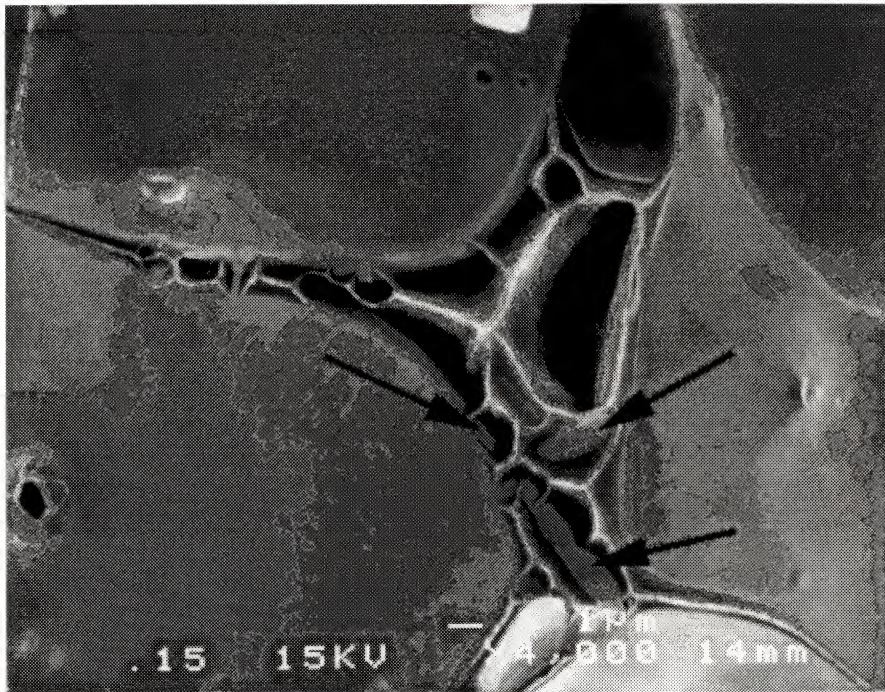
Figure 4.37 Secondary electron image of segmented recession of a C40-Mo(Si,Al)$_2$ grain boundary due to atmospheric exposure for 160 hours at 200°C. Arrows point to apparent alumina particles inside segmented regions.

TN-5 00   TLE 30-JUN-98 08:41
Cursor: 0 000keV = 0

0.000   VFS = 8192   10.240
  6U   512chans   36/DT   RT=   0sec   0.020keV
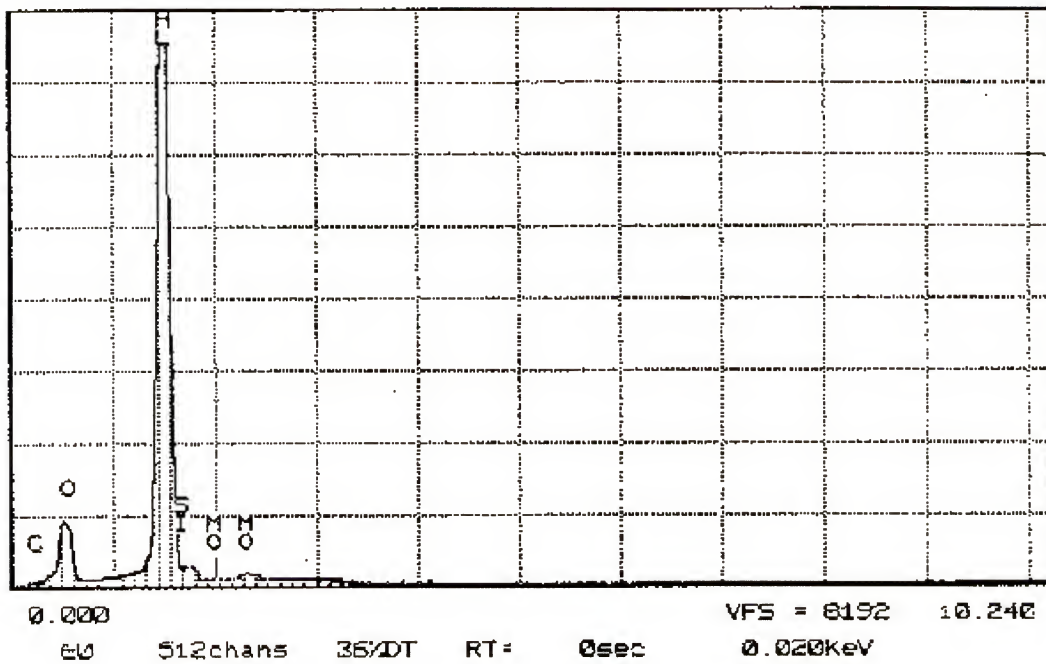
Figure 4.38 Spectrum obtained by EDS of acicular particles found in the receded segments of C40-Mo(Si,Al)$_2$ grain boundaries after exposure to air at 200°C for 160 hours.

Transmission electron microscopy was performed to examine the nature of the grain boundaries in the pre-exposed C40 samples. The samples were found to contain the relatively equiaxed alumina particles as expected from the reduction of silica during processing (Figure 4.39). The boundaries also contained lens-shaped particles consisting of two phases which were identified to be aluminum and silicon carbide (Figure 4.40). The lens-shaped particles were not resident on all boundaries, but were commonly found in groups along some boundaries (Figure 4.41). The necklace arrangement of the particles was similar in scale and spacing to the dimpled regions seen on the surface of samples heated in air at 200°C for 160 hours. These particles were not observed in the samples that had been exposed to attack, suggesting that the disappearance of the coupled particles could be the source of the dimpled cavities remnant of atmospheric attack.

(a)   (b)
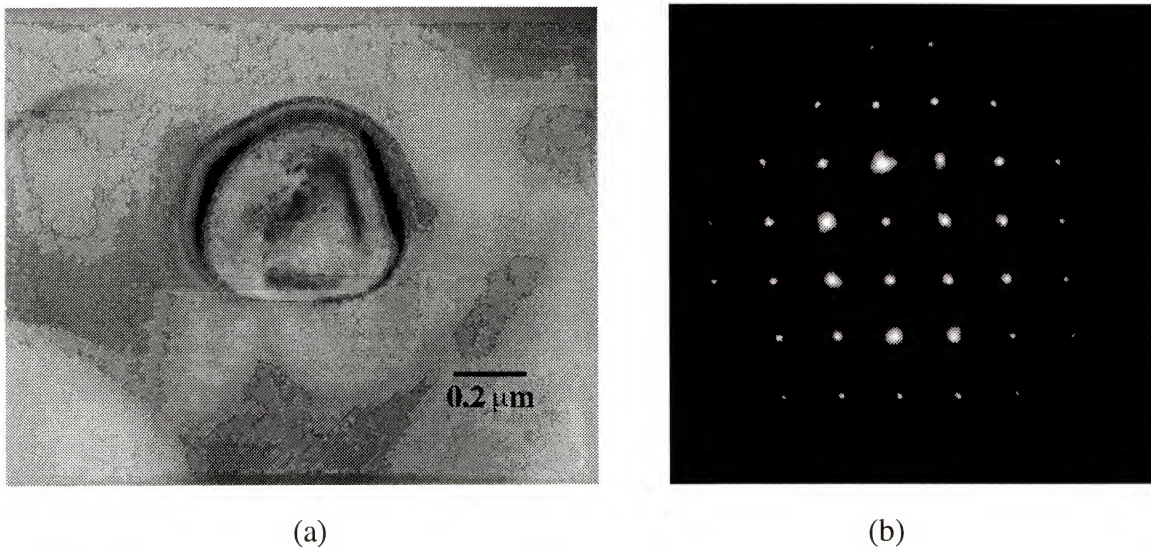
Figure 4.39 Transmission electron microscopy of an aluminum oxide particle found in the C40-Mo(Si,Al)$_2$ alloy. a) BF micrograph of the alumina particle. b) SADP of alumina particle with $\mathbf{B} = [0\ 2\ \bar{2}\ 1]$.
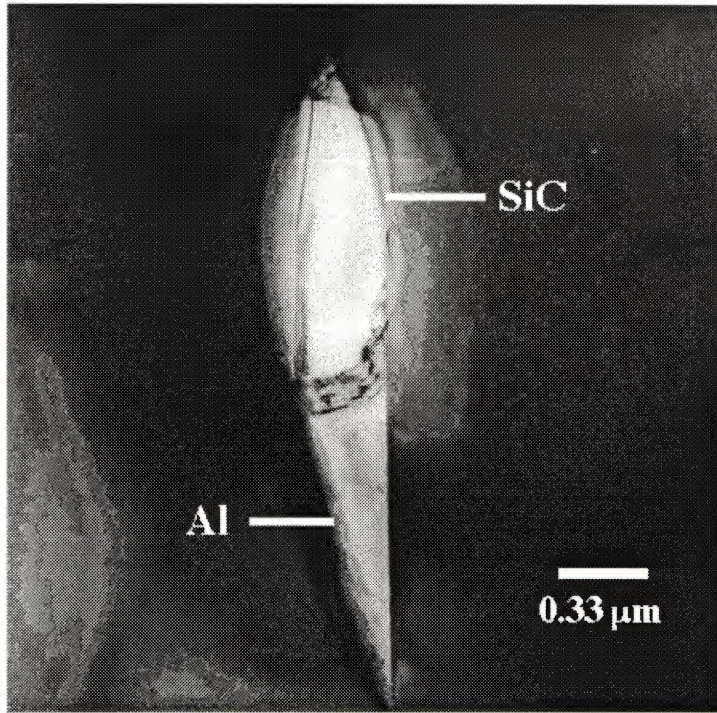
(a)
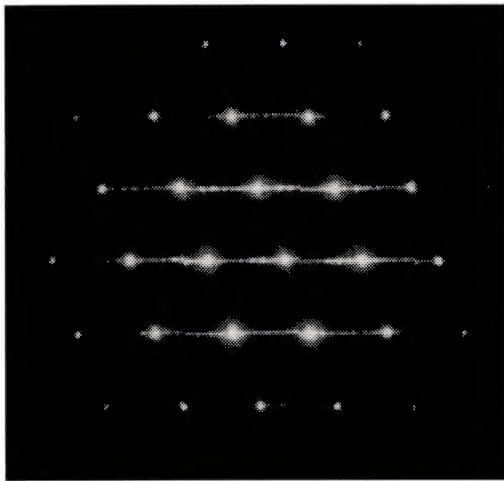
(b)
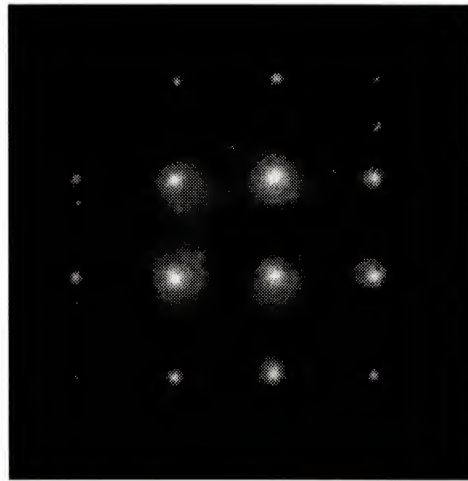
(c)

Figure 4.40 Transmission electron microscopy of an aluminum / silicon carbide coupled particle found along a C40-Mo(Si,Al)$_2$ grain boundary. a) BF image of the particle with the phases denoted. b) SADP of β silicon carbide, **B** = [0 1 1]. c) SADP of aluminum, **B** = [0 0 1].
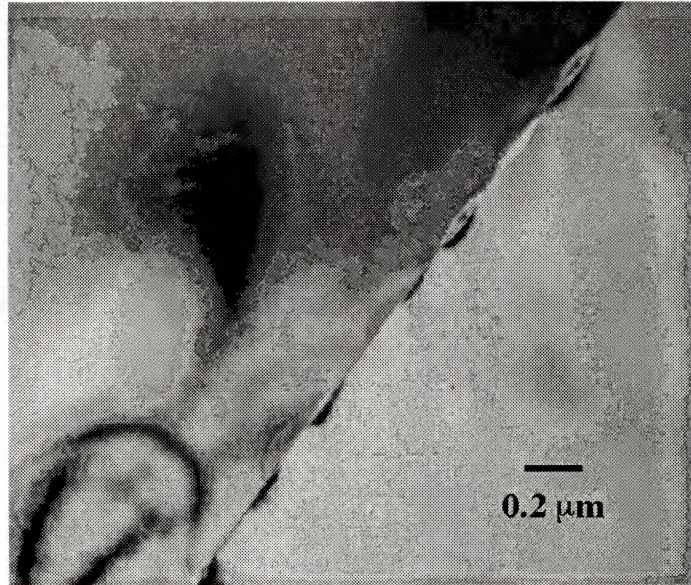
Figure 4.41 Bright field TEM of necklace arrangement of particles along a Mo(Si,Al)$_2$
grain boundary.

4.4 Alloying Additions and Other Alloy Systems

4.4.1 The W-Si-Al System

It was postulated that the behavior observed for Mo(Si,Al)$_2$ should extend to other
X-Si-Al systems when contaminated with crabon. A material (X) that forms an X(Si,Al)$_2$
compound yet has the same affinity for carbon as does molybdenum was needed. The
similarities that were established between tungsten and molybdenum in Table 2.3 made it
an ideal choice to test this assumption. A thermodynamic estimation was performed using
Thermocalc to determine whether tungsten would behave analogously with molybdenum
with respect to the stability of their respective carbide phases (Figure 4.42). The results
indicated similar behavior between molybdenum and tungsten with respect to the free
energy of formation of the various carbide phases in the presence of excess carbon.

Alloys were produced of W(Si,Al)$_2$ with a composition analogous to the 20 at%
aluminum composition produced for Mo(Si,Al)$_2$ samples. Compacts were produced by the

blended powder technique from powders of the same size and purity of the corresponding Mo-Si-Al powders. Scanning electron microscopy of the resulting compacts indicates that the samples are nearly-single-phase, containing secondary phases in the forms of alumina and a phase of higher average atomic number which WDS indicates to be T1 $W_5(Si,Al)_3$ (Figure 4.43). The results from XRD of a thin section of the bulk compact indicate the sample is comprised of mostly two phases; hexagonal C40 and tetragonal $C11_b$ (Figure 4.44). While there is no available ternary isotherm for the W-SI-Al system, it is assumed that there is solubility of aluminum in the binary $C11_b$ phase since EDS scans indicate aluminum to be present throughout the matrix. Since the overall stoichiometry of the alloy remained $W(Si,Al)_2$, it was assumed that the sample would exhibit similar behavior to the nearly-single-phase Mo-Si-Al-based alloys. A small region of carbide phase was observed in the polished surface of the tungsten-based alloy. A spectrum obtained by EDS strongly indicates that the particle is SiC (Figure 4.45)

Fractured samples were examined in the SEM for evidence of the same grain boundary phases that were observed in $Mo(Si,Al)_2$. Unfortunately the mode of fracture of the W-based alloys differed from the Mo-based alloys in that the surfaces produced by fracture were not fully intergranular (Figure 4.46). Despite the often transgranular nature of the fracture path, an adequate amount of grain boundary area was exposed in the fracture. The presence of alumina was confirmed by performing EDS analysis on the small charging particles in the boundaries since these had essentially the same morphology as the alumina formed in the Mo-based alloys (Figure 4.47).

Scanning electron microscopy revealed small dimpled regions on the grain boundary surfaces of the tungsten-based alloys (Figure 4.48). These regions were similar in size and morphology to those observed in the molybdenum-based alloys. Inspection by EDS indicates that these regions are each comprised of an aluminum-rich region and a
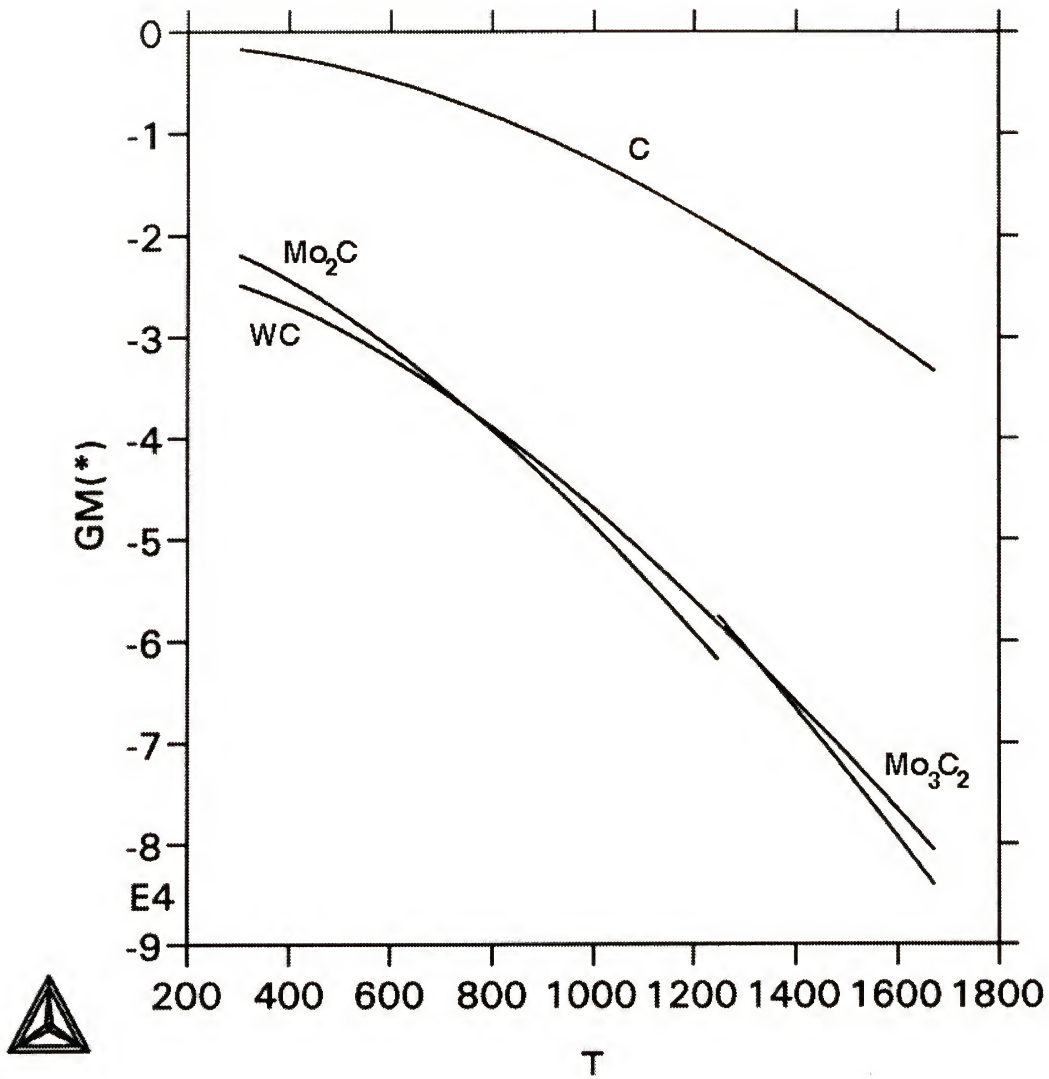
Figure 4.42 Gibbs free energy per gram-atom for tungsten carbide, molybdenum carbides, and carbon as a function of temperature. This plot illustrates the similarities between W and Mo with respect to the free energy formation of carbide phases.
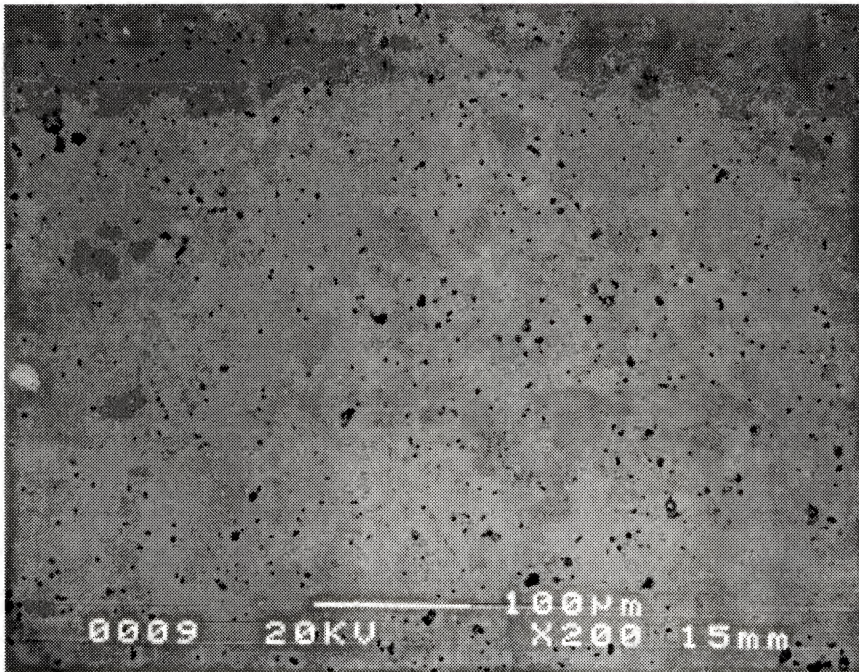
Figure 4.43 Backscattered electron image of $W(Si,Al)_2$ sample produced by blended powder technique. Gray matrix indicates the $C11_b$ and C40 phases, black regions are porosity and/or alumina; bright particle to the far left is the T1 $W_5(Si,Al)_3$ phase.
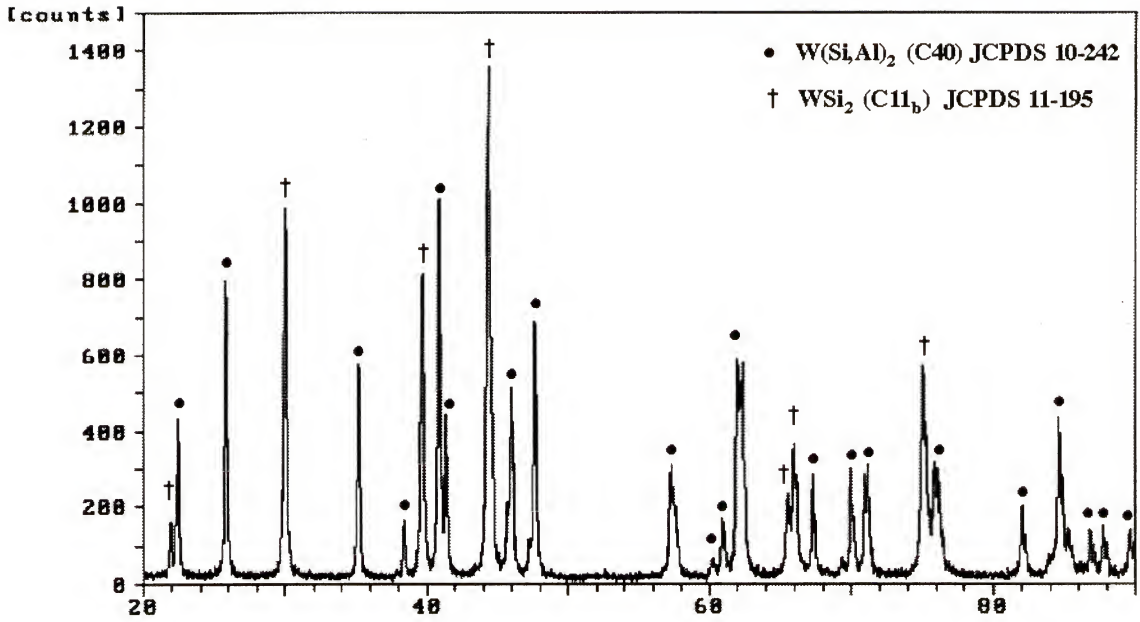
Figure 4.44 Spectrum obtained by XRD of the $W(Si,Al)_2$ alloy produced by the blended powder technique.
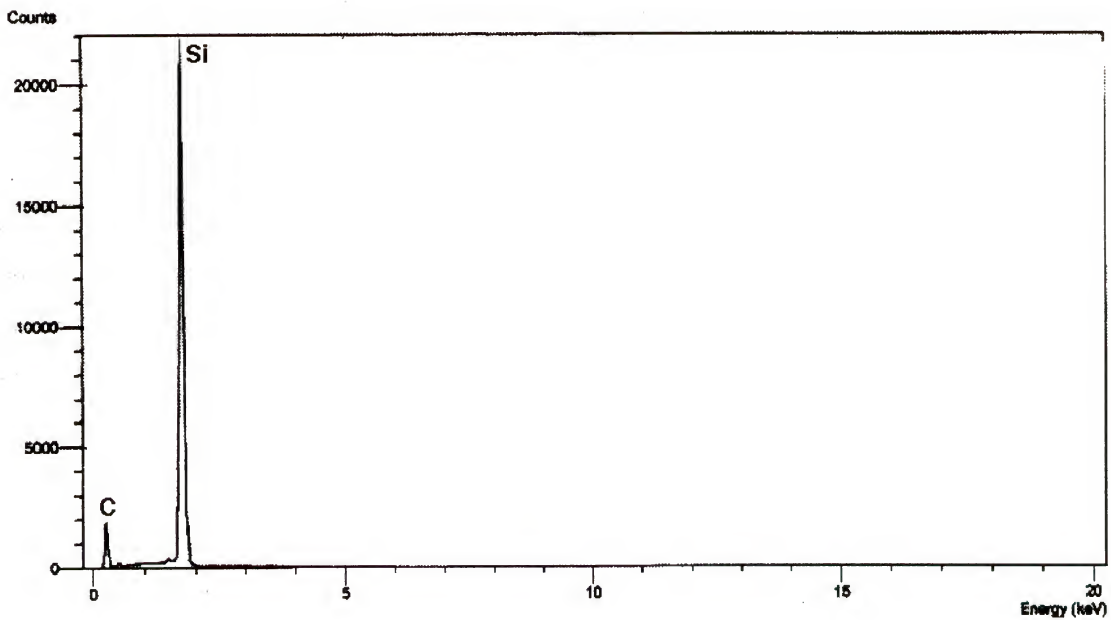
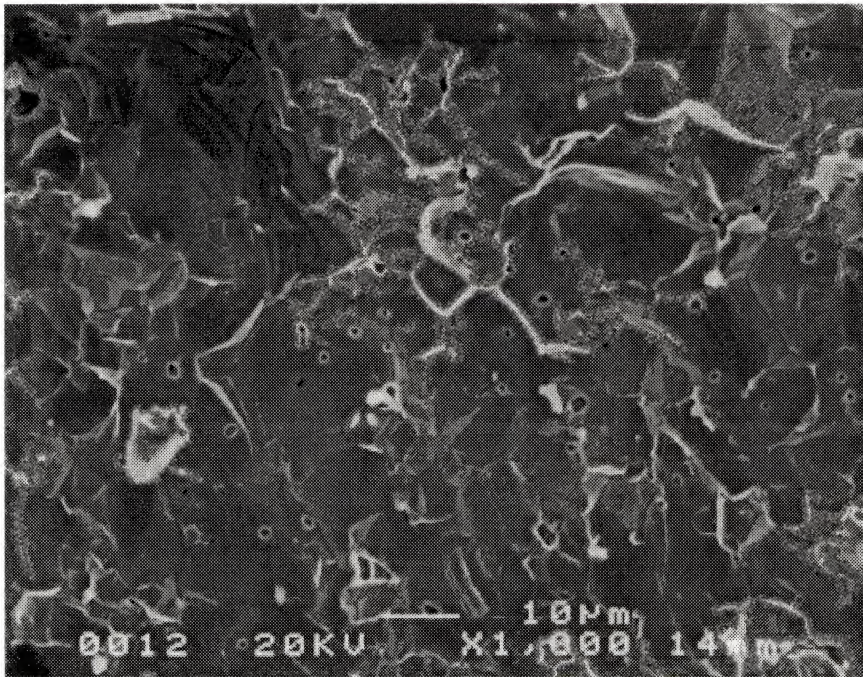Figure 4.45 Spectrum obtained by EDS of a carbide particle found in the polished surface of the $W(Si,Al)_2$ alloy.
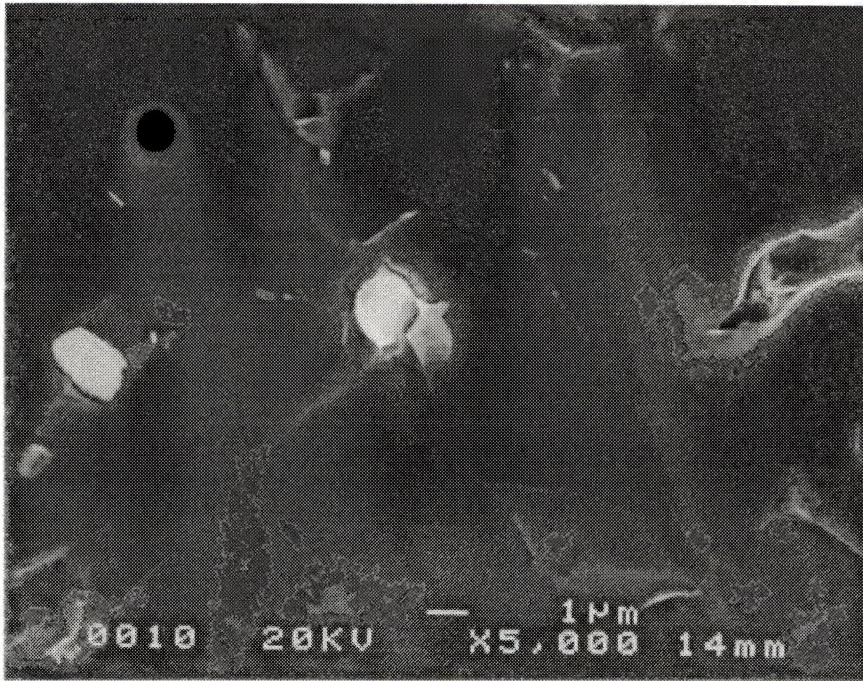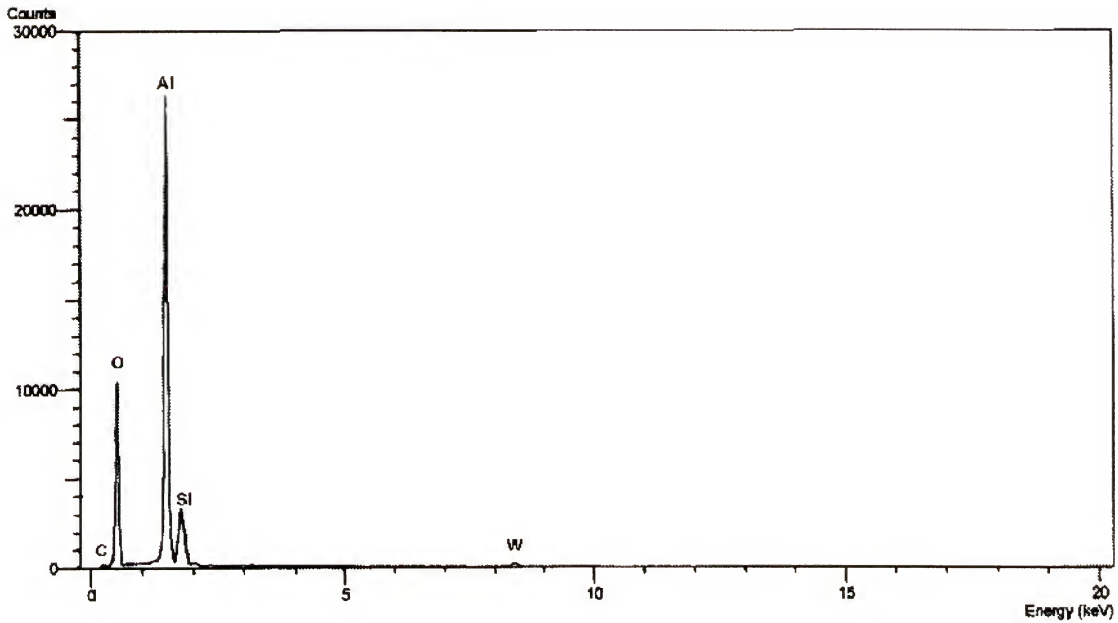
Figure 4.46 Secondary electron image of a fracture surface in W(Si,Al)$_2$. Note: the fracture surface is mostly transgranular, unlike the fracture surfaces observed in the Mo(Si,Al)$_2$ alloys.

(a)

(b)

Figure 4.47 Evidence of aluminum oxide present in the grain boundaries of the $W(Si,Al)_2$
alloy. a) Secondary electron image of alumina (bright particles) present in the
fracture surface. b) spectrum obtained by EDS of the same particle. Note: small Si
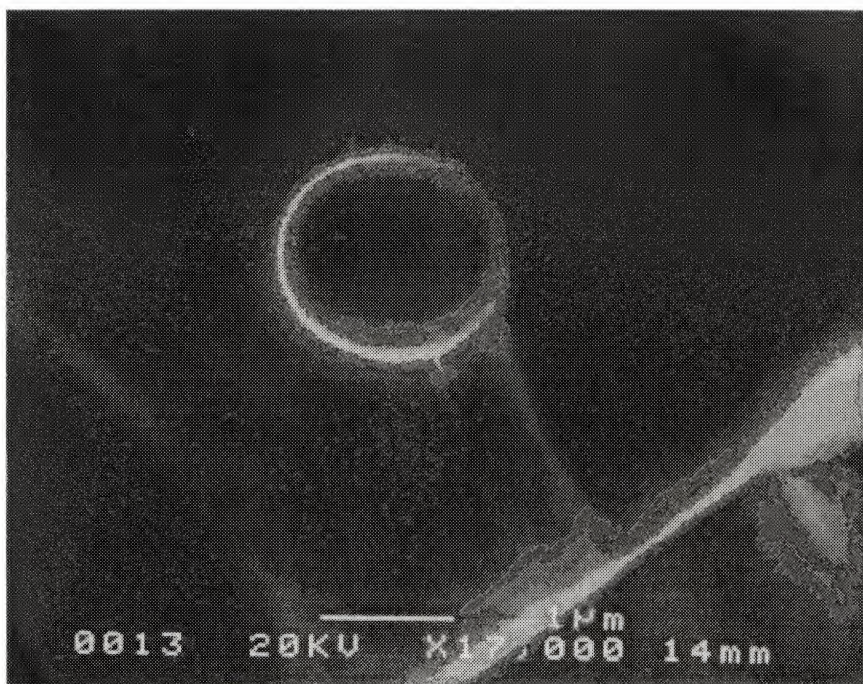and W peaks possibly due to beam interaction with surrounding matrix.

Figure 4.48 Secondary electron image of a dimpled region on the fracture surface of the $W(Si,Al)_2$ alloy.

silicon/carbon-rich region (Figure 4.49). The edge of the dimpled regions show an elevation in Si and C while the interior region appears rich in aluminum.

Humid air oxidation testing was performed at 200°C for 160 hours on the fractured $W(Si,Al)_2$ surfaces for comparison to the $Mo(Si,Al)_2$. The behavior was identical to that seen in the molybdenum-based materials. These findings indicate a generality in the mechanism of environmental sensitivity of alumino-silicides with small carbon impurities. The surfaces also displayed grain boundary recession around alumina particles, although examination of triple-points was difficult due to the significant amount of transgranular fracture (Figure 4.50).
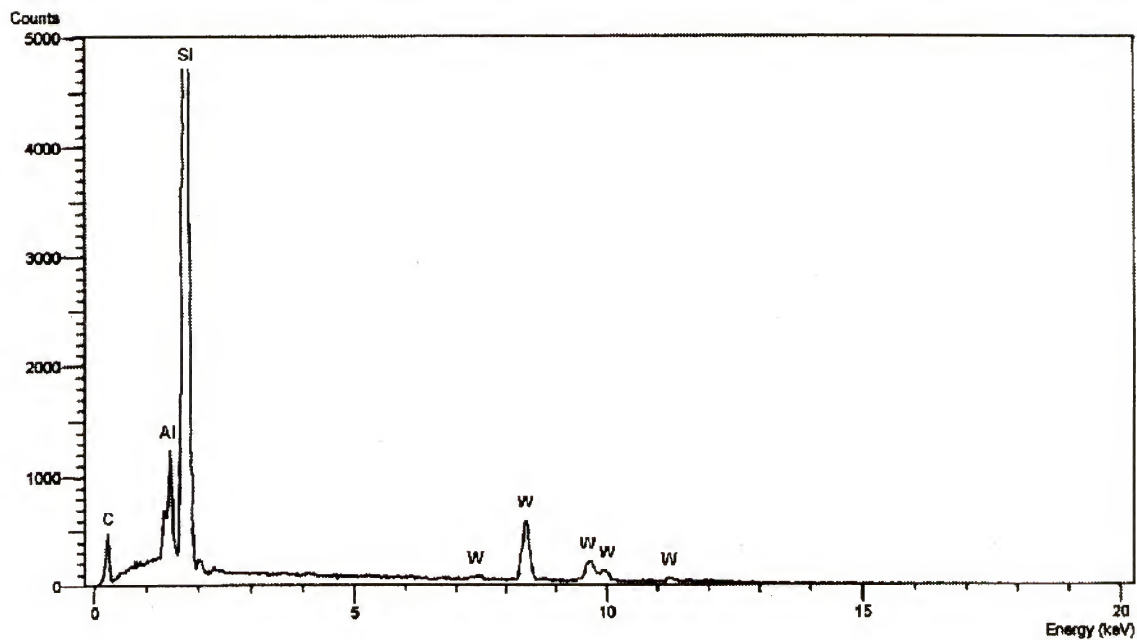
(a)
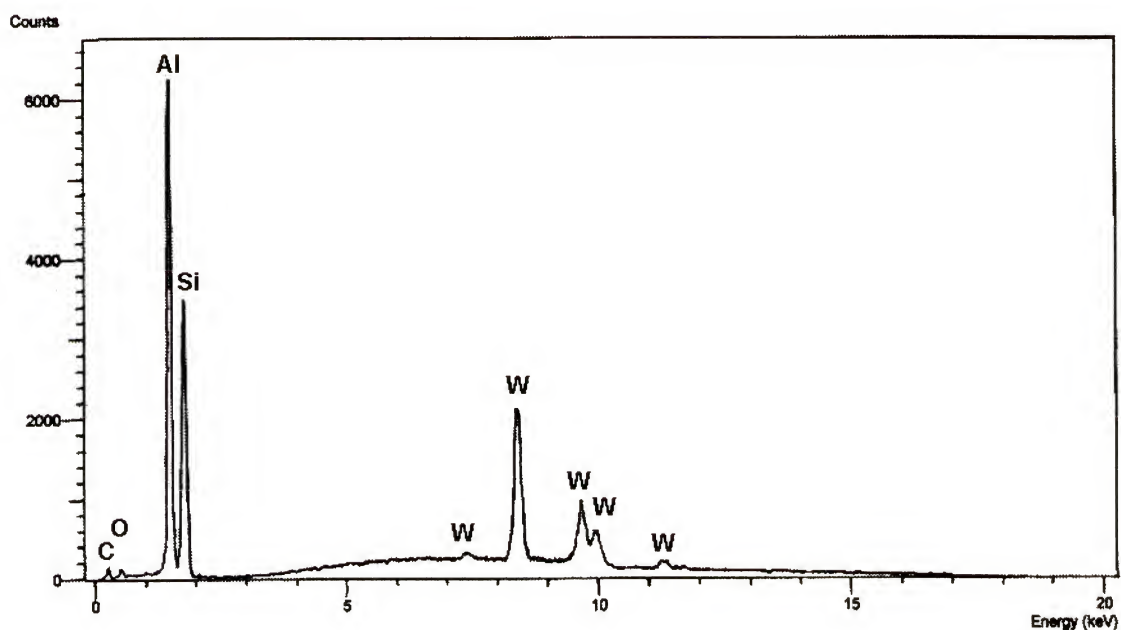
(b)

Figure 4.49 Spectra obtained from EDS of dimpled regions on $W(Si,Al)_2$ grain facet. a) Spectrum taken from the edge of the dimpled region, indicating elevated levels of Si and C. b) Spectrum obtained from the interior of the dimpled region indicating an elevated level of Al.
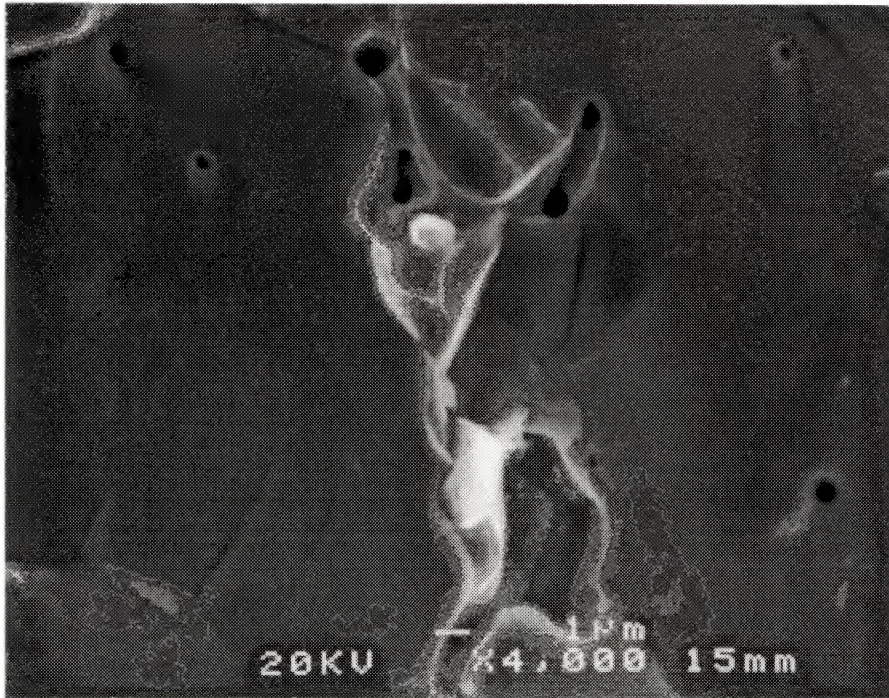
Figure 4.50 Secondary electron image of a receded grain boundary intersecting the fracture surface of the W(Si,Al)$_2$ alloy. Bright particles in the boundary are alumina. Black regions are either porosity or sites of alumina pullout. Sample was exposed to air at 200°C for 160 hours.

4.4.2 The Mo-Ti-Si-Al system

As mentioned in the literature review, the C40 compound is known to exist in solid solutions of $(Mo,X)Si_2$ alloys, where X represents Nb, Ta, Cr and Ti. Working on the assumption that the $(Mo,Ti)(Si,Al)_2$ compound would form the C40 structure, samples were made for assessment of environmental properties. This investigation began before the discovery of the SiC/Al particles, and was inspired by the notion that a pest phenomenon was occurring in the C40 because of the increased Mo/Si ratio. Titanium additions were made to the alloy by the use of titanium disilicide powder, in substitution for enough molybdenum disilicide to create a $(Mo,Ti)(Si,Al)_2$ almost single-phase alloy containing five atomic percent titanium. The resulting alloy was ground and analyzed by XRD for verification of the formation of the C40 structure (Figure 4.51). Upon verification of C40 formation, the samples were examined in the SEM to assess the microstructure and look for possible secondary phases undetected by the XRD. The resulting microstructure appears to be nearly single phase with the exception of alumina and porosity as seen in the other ternary alloys (Figure 4.52).

Microhardness tests were performed on the Ti-containing C40 material in order to qualitatively assess the effect Ti additions might have on the grain boundary properties. The indents produced by the microhardness tester were square and showed little or no signs of intergranular decohesion (Figure 4.53). The cracks emanating from the corners of the indent appear to indicate transgranular cracking. This evidence was taken to show that Ti did, in some way, alter the grain boundary behavior of the C40 compound.
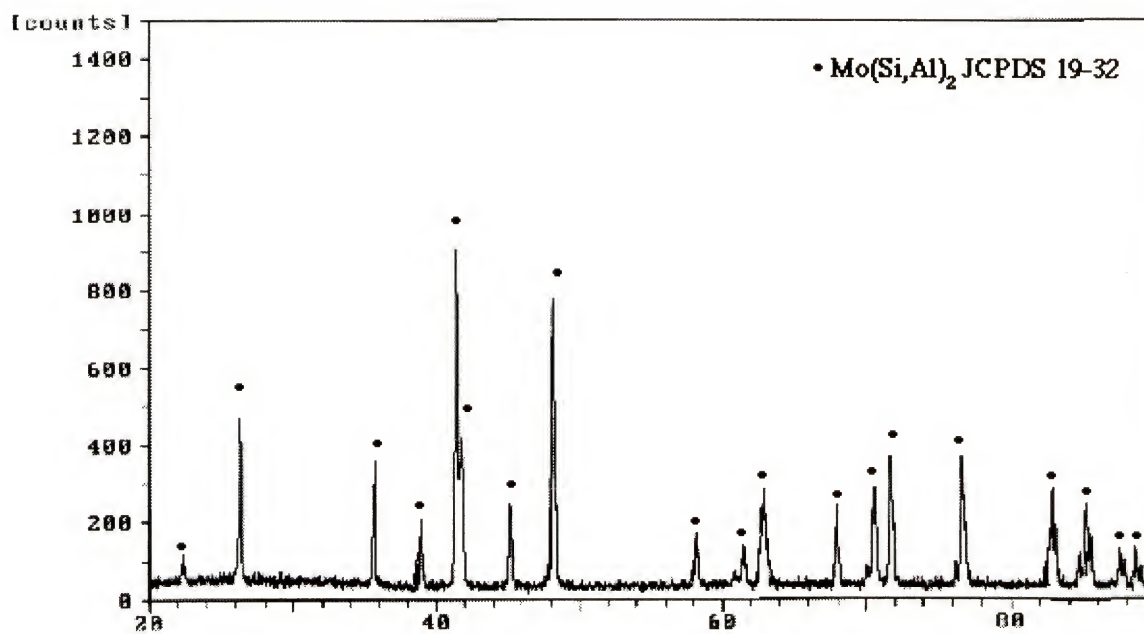
Figure 4.51 Spectrum obtained by XRD of (Mo,Ti)(Si,Al)$_2$ alloy. Peaks are consistent with the C40 structure observed in ternary Mo(Si,Al)$_2$.
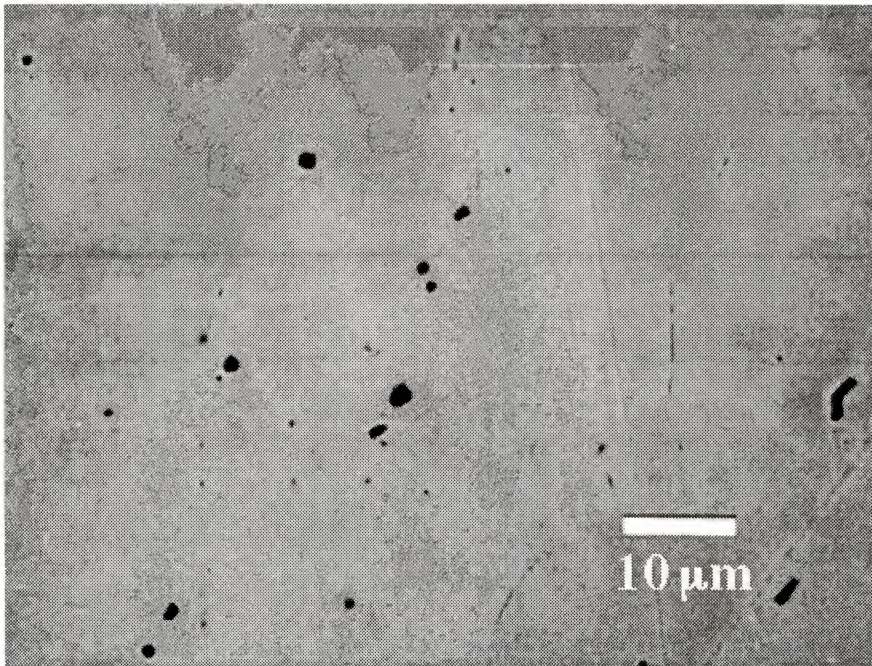
Figure 4.52 Secondary electron image of the microstructure of $(Mo,Ti)(Si,Al)_2$ produced by blended powder technique. Gray matrix represents single-phase C40. Dark regions are alumina and/or porosity.
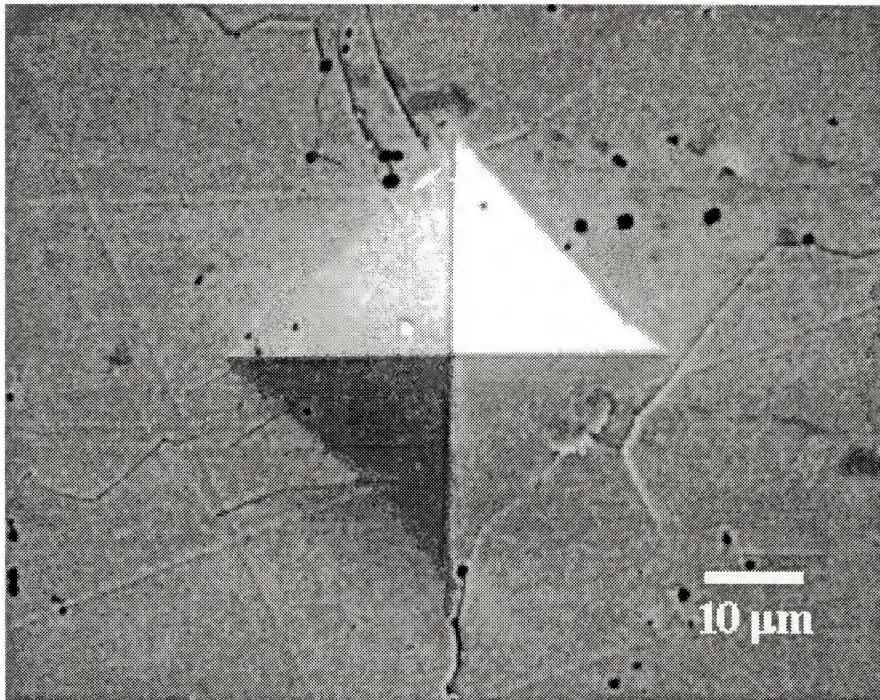
Figure 4.53 Secondary electron image of a Vickers microhardness indent in C40-
(Mo,Ti)(Si,Al)$_2$. Note: the absence of grain boundary cracking observed
in ternary Mo(Si,Al)$_2$

Fortunately the ability to produce intergranular fracture was not lost due to the additions of titanium; thus, suitable samples were made for inspection by *in-situ* fracture testing in the AES. The resulting analysis of the grain boundary surfaces revealed the presence of carbon on the boundaries as well as oxygen and the expected alloy constituents (Figure 4.54). Depth profiles indicate that the alloy behaves similarly to the ternary alloys, in that, while Mo appears depleted at the boundaries, all other components appear enriched. As stated previously, the information from the AES depth profiles can be interpreted in different ways, but the presence of carbon at the boundaries is definitely indicated by the data shown (Figure 4.55).

Atmospheric exposure tests were performed on the Ti-containing samples to assess whether the alloying additions could mitigate the effects seen in the ternary alloys. Samples were polished then heated in moist air at 200°C for 160 hours. The samples were inspected optically for signs of atmospheric attack (Figure 4.56) and there was no evidence of boundary grooving or attack at triple points. Thus, it appears that the titanium additions effectively eliminate the problem experienced in the ternary alloys. A possible mechanism for this lies in the fact that the formation of TiC is greatly favored over the formation of both Al_4C_3 and SiC. In fact, Ti additions have been used in aluminum alloy reinforced with graphite or SiC, to prevent the formation of aluminum carbide at interfaces [83, 91].

Transmission electron microscopy of the titanium alloys was performed in order to determine the effects of Ti on the microstructure. As expected alumina particles were present along the grain boundaries and there was no evidence of the coupled SiC/Al particles observed in the ternary alloys although some aluminum was observed along the boundaries. Evidence of TiC was also observed as seen in Figure 4.57. It should be noted that TiC was not observed commonly in the microstructure. The presence of TiC and the absence of SiC is predicted from thermodynamic data and is suspected to be partially responsible for preventing the atmospheric degradation of these samples since it is energetically impossible to form Al_4C_3 from aluminum in contact with TiC.
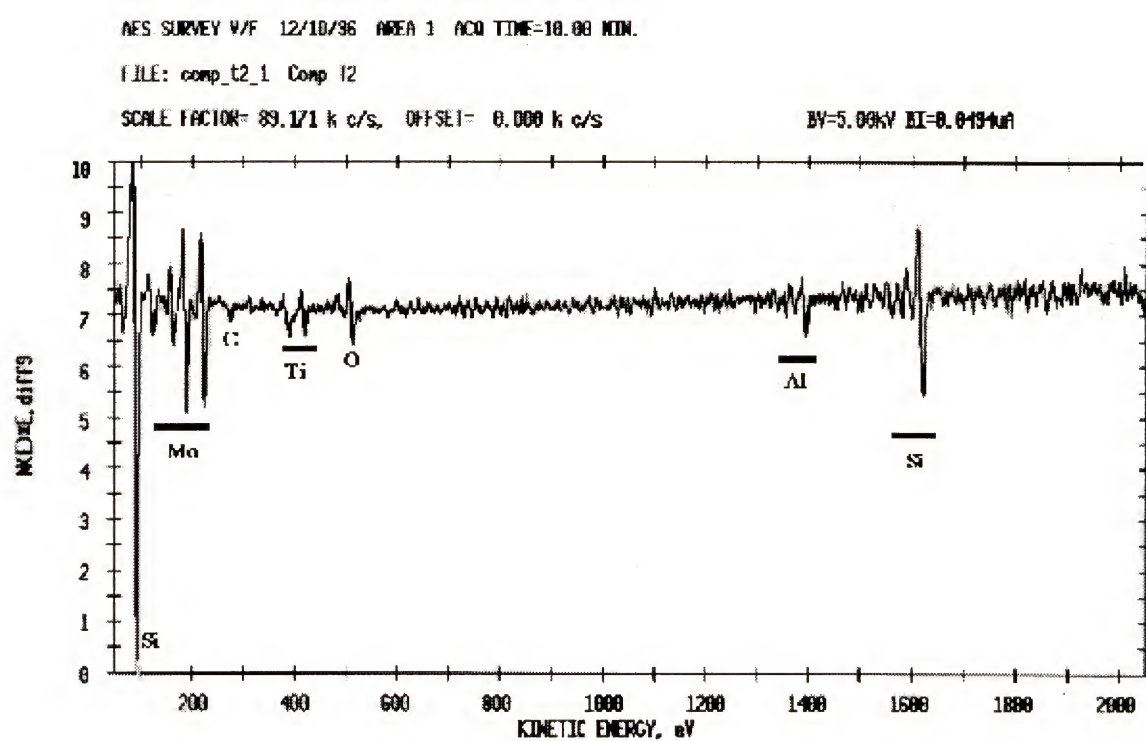
AES SURVEY V/F 12/18/96 AREA 1 ACQ TIME=10.00 MIN.

FILE: comp_t2_1 Comp #2

SCALE FACTOR= 89.171 k c/s, OFFSET= 0.000 k c/s   BV=5.00kV BI=0.0194uA

Figure 4.54 Spectrum obtained by AES from grain boundary surface of C40-
(Mo,Ti)(Si,Al)$_2$. Sample was factured in the high vacuum chamber of the AES.

AES PROFILE V/F ALT. 12/18/96 EL=Ti2 REG 7 AREA 1 SPUTTER TIME=18.00 MIN.

FILE: comp_t2_2 Comp T2

SCALE FACTOR= 2.099 k c/s, OFFSET= 0.000 k c/s   BV=5.00kV BI=0.0494uA
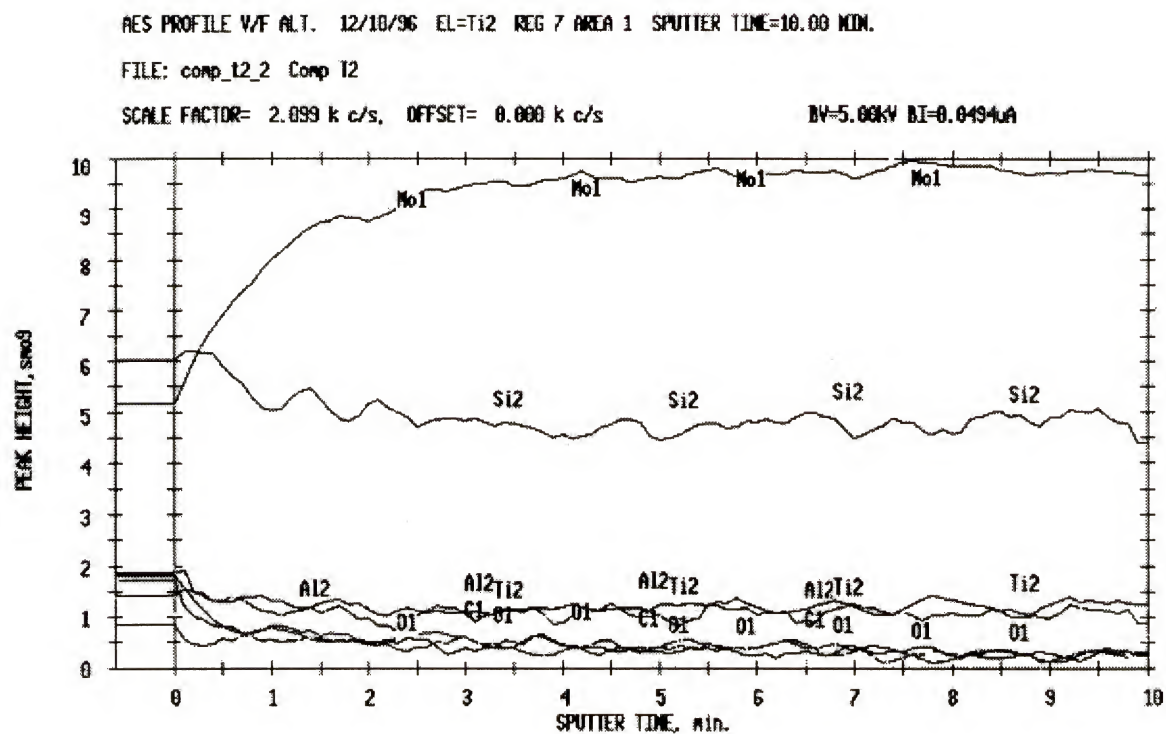
Figure 4.55 Chemical depth profile obtained by AES of an *in-situ* fracture surface of C40-$(Mo,Ti)(Si,Al)_2$. Sputter time indicates depth into the grain.
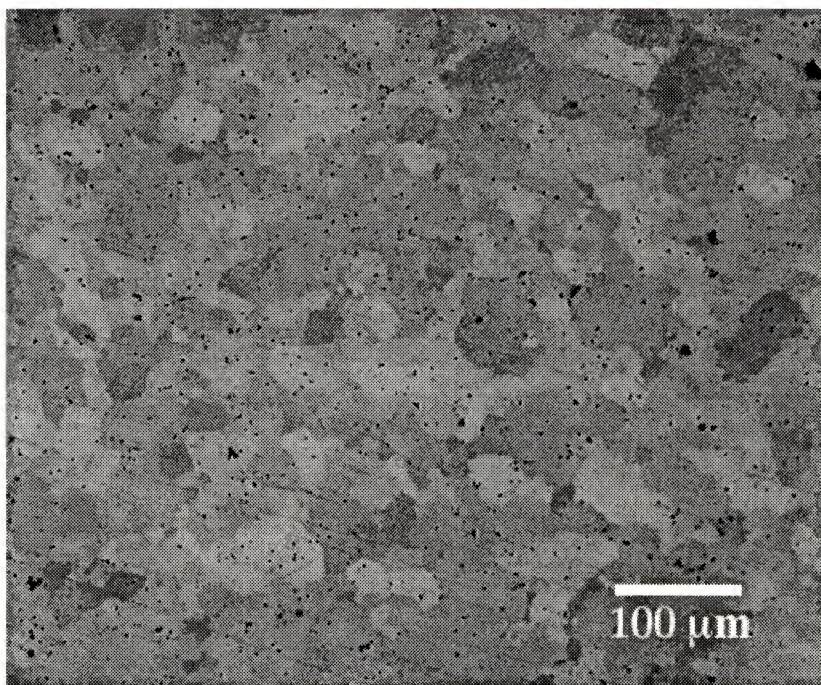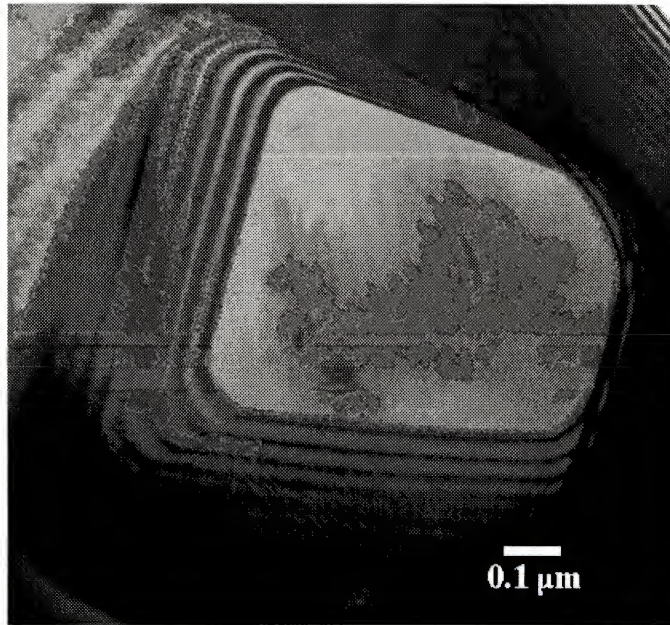
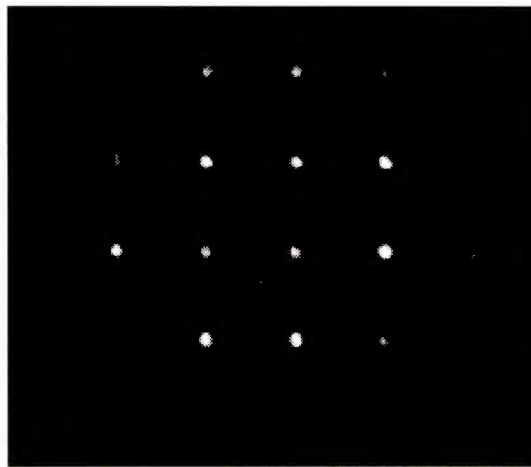Figure 4.56 Optical micrograph of C40- $(Mo,Ti)(Si,Al)_2$ after 160 hours in moist air at 200°C. The sample shows no sign of the attack that occured in the ternary $Mo(Si,Al)_2$ material.
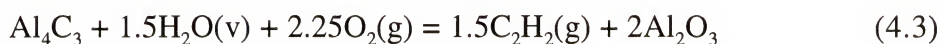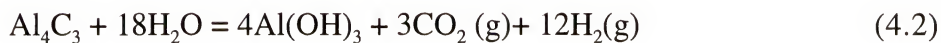
(a)

(b)

Figure 4.57 Transmission electron microscopy of a titanium carbide particle found in the (Mo,Ti)(Si,Al)$_2$ alloy. a) Bright field image of the TiC particle. b) [0 0 1] SADP taken from the TiC particle.

4.5 General Discussion

A review of the thermodynamics of the Al-Si-C system reveals that Al and SiC, although commonly used together in SiC-reinforced aluminum, are not in equilibrium with each other at room temperature. In SiC-reinforced aluminum, the reaction between the matrix and the reinforcing phase is mitigated by both coatings on the SiC or the silicon enrichment of the aluminum matrix immediately surrounding the SiC induced by the rejection of Si associated with Al_4C_3 formation. At room temperature there is a mild driving force (ΔG = -2.673 kJ/mol) for the reaction of the phases to form silicon and aluminum carbide according to the following reaction:

$$4Al + 3SiC = 3Si + Al_4C_3 \qquad (4.1)$$

The Al_4C_3 compound is noted for its extreme environmental sensitivity and has a high driving force to react with aqueous solutions and moist air by the following reactions [82]:

$$Al_4C_3 + 18H_2O = 4Al(OH)_3 + 3CO_2\ (g) + 12H_2(g) \qquad (4.2)$$

$$Al_4C_3 + 1.5H_2O(v) + 2.25O_2(g) = 1.5C_2H_2(g) + 2Al_2O_3 \qquad (4.3)$$

The noted environmental sensitivity of the aluminum carbide compound combined with the evidence of carbon consumption in the environmental attack and the silicon and alumina products of the observed reaction, led to the development of the following scenario. Upon melting of the aluminum powder during the heating cycle of the hot pressing operation, liquid aluminum in contact with the graphite paper dissolved carbon and permitted its transport into the sample. The probability that the samples were mildly hyperstoichiometric with respect to aluminum and silicon (as a result of the narrow solubility range for the C40 compound) left an aluminum-rich liquid which formed the coupled SiC/Al particles observed in the TEM. The reaction between silicon carbide and aluminum to form Al_4C_3 and Si (see eqn 4.1) was enhanced by the consumption of the

forming Al_4C_3 by environmental attack thus pulling the reaction forward by a LeChatelier effect. The byproducts of this sequence of events would be Al_2O_3, Si and $C_2H_2(g)$, the first of which has been directly observed and presence of the second is strongly suggested as mentioned previously in this chapter. The removal of the carbon by gaseous byproduct is consistent with the EDS results on the attacked fracture surfaces which show no evidence of carbon in samples after long term atmospheric exposure.

The formation of the coupled Al/SiC particles is consistent with the work of Park [82] who observed that, at high temperatures, SiC is in equilibrium with an aluminum liquid containing dissolved silicon. The SiC particles, once formed, are sluggish to dissolve and could remain intact despite the fact that the aluminum and silicon carbide are not in equilibrium at lower temperatures. The forward reaction of silicon carbide and aluminum to form aluminum carbide and silicon at room temperature has been shown by calculations to be energetically favored. This reaction is known to be catalyzed by the presence of alumina. It is assumed that if there is not a reaction layer present between the SiC and Al, then the internal oxidation of aluminum would provide the catalyst for the initial formation of aluminum carbide. The continued reaction of atmospheric species with the aluminum carbide would produce more alumina and, in turn, perpetuate the reaction to the exhaustion of the carbon in the silicon carbide. The reaction of these two phases would leave alumina and silicon as the only solid products, which is consistent with the observations on oxidized fracture surfaces. The reaction scenario just described would produce alumina and silicon with a combined volume 14% greater than the original volume of the coupled SiC/Al particles. This volumetric increase would create tensile stress on the grain boundaries, essentially pulling the boundaries apart. This mechanism is addressed in Section 2.4.1 of this text, as a cause of pest disintegration. Figures 4.58 through 4.62 schematically depict the process described above.
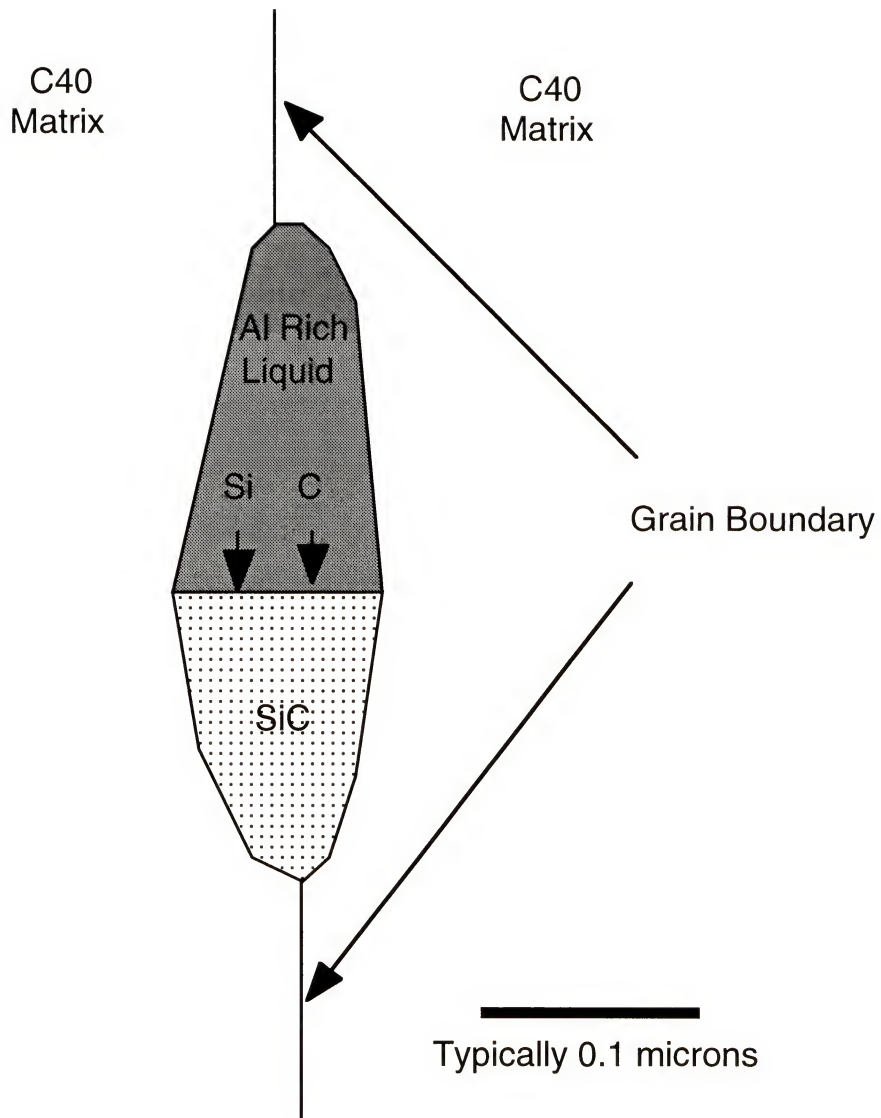
Figure 4.58 Schematic representation of the formation of SiC as a primary precipitate from the aluminum rich liquid present in C40 grain boundaries at processing temperature.
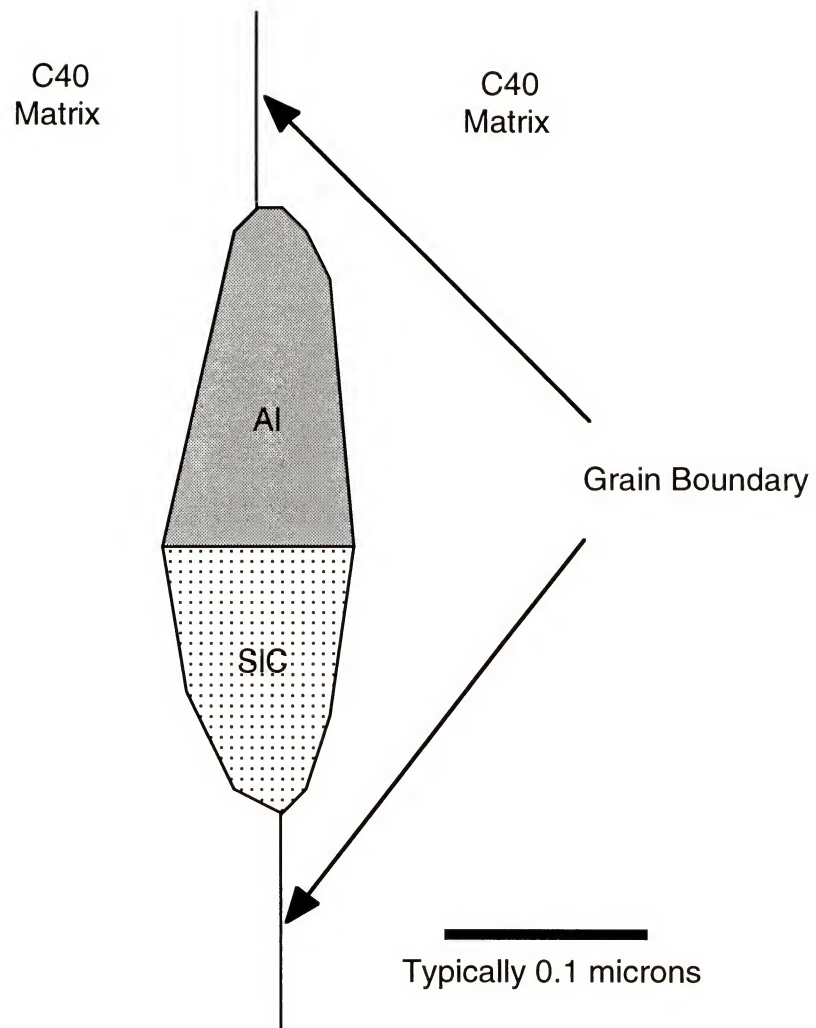
Figure 4.59 Schematic representation of the coupled SiC/Al particles observed in the TEM analysis of powder processed C40.
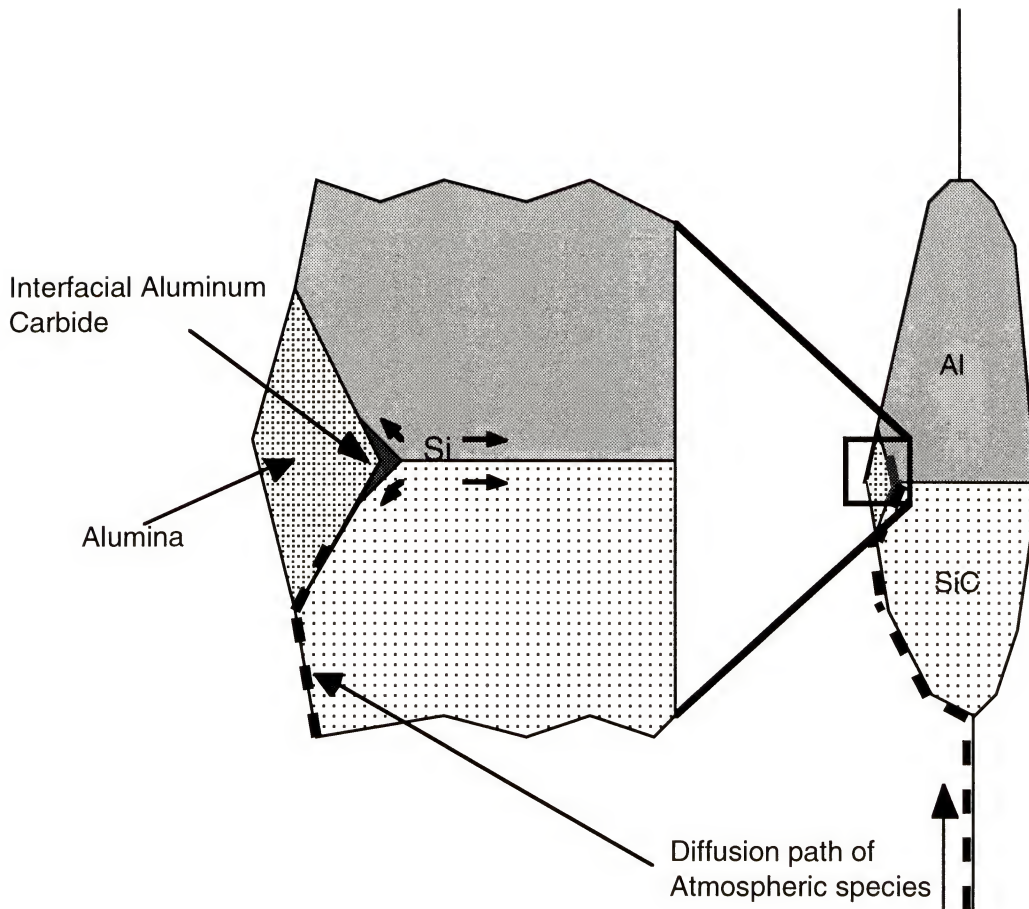
Figure 4.60 Schematic representation of the incipient stages of atmospheric attack of C40. The dashed line represents the diffusion path along the grain boundary and interphase boundaries. Note: the initial oxidation of Al provides active aluminum sites for catalysis of the aluminum carbide formation. Local rejection of silicon is also depicted.
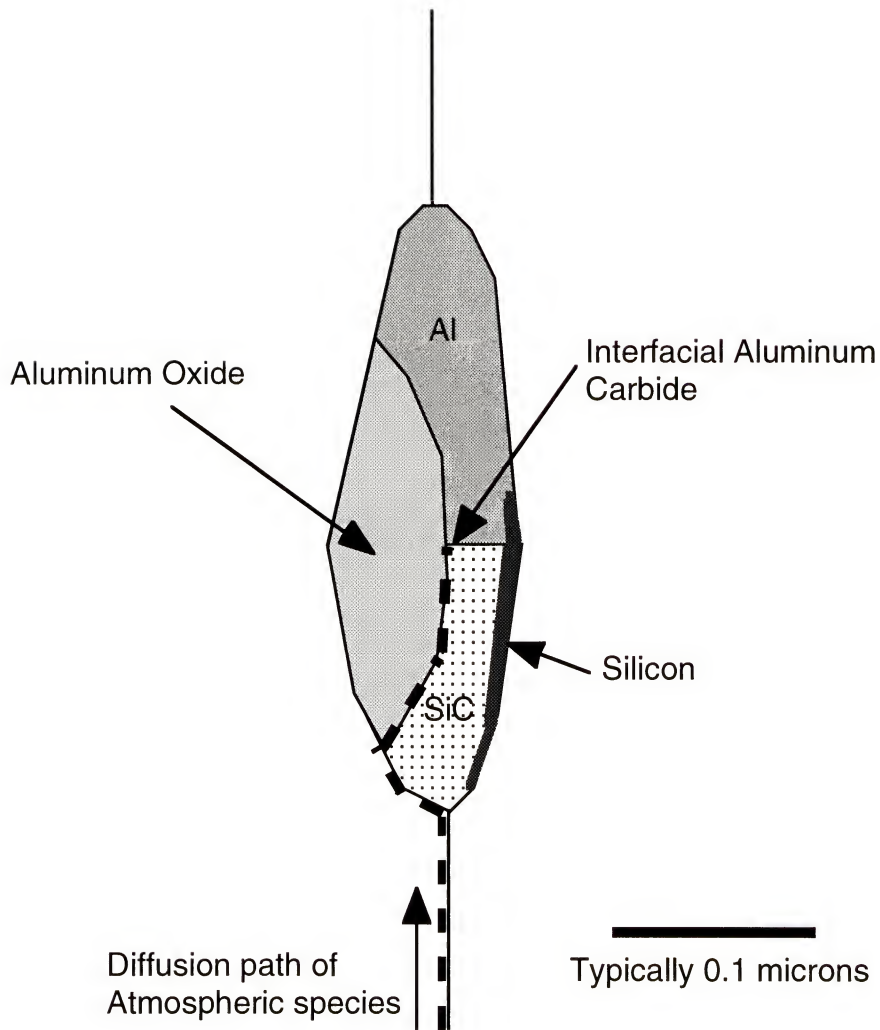
Figure 4.61 Schematic representation of the growth of alumina and rejection of silicon in the continued reaction of the coupled SiC/Al particle.

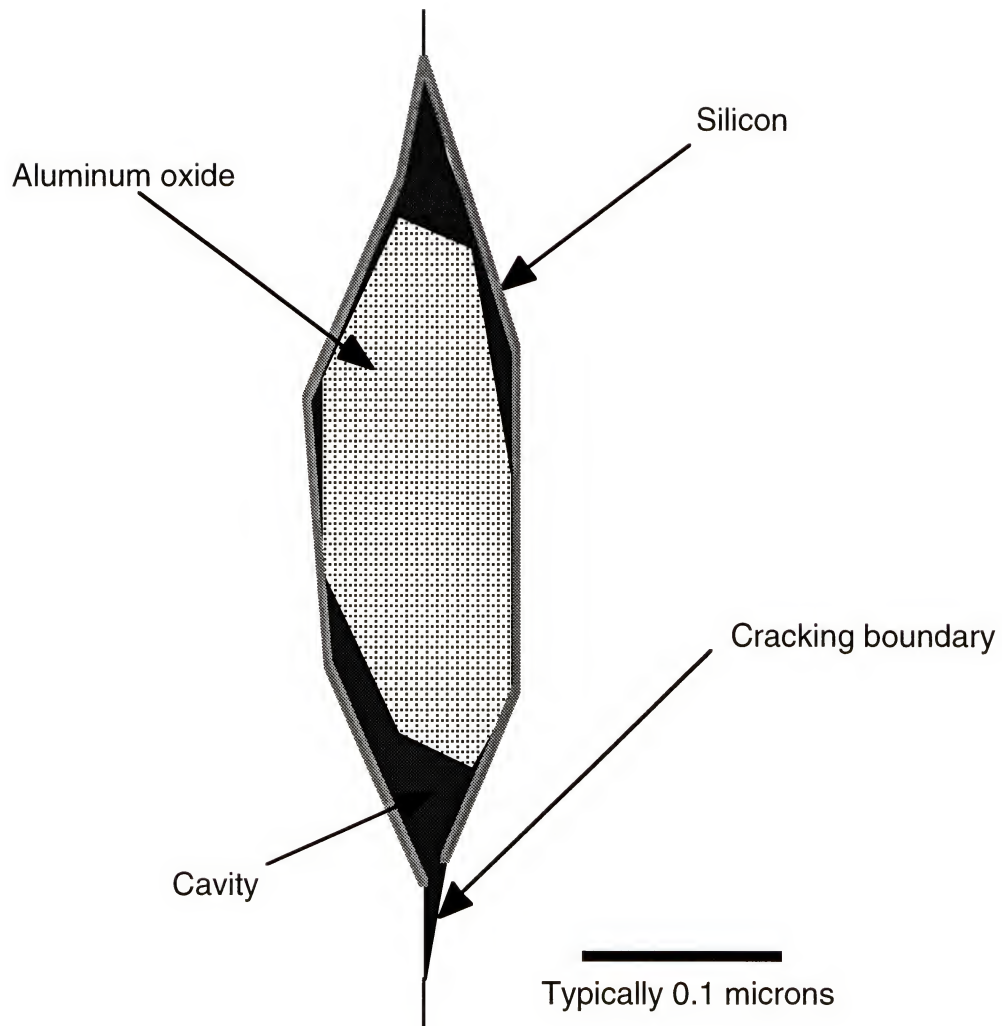Figure 4.62 Schematic of the final state of the former SiC/Al particle. The cavity and boundary cracking are resultant from the 14% volumetric expansion from the formation of alumina and silicon. This morphology is observed in the SEM analysis of samples after long term atmospheric exposure.

Results from a thermodynamic assessment of the titanium effect on these alloys shows that the formation of titanium carbide is highly favored over the formation of silicon carbide. Therefore, it is assumed that titanium adequately "ties up" the carbon to prevent the formation of the coupled SiC/Al particles in the boundaries. A similar estimation was performed for each of the elements listed as possible Mo substitutes in Table 2.3. The results have been graphically arranged to show both suitable and unsuitable alloying additions on the basis of the element's ability to "tie up" the carbon (Figure 4.63). Some of the elements in Table 2.3 (Re, Ni, Te, and Fe) form silicide or aluminide compounds in the presence of Al, Si and C, thus these elements were not included in Figure 4.64 since it could not be extrapolated from experimental results whether "tying up" Al or Si would affect formation of the SiC/Al particles. Elements listed above SiC in the figure, are considered unsuitable as they are not energetically capable of preventing SiC formation. Elements listed below SiC are considered suitable as they would likely prevent the formation of SiC by forming their respective carbide phase. It is important to note that the alloying additions would have to exceed the amount of the element required to completely consume the carbon, to prevent formation of SiC. A compilation of the free energy plots for each of the alloying additions is available in the Appendix.
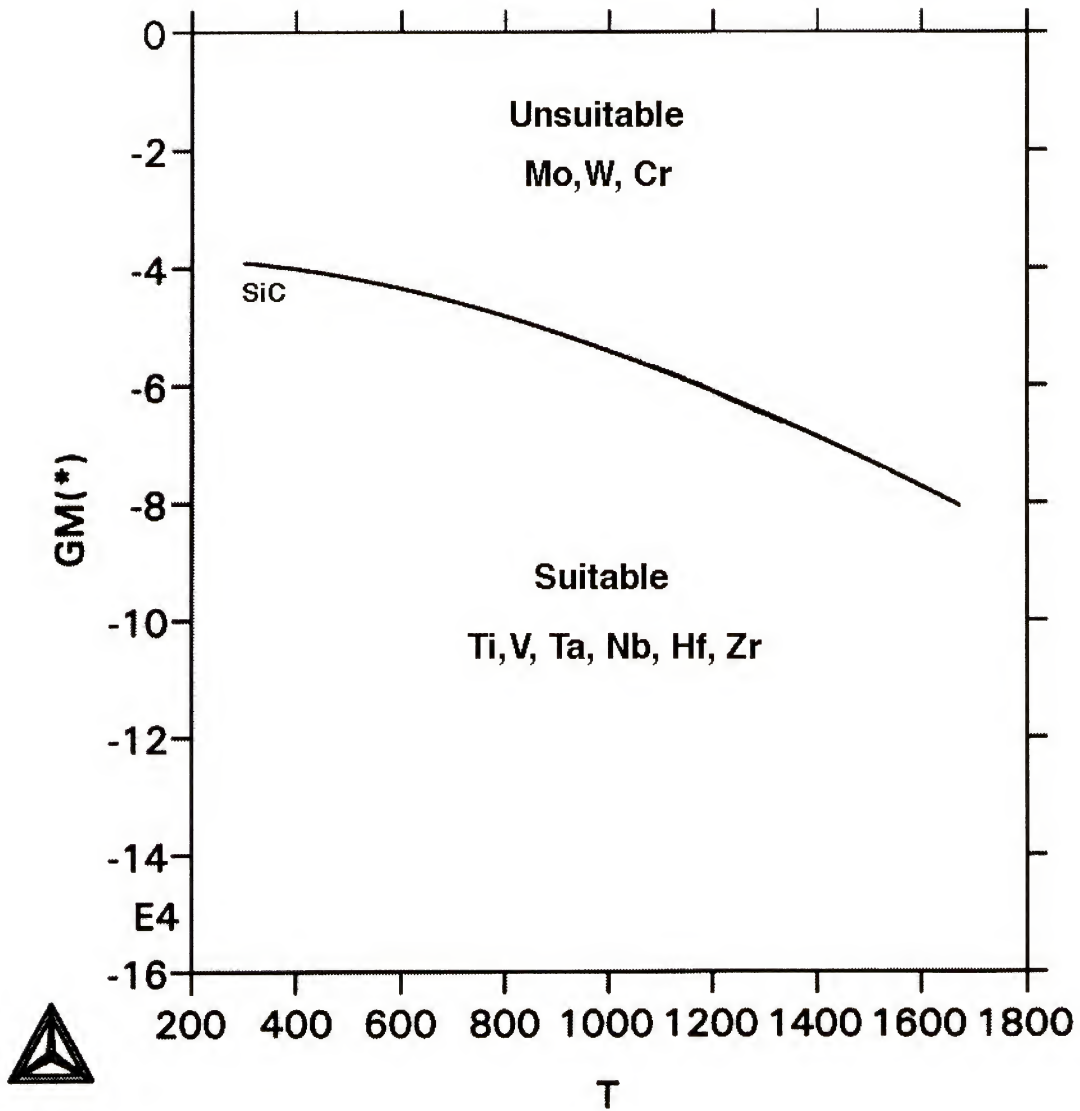
Figure 4.63 Free energy plot of SiC with a listing of the elements considered for substitutional alloying in $(Mo,X)(Si,Al)_2$. The elements are grouped by their ability to form carbide phases, and are labeled for suitability accordingly.

CHAPTER 5
SUMMARY & CONCLUSIONS

Several powder processing routes have been established as viable methods for the production of the $Mo(Si,Al)_2$ intermetallic compound. Arc-melting of bulk materials followed by comminution and hot pressing of the subsequent powders was shown to provide near single-phase microstructures. The drawback of the arc-melting method is the lengthy comminution process which is also responsible for the lack of control over grain size. Mechanical alloying has been shown to be a promising route for the production $Mo(Si,Al)_2$ given the ability to prevent contamination of the milling charge by the vial and milling media. This process does show greater control over grain size than other methods, and should be considered for future processing investigations of this material. The blended powder technique in which the C40 phase formed during the heating cycle of the hot compaction of powders has been shown to be the preferred method for production of dense, nearly single-phase $Mo(Si,Al)_2$. The simplicity of the process combined with the production of optimized microstructures made this process the choice for production of C40 for further investigation.

The Mo-Si-Al isothermal phase diagram was evaluated at 1400°C. The strategy for the assessment of the diagram involved selection of alloy compositions based on the conflicting claims of previous investigations. The presence of C54 $Mo(Si,Al)_2$ at 1400°C was verified. It was also established that the binary Mo_3Al_8 phase is in equilibrium with both C54 and the T1 $Mo_5(Si,Al)_3$ phase. The ternary terminal end of the T1 phase was also determined, establishing the extent of aluminum solubility in the 5-3 silicide. A more accurate depiction of the shape of the T1 boundary in equilibrium with C40 was also produced.

Discovery of an environmentally induced grain boundary degradation diverted the investigation from the initial goal of determining the mechanical properties of the C40 phase. Attempts to accelerate the observed phenomenon by heating in humid air were successful, indicating a moisture sensitive reaction was occurring. Findings from electron microscopy show the presence of coupled Al/SiC particles distributed on the grain boundaries of the C40 samples. Carbon picked up from the graphite dies used in hot pressing is thought to be the source of the carbon in the SiC phase.

The reaction of the Al and SiC to form Al_4C_3 and Si has been shown to be energetically possible. The aluminum carbide phase is known for extreme sensitivity to moist air. The reaction of Al_4C_3 with moist air is consistent with the observed behavior with respect to the byproducts of the observed reaction. It should be noted that the attack is not a property of the C40 phase, but of the secondary phases lining the grain boundaries.

Alloying studies were employed to validate the mechanisms suspected in the environmental sensitivity. Additions of titanium to form $(Mo,Ti)(Si, Al)_2$ have been shown to eliminate the grain boundary degradation observed in ternary $Mo(Si,Al)_2$. It has been shown through thermodynamic data that titanium has a much stronger affinity for carbon than either aluminum or silicon. The formation of titanium carbides in these alloys is the mechanism by which the formation of the SiC and, subsequently, environmentally susceptible Al_4C_3 is suppressed. Production of $W(Si,Al)_2$ by the same process has shown that powder processing of these alumino-silicide materials in graphite dies will invariably lead to carbon contamination. This contamination will likely take the form of coupled Al/SiC particles in the absence any strong carbide forming elements.

The conclusions made from this investigation are as follows:

1) Powder processing can be employed to successfully produce dense, nearly-single-phase $Mo(Si,Al)_2$.

2) Carbon contamination from pressing in graphite dies is responsible for the formation of coupled SiC/Al particles observed in the grain boundaries of powder processed $Mo(Si,Al)_2$

3) The grain boundary attack observed in the C40 compacts is a result of the coupled SiC/Al particles reacting with each other and the environment, and is not an intrinsic property of C40 $Mo(Si,Al)_2$.

4) $X(Si,Al)_2$ materials processed in this fashion will exhibit identical grain boundary behavior if the element X does not have a stronger affinity for carbon than silicon and aluminum,.

5) Alloying to form $(Mo,X)(Si,Al)_2$ (where X represents elements that form carbides more stable than SiC and Al_4C_3) will prevent the environmental susceptibility of the grain boundaries by suppressing the formation of SiC and the subsequent formation of Al_4C_3.

Future studies of the processing of $Mo(Si,Al)_2$ should focus on the relationship between composition and its effect on the disposition of carbide phases in the grain boundaries. Minimization of carbon contamination could be achieved through different consolidation methods (i.e. HIPing) and complete solid state processing through the elimination of liquid aluminum that forms upon heating of the powders. Once the environmental susceptibility is compensated for, the study of polycrystalline $Mo(Si,Al)_2$ on the basis of mechanical behavior could continue.

APPENDIX

FREE ENERGY DIAGRAMS

Figure A-1 Free energy diagram showing the relative free energies of the C, Al_4C_4, SiC, and Cr_2C_3 phases.

Figure A-2 Free energy diagram showing the relative free energies of the C, Al$_4$C$_4$, SiC, and HfC phases.

Figure A-3 Free energy diagram showing the relative free energies of the C, Al$_4$C$_4$, SiC, and NbC phases.

Figure A-4 Free energy diagram showing the relative free energies of the C, Al_4C_4, SiC, and TaC phases.

Figure A-5 Free energy diagram showing the relative free energies of the C, Al_4C_4, SiC, and TiC phases.

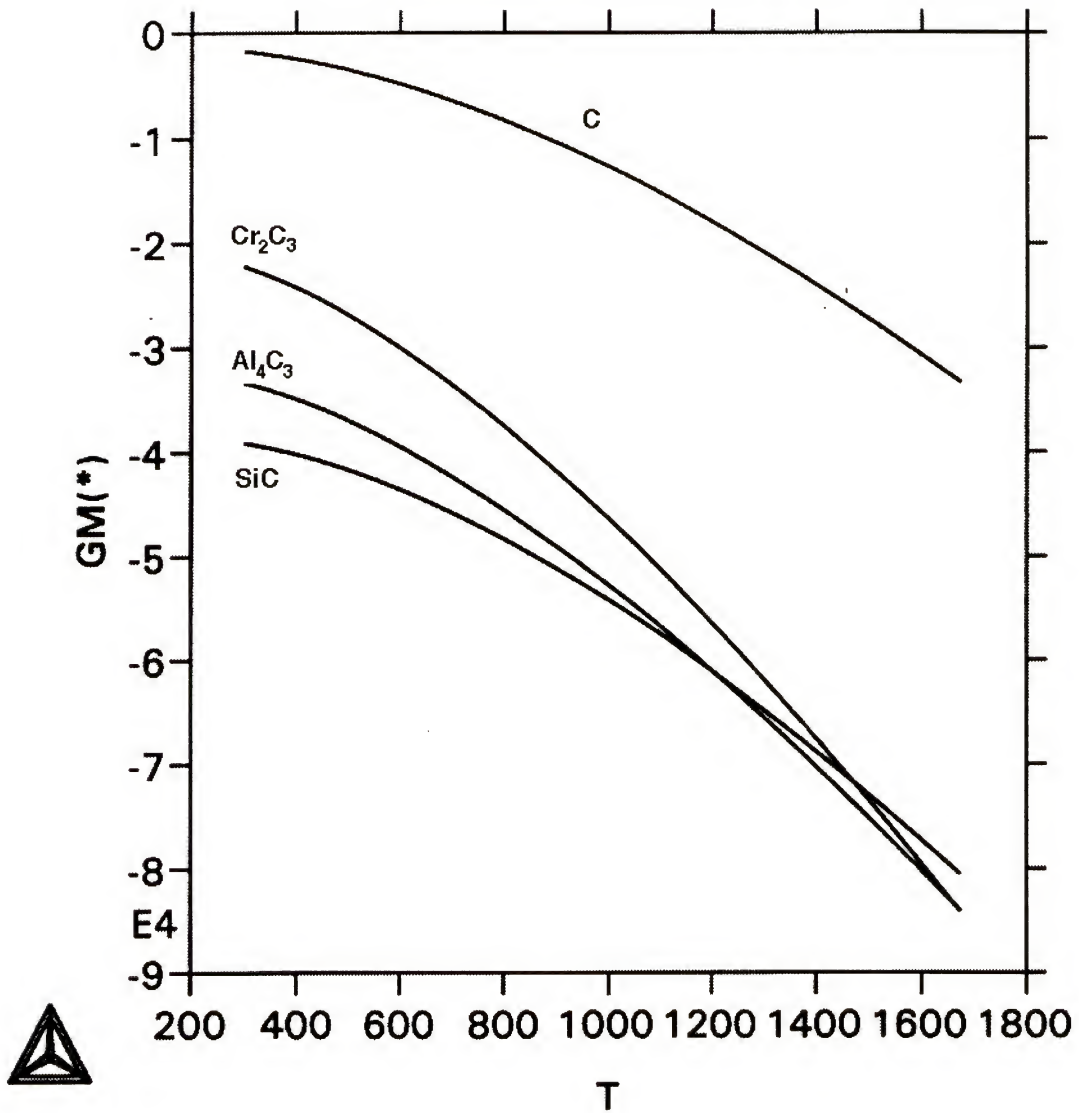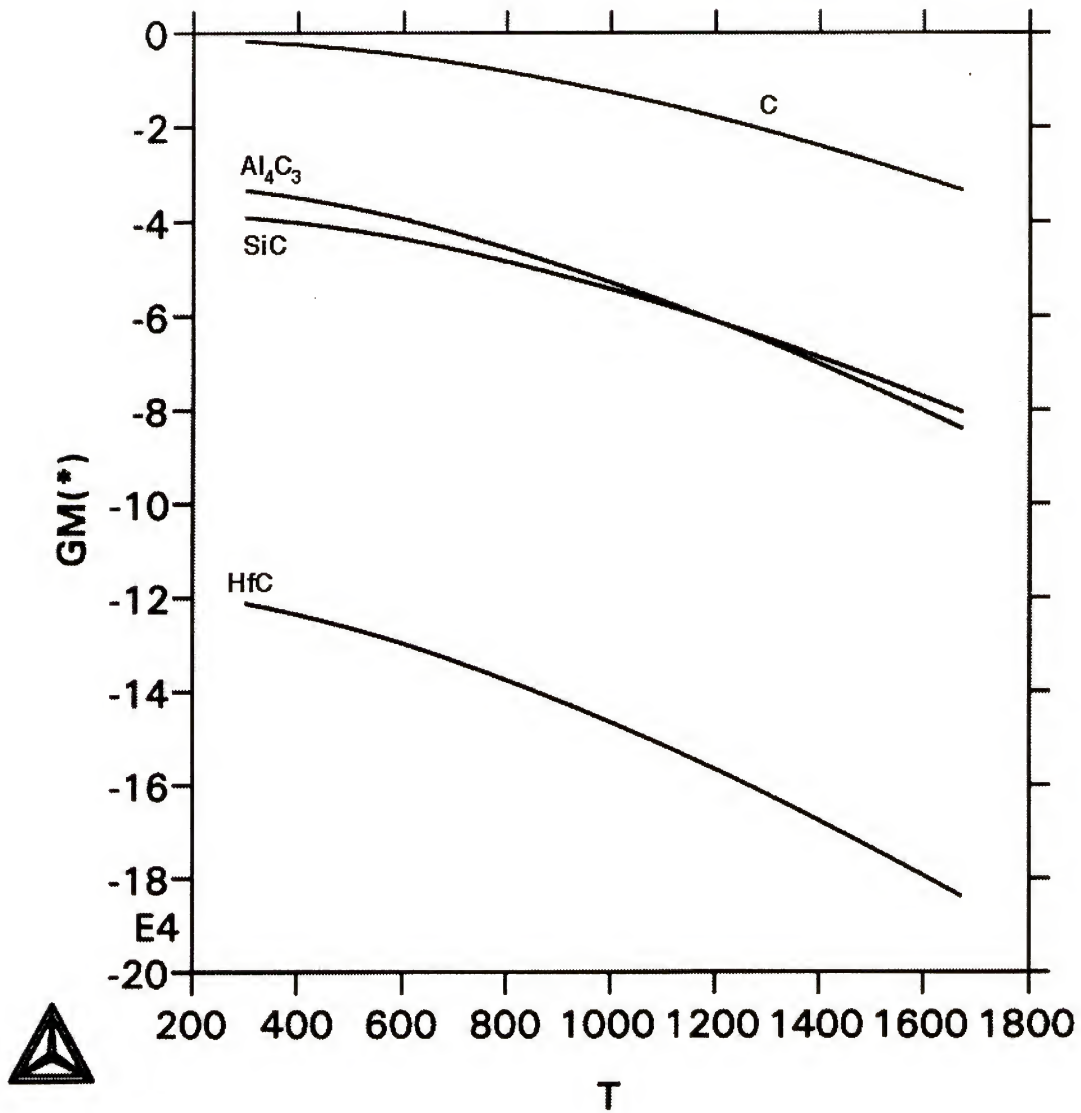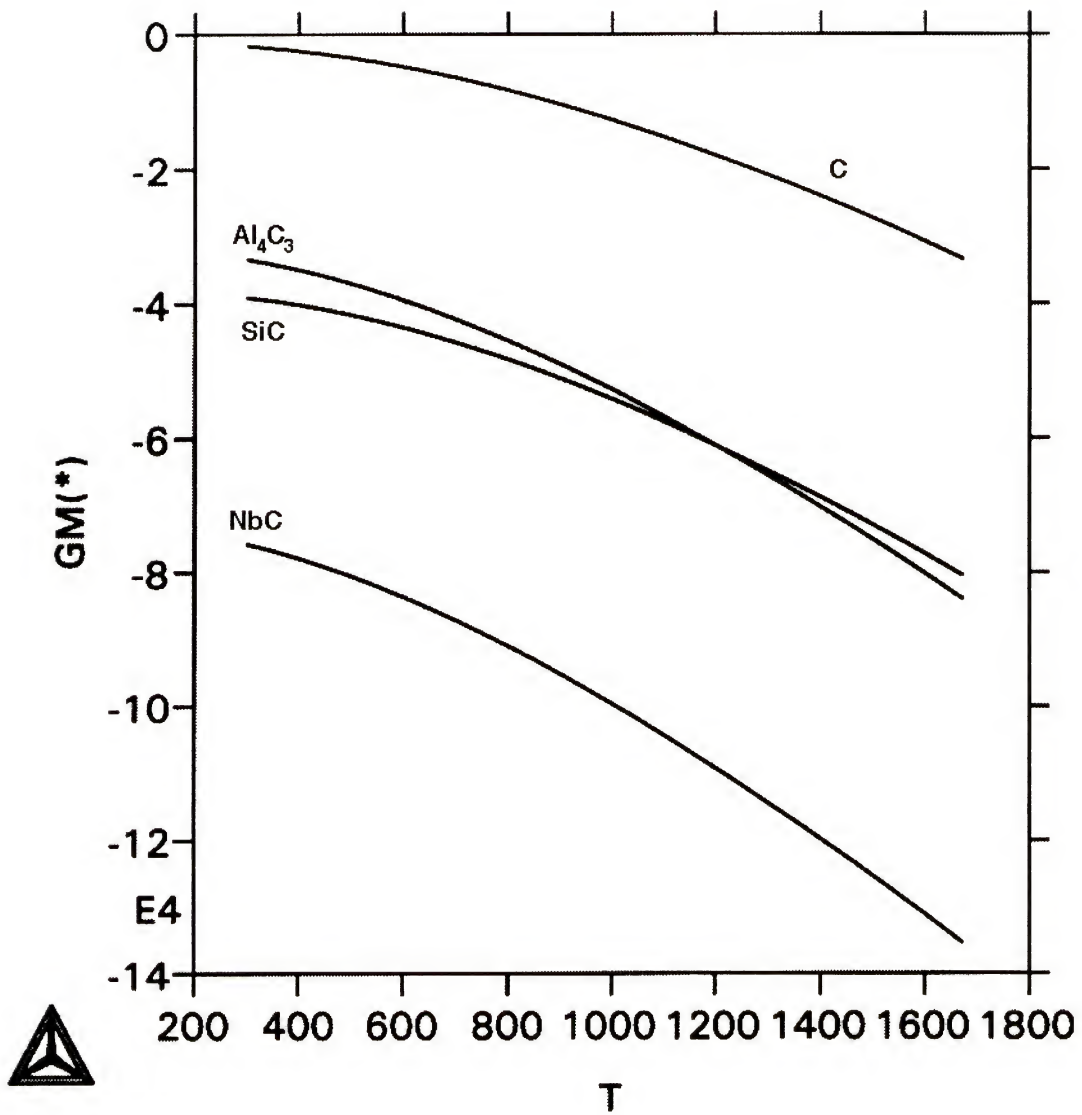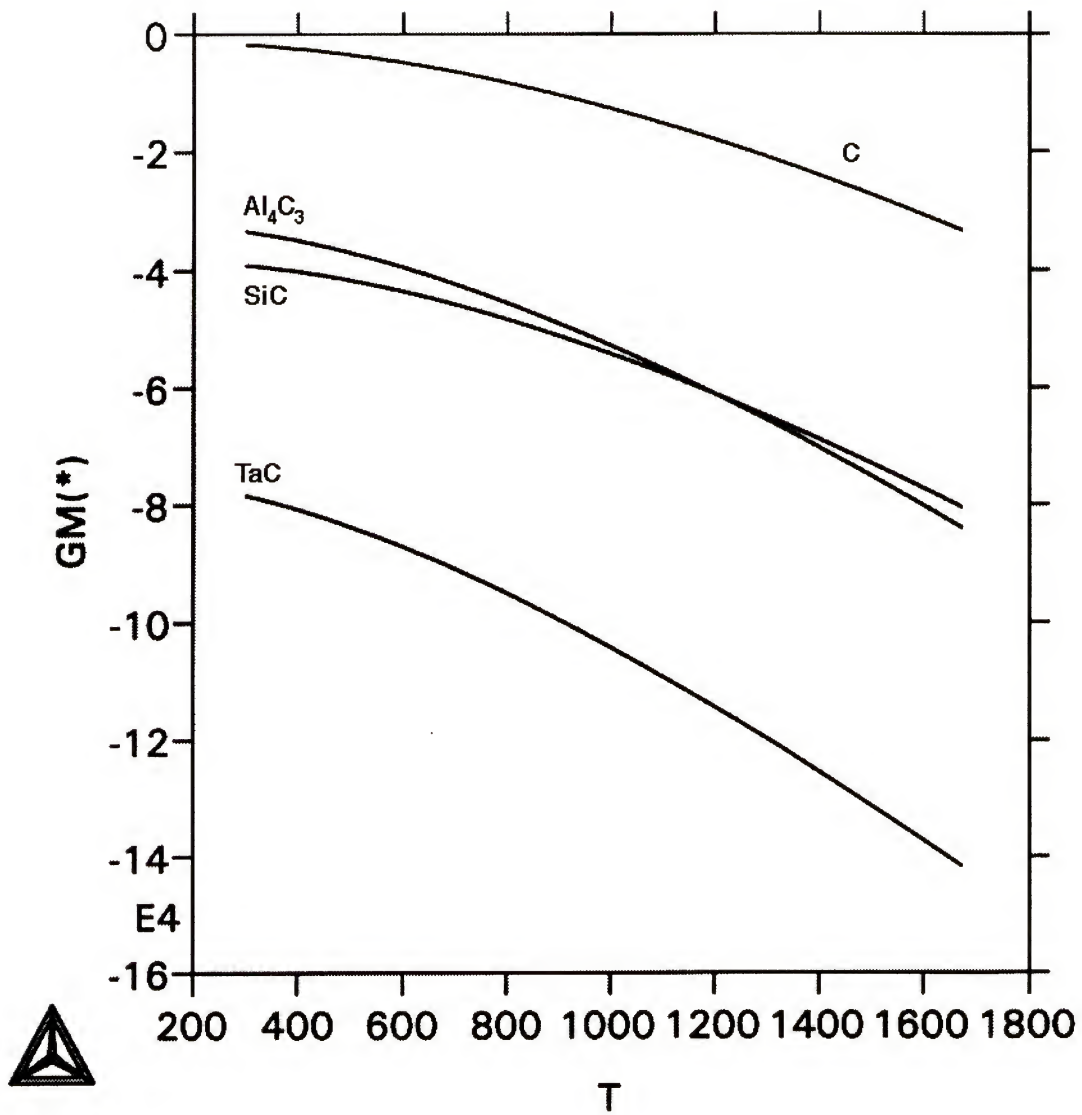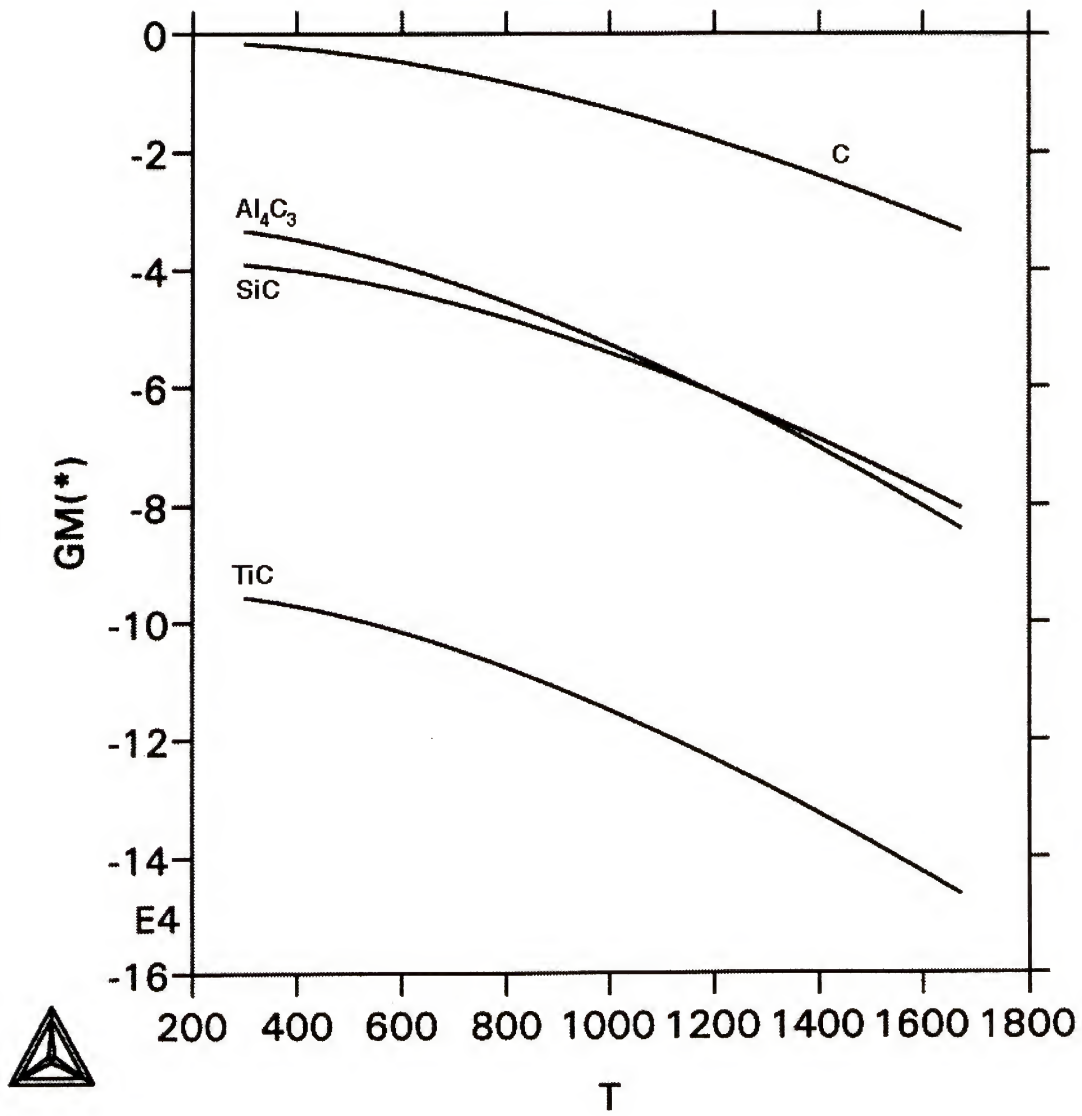Figure A-6 Free energy diagram showing the relative free energies of the C, Al_4C_4, SiC, and VC phases.
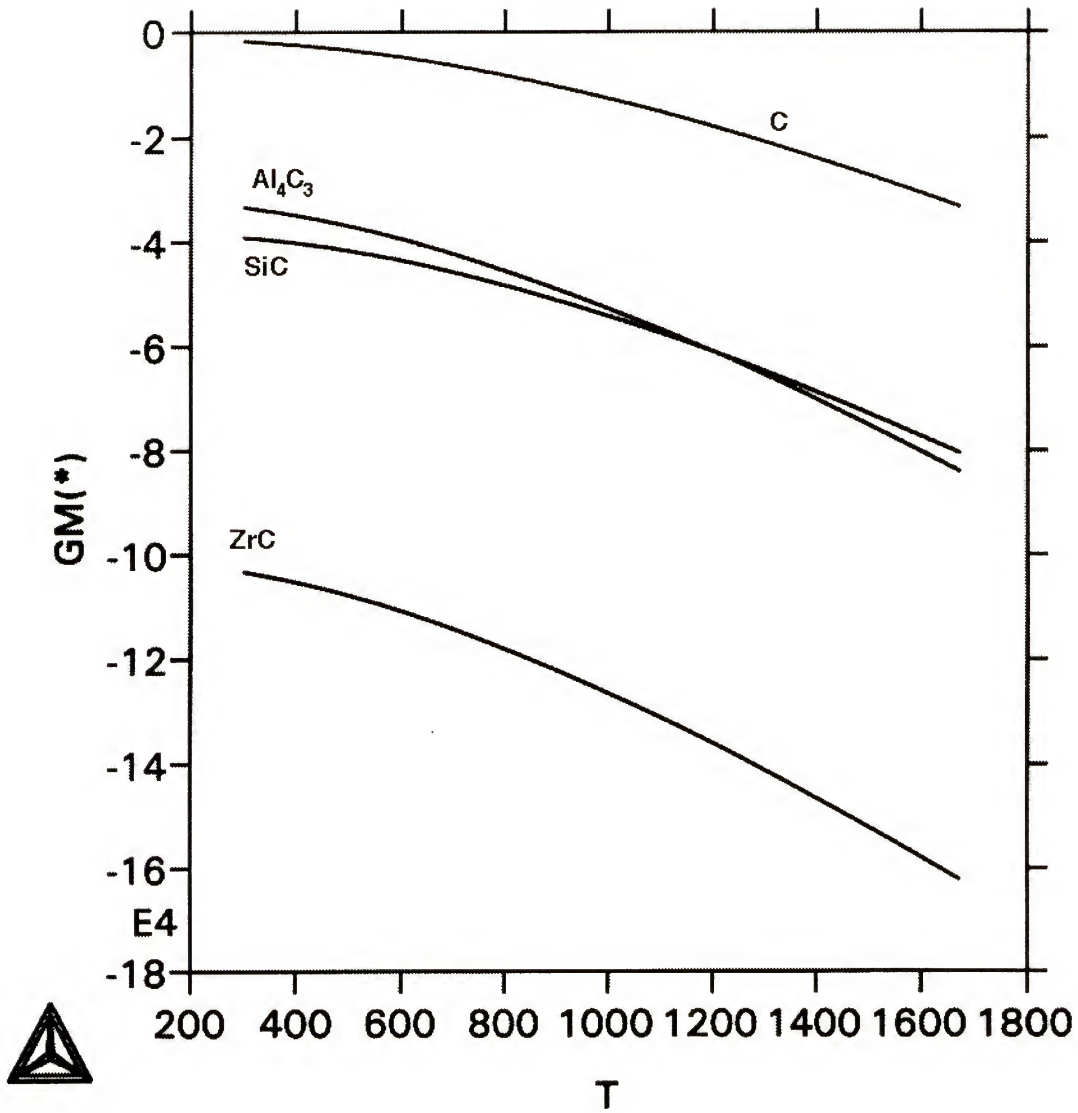
Figure A-7 Free energy diagram showing the relative free energies of the C, Al_4C_4, SiC, and ZrC phases.

REFERENCES

1. A. Gokhale, and G.J. Abbaschian, *The Mo-Si (Molybdenum Silicon) System.* Journal of Phase Equilibria, 1991. **12**: p. 493-498.

2. G.V. Samsonov, I.M. Vinitskii, Handbook of Refractory Materials, 1980. (**New York : IFI Plenum**).

3. W.J. Boettinger, J.H. Perepezko, P.S. Frankwicz, *Application of Ternary Phase Diagrams to the Development of $MoSi_2$-Based Materials.* Materials Science and Engineering, 1992. **A155**: p. 33-44.

4. W.A. Maxwell, *Study of molybdenum disilicide for elevated temperature applications.* Proc. Metallurgy and Materials Information Meet., 1951. **NSA-12**.

5. Kanthal, *Swedish Patent Number 155,836,* . 1953.

6. K.J. Bowman, *Refractory Metal Disilicides Research.* Report From MIAC Department of Defense, 1992. **2**.

7. A.K. Vasudevan, J.J. Petrovic, *A Comparative Overview of Molybdenum Disilicide Composites.* Materials Science and Engineering, 1992. **A155**: p. 1-17.

8. H. Nowotny, C.H. Brukl, *Ein Beitrag Zum Dreistoff: Molybdaen-Aluminum-Silicium.* Monatshefte fuer Chemie, 1960. **91**: p. 310-315.

9. H. Nowotny, E. Dimakodoulou, H. Kudielka, *Ein Beitrag Zum Dreistoff : Mo-Si-B.* Monatshefte fuer Chemie, 1957. **88**: p. 180.

10. H. Nowotny, E. Parthe, R. Kieffer, F. Benesovsky, *Das Driestoffsystem: Molybdaen-Silizium-Kohlenstoff.* Monatshefte fuer Chemie, 1954. **85**: p. 255-272.

11. C.H. Brukl, H. Nowotny, F. Benesovsky, *Untersuchugen in Den Dreistoffsystemen: V-Al-Si, Nb-Al-Si, Cr-Al-Si, Mo-Si-Al BZW. Cr(Mo)-Al-Si.* Moantshefte fuer Chemie, 1961. **92**: p. 965-967.

12. C.H. Brukl, H. Nowotny, O. Schob, F. Benesovsky, *Die Kristallstrukturen von TiSi, Ti(Al,Si)$_2$, und Mo(Si,Al)$_2$.* Monatshefte fuer Chemie, 1961. **92**: p. 779-785.

13. E. Fitzer, *Warmfeste und Korrosionsbestandige Sinterwerkstoffe.* 2nd Plansee Seminar, Ruette/Tirol June 19-23, 1955.

14. S.C. Deevi, *Diffusional Recations in the Combustion Synthesis of $MoSi_2$.* Materials Science and Engineering, 1992. **A149**: p. 241-251.

15. S.C. Deevi, and S. Deevi, *In-Situ Synthesis of MoSi$_2$-Al$_2$O$_3$ Composite by a Thermite Reaction.* Scripta Metallurigica et Materialia, 1995. **33**(3): p. 415-420.

16. S. Jayashankar, M.J. Kaufman, *Effect of Oxygen Content on the Superplastic Behavior of MoSi$_2$/SiC Composites.* Ceramic Engineering & Science Proceedings, Cocoa Beach, FL, 1996. **17**(4,5).

17. R.M.J. Aiken, *Structure and Properties of In-Situ Reinforced MoSi$_2$.* Ceramic Engineering & Science Proceedings, Cocoa Beach, FL, 1991. **12**(9,10): p. 1643-1655.

18. R.M. Aiken, Jr., *Strengthening of Discontinuously Reinforced MoSi$_2$ Composites at High Temperatures.* Materials Science and Engineering, 1992. **A155**: p. 121-133.

19. C.H. Henager, J.L. Brimhall, J.P. Hirth, *Synthesis of a MoSi$_2$-SiC Composite in-situ Using a Solid State Displacement Reaction.* Materials Science and Engineering, 1992. **A155**: p. 109-114.

20. A. Costa e Silva, M.J. Kaufman, *Microstructural Modifications of MoSi$_2$ Through Aluminum Additions.* Scripta Metallurgica et Materialia, 1993. **29**: p. 1141-1145.

21. A. Costa e Silva, *Synthesis of Molybdenum Disilicide Composites Using In-Situ Reactions*, . 1994, University of Florida.

22. Kanthal, *Kanthal Super Handbook.* 2 ed. 1984, Hallstahammar, Sweden: Kanthal Furnace products.

23. D. Leiser, *U.S. Patent Number 5,079,082*, 1997.

24. Y.L. Jeng, E.J. Lavernia, *Review: Processing of Molybdenum Disilicide.* Journal of Materials Science, 1994. **29**: p. 2557-2571.

25. D.A. Hardwick, P.L. Martin, S.N. Patankar, J.J. Lewandowski, *Processing-Microstructure-Property Relationships in Polycrystalline MoSi$_2$.* Structural Intermetallics. 1993, Warrendale, PA: TMS. 665-673.

26. F.S. Pettit and G.H. Meier , *Oxidation of Intermetallics and Sulfur Effects on Alumina Scale*, . 1995, University of Pittsburgh.

27. P.J. Meschter, *Oxidation of MoSi$_2$/Tib$_2$ and MoSi$_2$/Al$_2$O$_3$ Mixtures.* Scripta METALLURGICA et MATERIALIA, 1991. **25**(5): p. 1065-1069.

28. C.G. McKamey, P.F. Tortelli, J.H. De Van, and C.A. Carmichael, *A Study of Pest Oxidation in Polycrystalline MoSi$_2$* Journal of Materials Research, 1992. **7**(10): p. 2747-2755.

29. J.B. Berkowitz-Mattuck, P.E. Blackburn, and E.J. Felton, *The Intermediate-Temperature Oxidation Behavior of Molybdenum Dislicide.* Transactions of the Metallurgical Society of AIME, 1965. **233**(June): p. 1093-1099.

30. J.B. Berkowitz-Mattuck, M. Rosetti and D.W. Lee, *Enhanced Oxidation of Molybdenum Disilicide Under Tensile Stress: Relation to Pest Mechanisms.* Metallurgical Transactions, 1970. **1**(February): p. 479-483.

31. O. Kubaschewski, and B.E. Hopkins, *Oxidation of Metals and Alloys.* 2nd ed. 1962, London: Butterworths.

32. T.C. Chou, T.G. Nieh, *Pest Disintegration of Thin MoSi₂ Films by Oxidation at 500°C.* Journal of Materials Science, 1994. **29**: p. 2963-2967.

33. D.A. Berztiss, F.S. Pettit, G.H. Meier. *Anamolous Oxidation of Intermetallics.* in *Materials Research Society Symposium.* 1995: Materials Research Society.

34. J.L. Smialek, J.A. Nesbitt, W.J. Brindley, M.P. Brady, J. Doychak, R.M. Richardson and D.R. Hull. *Service Limitations for Oxidation Resistant Intermetallic Compounds.* in *Materials Research Society Symposium.* 1995: Materials Research Society.

35. A. Stergiou, P. Tsakiropolous, *Study of the Effects of Al, Ta, W additions on the Microstructure and Properties of MoSi₂ Based Alloys.* Materials Research Society Symposium Proceedings, 1995. **364**: p. 911-916.

36. A. Stergiou, P. Tsakiropoulos, *Oxiaditon studies on MoSi₂₋ₓ (X=Al,Ta,W) alloys.* Structural Intermetallics, 1997. **5**(2): p. 869-875.

37. K. Kurokawa, H. Matsuoka, H. Takahashi, and W.L. Worrell. *High Temperature Oxidation of MoSi₂-WSi₂ Solid Solutions.* in *Fourth International Symposium on High Temperature Corrosion and Protection of Materials.* 1996. France.

38. J. Schlichting, *Oxidation Kinetic of Silicon Ceramic from the Point of Refractory Materials Resistant Against Hot Corrosion.* Rev. Int. hautes Temper. Refract., 1979. **16**: p. 67-72.

39. V.U. Kodash, P.S. Kisly and V.J. Shemet, *High Temperature Oxidation of Molybdenum Aluminosilicides.* Hight Temperature Science, 1990. **29**: p. 143-152.

40. K. Yanigahara, T. Maruyama, and K. Nagata, *Isothermal and Cyclic Oxidation of Mo(Si₁₋ₓ,Alₓ) up to 2048 K.* Materials Transactions, JIM, 1993. **34**(12): p. 1200-1206.

41. K. Yanigahara, T. Maruyama, K. Nagata, *High Temperature Oxidation of Mo-Si-X Intermetallics (X=Al, Ti, Ta, Zr, Y).* Intermetallics, 1994. **3**: p. 243-251.

42. D.M. Shah, D. Berczick, D.L. Anton, and R. Hecht, *Appraisal of other silicides as structural Materials.* Materials Science and Engineering A, 1992. **A155**: p. 45-57.

43. A.J. Thom, M.K. Meyer, J.J. Williams, M. Akinc, *Improved Oxidation Resistance of A₅Si₃ (A=Transition Metal) Silicides by Small Atom Doping.* Processing and Fabricatrion of Advanced Materials IV, Proceedings of TMS 1996, 1996: p. 139-149.

44. B.V. Cockeram, Robert A. Rapp, *Oxidation-resistant boron- and germanium-doped silicde coatings for refractory metals at high temperature.* Materials Science and Enginieering A, 1995. **192**: p. 980-986.

45. J.H. Perepezko, C. Nunes, *Phase stability and microstructural design in high temperature (Mo,Nb)-Si-B alloys*, 1996, AFOSR Structural Metals Workshop: Bar Harbor, ME.

46. C.A. Nunes, R. Sakidja, J.H. Perepezko, *Phase stability in high temperature Mo-Rich Mo-B-Si alloys.* Structural Intermetallics, 1997. **5**(4): p. 831-839.

47. R. Sakidja, H. Sieber, J.H. Perepezko. *Microstructural development of Mo rich Mo-B-Si alloys.* in *TMS Annual Meeting.* 1998. San Antonio, TX: TMS, Warrendale PA.

48. J.H. Schneibel, C.T. Liu, L. Heatherly, M. Kramer, *Assessment of processing routes and strength of a 3-phase molybdenum boron silicide (Mo_5Si_3-Mo_5SiB_2-Mo_3Si).* To Appear in Scripta Metallurgica et Materialia, 1998.

49. K. Ishizaki, *Phase diagrams under high total gas pressures - Ellingham diagrams for hot isostatic press processes.* Acta Metallurgica et Materialia, 1990. **38**(11): p. 2059-2066.

50. G.C. Wei, *Beta SiC powders produced by carbothermic reduction of silica in a high temperature rotary furnace.* Journal of the American Ceramic Society, 1983. **66**(7): p. c111-c113.

51. E.N. Ross, P.D. Eason, M.J. Kaufman, *Processing of Low Silica $MoSi_2$-Based Compounds Using Carbon and Aluminum Additions.* Processing and Fabrication of Advanced Materials V, Proceedings of TMS Annual Meeting, 1996: p. 347-360.

52. A. Costa e Silva, *Applications of in situ reactions to $MoSi_2$ based materials.* Materials Science and Engineering A, 1994. **A195**: p. 75-88.

53. K. Matsura, T. Ohmi, M. Kudoh, T. Kakuhashi, T. Hasegawa, *Raective sintering of molybdenum alumino-silicide and its oxidation resistance.* Journal of Japan Institue of Light Metals, 1997. **47**(8): p. 446-451.

54. N. Saunders, *Al-Mo (Aluminum - Molybdenum)*, in *Binary Alloy Phase Diagrams*, T.B. Massalski, Editor. 1990, ASM International: Materials Park, OH. p. 174-176.

55. M. Fu, *A Study of Micropyretic Reactions in the Mo-Si-Al Ternary System.* Journal of Materials Research, 1997. **12**(6): p. 1481-1491.

56. D. Yi, Z. Lai, O.M. Akselsen, J.H. Ulvensoen, *Ternary alloying study of $MoSi_2$.* Metallurgical and Materials Transactions A, 1998. **29A**: p. 119-129.

57. A. Stergiou, and P. Tsakiropolous, *The Intermediate and High Temperature Oxidation Behaviour of $(Mo,X)Si_2$ (X=W,Ta) Intermetallic Alloys.* Intermetallics, 1997. **5**: p. 117-126.

58. M. Moriwaki, K. Ito, H. Inui, and M. Yamaguchi, *Plastic Deformation of $Mo(Si,Al)_2$ Single Crystals With the C40 Structure.* Mat. Res. Soc. Proc., 1997. **460**: p. 605-610.

59. P.D. Eason, M.J. Kaufman, Unpublished research, 1997.

60. J.H. Westbrook, D.L. Wood, *"Pest" Degradation in Beryllides, Silicides, Aluminides, and Related Compounds.* Journal of Nuclear Materials, 1964. **12**(2): p. 208-215.

61. G.H. Meier, *High temperature oxidaiton and corrosion of metal-silicides.* Materials Research Society Symposioum Proceedings, 1987. **81**: p. 443-458.

62. G.H. Meier and F.S.Pettit , *High Temperature Oxidation and Corrosion of Intermetallic Compunds.* Materials Science and Technology, 1992. **8**(4): p. 331-338.

63. Meschter, *Low-Temperature Oxidation of Molybdenum Disilicide.* Metallurgical Transactions A, 1992. **23A**(June): p. 1763-1772.

64. E.P. George, C.T. Liu, D.P. Pope, *Environmental Embrittlement: The Major Cause of Room Temperature Brittleness in Polycrystalline Ni₃Al.* Scripta Metallurgica et Materialia, 1992. **27**: p. 365-370.

65. H.J. Grabke, M. Steinhorst, M.W. Brumm, B. Wagemann, V.K. Tolpygo, I. Rommerskirchen, A.V. Katsman, *Intergranular oxidation and pesting of intermetallic compounds.* Materials Science Forum, 1996. **207-209**: p. 725-728.

66. D.J. Duquette, *Envrionmental resistance of intermetallic compounds and composite materials.* Materials Science and Engineering A, 1995. **A198**: p. 205-211.

67. D. Duquette, *Corrosion of Intermetallic Compounds*, in *Intermetallic Compounds : Vol 1, Principles*, J.H.W.a.R.L. Fleischer, Editor. 1994, John Wiley & Sons Ltd: New York. p. 965-975.

68. R.J. Hanrahan, M. Puga-Lambers. E. Lambers, S.P. Withrow. *A study of the mechanism of "pest" in niobium aluminde.* in *Elevated Temperature Coatings: Science and Technology II.* 1996. Anaheim, CA: TMS, Warrendale PA.

69. C.T. Liu, C.L. White, *Dynamic Embrittlement of Boron-Doped Ni₃Al Alloys at 600 C.* Acta Metallurigca, 1987. **35**(3): p. 643-649.

70. C.T. Liu, C.G. McKamey, E.H. Lee, *Environmental Effects on Room Temperature Ductility and Fracture in Fe₃Al.* Scripta Metallurgica et Materialia, 1990. **24**: p. 385-390.

71. C.T. Liu, E.P. George, *Environmental Embrittlement in Boron-Free and Boron-Doped FeAl (40 at. % Al) Alloys.* Scripta Metallurgica et Materialia, 1990. **24**: p.1285-1290.

72. C.T. Liu, M. Takeyama, *Environmental embrittlement in ordered Ni₃Fe.* Scripta Metallurgica et Materialia, 1990. **24**: p. 1583-1586.

73. C.T. Liu, Y-W. Kim, *Room Temperature Environmental Embrittlement in a TiAl Alloy.* Scripta Metallurgica et Materialia, 1992. **27**: p. 599-603.

74. T. Takasugi, C.L. Ma, S. Hanada, *Environmental embrittlement and grain boundary segregation of boron and carbon in Ni₃(Si,Ti) alloys.* Materials Science and Engineering A, 1995. **A192/193**: p. 407-412.

75.   R.W. Hertzberg, *Deformation and Fracture Mechanics of Engineering Materials.* 1989, New York: John Wiley & Sons.

76.   J. Stringer. *Environmental Interaction with Grain Boundaries.* in *4th Bolton Landing Conference.* 1975. Lake George, NY: Claitor's Publishing.

77.   D.A. Jones, *Principles and Prevention of Corrosion.* 1992, New York: Macmillan Publishing Co.

78.   R.E. Reed-Hill, R. Abbaschian, *Physical Metallurgy Priciples.* 3rd ed. 1992, Boston, MA: PWS-Kent Publishing. 926.

79.   D.A. Porter, and K.E. Easterling, *Phase Transformations in Metal Alloys.* 2 ed. 1992, London: Chapman and Hall.

80.   K.T. Aust, G. Palumbo, *Environmental Interactions at Grain Boundaries.* Transaction of the Japan Institute of Metals, 1986. **Supplement 27**: p. 995-1004.

81.   J.C. Viala, P. Fortier, J. Bouix, *Stable and metastable phase equilibria in the chemical interaction between aluminum and silicon carbide.* Journal of Materials Science, 1990. **25**(3): p. 1842-1856.

82.   J.K. Park, J.P. Lucas, *Moisture effect on SiCp/6061 Al MMC: dissolution of interfacial Al_4C_3.* Scripta Materialia, 1997. **37**(4): p. 511-516.

83.   T. Iseki, T Kameda, T. Maruyama, *Interfacial reactions between SiC and aluminum during joining.* Journal of Materials Science, 1984. **19**: p. 1692-1698.

84.   T. Iseki, T. Kameda, T. Maruyama, *Some properties of Al_4C_3.* Journal of Materials Science Letters, 1983. **2**: p. 675-676.

85.   K.L. Choy, *Effects of surface modifications on the interfacial chemical stability and strength of continuous SiC fibers aftre exposure to molten aluminum.* Scripta Metallurgica et Materialia, 1994. **32**(2): p. 219-224.

86.   B. Maruyama, L Rabenberg. *Oxidation model of interface reactions in aluminum/graphite composites.* in *Interfaces in metal matrix composites.* 1986: Metallurgical Society of AIME, Warrendale PA.

87.   B. Maruyama, F.S. Ohuchi, L. Rabenberg, *Catalytic carbide formation at aluminum carbon interfaces.* Journal of Materials Science Letters, 1990. **9**(7): p. 864-866.

88.   F.N. Rhines, *Phase Diagrams in Metallurgy: Their Development and Application.* 1956, New York: McGraw Hill Book Co. Inc.

89.   R.T. DeHoff, *Thermodynamics in Materials Science.* 1993, New York: McGraw Hill, Inc.

90.   D.R. Gaskell, *Introduction to Metallurgical Thermodynamics.* 2 ed. 1981, Washington DC: Hemisphere Publishing Corp. 611.

91.   P. Sahoo, M.J. Koczak, *Analysis of in-situ formation of titanium carbide in aluminum alloys.* Materials Science and Engineering, 1991. **A144**: p. 37-44.

BIOGRAPHICAL SKETCH

Paul D. Eason was born on August 4, 1971, in Jacksonville, Florida. He began attendance at the University of Florida in Fall of 1989. During summers and school breaks Paul held a position as an Engineering Assistant at the Jacksonville Electric Authority. He completed his undergraduate degree at the University of Florida in 1995 with a major in materials science and engineering, specializing in both metallurgy and ceramic engineering with a minor in business administration.

While attending the University of Florida, Paul was active in several professional and honorary organizations. He was the President of the Florida Student TMS/ASM Chapter and Keramos Honor Society, and was inducted into EΛX Engineering Leadership Fraternity. He also served on the advisory board for the Board of Regents Curriculum Review Committee. His involvement in professional societies extended into graduate school when he held the office of Vice President of the Florida Student TMS/ASM Chapter.

During the course of his time in graduate school Paul coauthored four papers with his advisor, Prof. Michael Kaufman. He received his doctorate in materials science and engineering from the University of Florida in 1998.

Paul's strong interest in travel has taken him across North America, as well as to countries such as Turkey, Iceland, Sweden, Denmark and Greece. His other interests include playing and listening to music, collecting wine, cooking, and architecture.

I certify that I have read this study and that in my opinion it conforms to acceptable standards of scholarly presentation and is fully adequate in scope and quality, as a dissertation for the degree of Doctor of Philosophy.
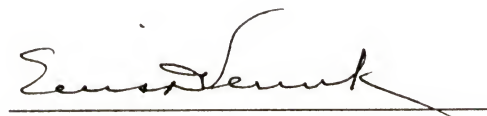
Michael J. Kaufman, Chairman
Professor of Materials Science and
Engineering

I certify that I have read this study and that in my opinion it conforms to acceptable standards of scholarly presentation and is fully adequate in scope and quality, as a dissertation for the degree of Doctor of Philosophy.
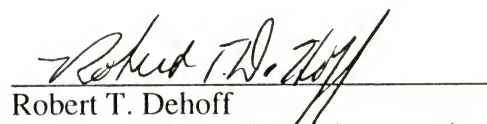
Reza Abbaschian
Professor of Materials Science
and Engineering

I certify that I have read this study and that in my opinion it conforms to acceptable standards of scholarly presentation and is fully adequate in scope and quality, as a dissertation for the degree of Doctor of Philosophy.

Ellis D. Verink
Distinguished Service Professor
Emeritus of Materials Science
and Engineering

I certify that I have read this study and that in my opinion it conforms to acceptable standards of scholarly presentation and is fully adequate in scope and quality, as a dissertation for the degree of Doctor of Philosophy.

Robert T. Dehoff
Professor of Materials Science and
Engineering

I certify that I have read this study and that in my opinion it conforms to acceptable standards of scholarly presentation and is fully adequate in scope and quality, as a dissertation for the degree of Doctor of Philosophy.

Timothy J. Anderson
Professor of Chemical Engineering

This Dissertation was submitted to the Graduate Faculty of the College of Engineering and to the Graduate School and was accepted as partial fulfillment of the requirements for the degree of Doctor of Philosophy.

December, 1998

Winfred M. Phillips
Dean, College of Engineering

M.J. Ohanian
Dean, Graduate School